Real-Time Simulation of Full-Field Atmospheric Turbulence for a Piloted Rotorcraft Simulator

by

John Edward Robinson III

S.B., Aeronautics and Astronautics
Massachusetts Institute of Technology, 1993

Submitted to the Department of Aeronautics and Astronautics
in Partial Fulfillment of the Requirements of the Degree of

Master of Science in Aeronautics and Astronautics

at the
Massachusetts Institute of Technology
May 1994

Signature of Author. .....
Department of Aeronautics and Astronautics
May 6, 1994

Certified by. .....
Steven R. Hall, Associate Professor
Department of Aeronautics and Astronautics
Thesis Supervisor

Certified by. .....
David G. Miller, Senior Technical Specialist
Boeing Defense and Space Group, Helicopters Division
Thesis Supervisor

Accepted by. .....
Professor Harold Y. Wachman, Chairman
Department Graduate Committee

Real-Time Simulation of Full-Field Atmospheric Turbulence for a Piloted Rotorcraft Simulator

by

John Edward Robinson III

Submitted to the Department of Aeronautics and Astronautics on May 6, 1994, in partial fulfillment of the requirements of the degree of Master of Science in Aeronautics and Astronautics

Abstract

A full-field atmospheric turbulence model has been developed for use with real-time, piloted rotorcraft simulators. The simulated atmospheric turbulence consists of longitudinal, lateral and vertical velocity components, based on the Von Kármán expressions for the second-order statistics of the turbulence field. Turbulence time samples are generated in real time using a summation of sinusoids together with a novel transformation of the von Kármán spectra from Cartesian to polar coordinates. This transformation allows the spectra to be integrated analytically, and reduces the number of harmonics required in the summation by more than a factor of 100. In addition, a non-Gaussian cumulative probability distribution of turbulence is used, and variations of scale length and turbulence intensity with altitude are included. Simulation requires parallel processing of the full-field atmospheric turbulence model in conjunction with a blade element rotor model.

Quantitative evaluation of the full-field turbulence model was done through comparison of statistical variations of a CH-47D's response to turbulence in level cruise. The full-field atmospheric turbulence model predicted less vertical acceleration and more pitch acceleration than the traditional turbulence model. Inspection of the accelerations along the other axes did not show significant differences between the turbulence models. Also, qualitative evaluation was done through pilot evaluation of a CH-47D's response to turbulence during a series of representative maneuvers. The pilots were unable to identify the full-field atmospheric turbulence model as more realistic.

Thesis Supervisor: Steven R. Hall, Sc.D.
Title: Associate Professor, Department of Aeronautics and Astronautics

Thesis Supervisor: David G. Miller
Title: Senior Technical Specialist, Boeing Defense and Space Group, Helicopters Division

Acknowledgements

I would like to acknowledge several people who helped me throughout this project. First, thanks go to Dr. Timothy Weber from Hewlett Packard (formerly from Boeing Helicopters) and Mr. David Miller from Boeing Helicopters for their invaluable technical support, guidance and expertise during this project. Next, thanks go to Mr. Marty Haglund from Boeing Helicopters for his countless answers to questions about C, FORTRAN, and the Boeing Helicopters computer network, in general. Thanks go to Mr. David MacArthur from Boeing Helicopters for his many answers to questions about the flight simulator's motion system. Thanks go to Mr. Jim Taylor from Boeing Computer Services for his patience during the many not-so-productive flight simulation sessions which were needed before this project could be completed. And, of course, thanks go to Dr. Steven Hall for his guidance, explanations, instruction and suggestions for this project and other aspects of aeronautics.

I would like to acknowledge Mr. Ray Dunn, Mr. Ron Mecklin, Mr. Reggie Murrel and Mr. John Tulloch from Boeing Helicopters for their participation in the pilot evaluation of the atmospheric turbulence models.

Finally, I gratefully acknowledge the financial support from Boeing Helicopters and the technical support from Boeing Helicopters' Flight Simulation Laboratory.

Contents

List of Figures

List of Tables

Chapter 1

Introduction

Today, the helicopter is no longer a vehicle used only for simple missions, where the ability to hover in calm atmospheric conditions is sufficient. Rotorcraft are routinely given complex missions which subject the aircraft to conditions and maneuvers at the edge of their flight envelopes. One requirement mandated by this expanded flight envelope is the ability to sustain stabilized flight through turbulence to accomplish high workload tasks.

Rotorcraft have shown greater reliability and productivity in mission performance for certain high workload tasks than other forms of transportation. As a result of this unique ability, helicopters regularly compete with traditional forms of transportation for many roles. For example, the British Coast Guard relieves lighthouses and lightships along its coastline by helicopter, because they have demonstrated a greater mission reliability than the alternative form of replenishment by relief boat [7]. Also, helicopters based on drilling platforms in the North Sea provide quick, reliable evacuation and rescue services for the oil rig personnel. These civilian helicopters must operate to and from landing pads, often in severe atmospheric turbulence, with gusts reaching 60 miles per hour. Reliable mission performance in harsh environments is repeated by the United States Army's rotorcraft requirement of *all-weather* operation. Also, the United States Navy and Marine Corps perform missions that routinely expose their helicopters to equally extreme atmospheric conditions. For example, "Naval and Marine rotorcraft are required to hover above and land on ships, in wind gusts in excess of 50 miles per hour, while stormy seas induce ship

deck oscillations in excess of 25 feet."[6] As future rotorcraft are more frequently involved in *all-weather* and *nap-of-the-earth* (NOE) operations, a substantial portion of their service lifetime will be spent exposed to moderate and severe atmospheric turbulence. Therefore, it is imperative to have the capability to accurately simulate during the engineering process the various atmospheric conditions the rotorcraft may encounter.

The need for improved rotorcraft atmospheric turbulence modeling is unanimously echoed by the pilots who fly helicopter simulators. Most of these pilots agree that while they do feel some "atmospheric turbulence" acting on the flight simulator, the motions are not equivalent to those induced in the actual helicopter by real atmospheric turbulence. Many complain that compared to real atmospheric turbulence, the simulated version is too repetitious and does not contain "patches" of turbulent air interrupted by periods of calm air as the real atmosphere does. As a result of this regularity, pilots and automatic control systems may implement lead compensation to effectively cancel the effects of the simulated atmospheric turbulence. Such simple control system compensation does not effectively neutralize the aircraft motions caused by real atmospheric turbulence, since realistically there is no repetitive element in the actual turbulence field. Results obtained using simplistic atmospheric turbulence models may be misleading, or even incorrect. Thus, improved atmospheric turbulence simulation is a benefit to the design process as well as to piloted simulation fidelity.

The effects of atmospheric turbulence have been a major concern to the fixed-wing aircraft designer since the early days of flight [9]. Atmospheric turbulence impacts both flight dynamics and structural dynamics problems under every flight and atmospheric conditions. Typical turbulence related problems which must be addressed during the design of *all* aircraft include (1) the ultimate structural strength required to sustain peak gust loads, (2) the effects of turbulence on the aircraft's fatigue life, (3) the control system's performance in turbulence, i.e., gust rejection characteristics, and (4) the aircraft's handling and ride quality in turbulence. Only recently has it been recognized that

improved design criteria considering the effects of atmospheric turbulence are specifically required for future rotorcraft. Earlier studies of the effects of atmospheric turbulence on rotorcraft neglected the rotational sampling of the atmosphere by the helicopter's rotor blades. Instead, rotorcraft designers simply adopted their atmospheric turbulence models from the fixed-wing community. These models generally used a point approximation of the aircraft and sampled the atmospheric turbulence field at the aircraft's center of gravity. Unfortunately, these models do not adequately address the complexities associated with rotational sampling of the atmospheric turbulence field by the helicopter's rotor blades.

Recently, the fundamental physics underlying rotorcraft atmospheric turbulence modeling have been investigated in detail, and newly developed advanced rotorcraft atmospheric turbulence models seem capable of correcting several deficiencies present in earlier models [6, 25]. The purpose of this research is to quantify the benefits to realistic real-time piloted simulation of new rotorcraft specific advancements in atmospheric turbulence modeling. This is achieved by evaluating, through real-time and non-real-time simulation, a stochastic full-field model describing the atmospheric turbulence field experienced by the main rotors of a tandem helicopter.

The problem of modeling atmospheric turbulence has been investigated in varying detail during the past 40 years. Chapter 2 provides a brief overview of traditional atmospheric turbulence modeling. This includes a description of the general techniques used to simulate atmospheric turbulence for flight simulation; a review of the principle works investigating atmospheric turbulence modeling, for rotary wing aircraft, as well as for wind turbines and fixed wing aircraft; and a description of the general rotorcraft geometry used throughout this research.

Although recent work has greatly improved the physical understanding of rotorcraft atmospheric turbulence modeling, there has been little effort or ability to validate these models through real-time flight simulation and subsequent pilot evaluation. Chapter 3 outlines the statistical description of the atmospheric turbulence field and develops a novel

computation scheme which allows real-time execution. Each turbulence field velocity component is described by a summation of two-dimensional sinusoidal functions with uniformly distributed random phases. In this respect, this computation algorithm is similar to the ocean wave simulation method proposed by Borgman [1]. It is worth noting that no previous full-field rotorcraft atmospheric turbulence model has achieved real-time execution.

The atmospheric turbulence model developed in Chapter 3 has been fully implemented into Boeing Helicopters' comprehensive tandem helicopter simulator[1] for real-time simulation and piloted evaluation. Full descriptions of the Boeing Helicopters' tandem helicopter simulator and the flight simulation experimental procedure are given in Chapter 4.

The full-field atmospheric turbulence model was evaluated non-real-time to determine the expected ability of pilots to perceive the possible changes in the flight simulation realism. These results are reported and analyzed in Chapter 5. The real-time results of the pilot evaluation consist of qualitative information from the pilot survey and quantitative information from the simulated flight data. These survey responses and flight data are also reported and analyzed in Chapter 5.

Conclusions which can be drawn from this research are discussed in Chapter 6. Also, possible reasons for uncertainty in some areas of the investigation and recommendations for future research in the area of atmospheric turbulence simulation are discussed.

[1] The acronym BHSIM is used to refer to Boeing Helicopters' Comprehensive Real-Time Rotorcraft Simulator.

Chapter 2

Atmospheric Turbulence Modeling

This chapter contains the necessary background information for understanding the modeling and implementation issues of atmospheric turbulence. First, several appropriate axis systems for tandem rotor helicopter flight simulation are introduced. Then, an overview of general atmospheric turbulence models and their simulation methods are discussed from a historical perspective. Finally, a brief summary of related works in the wind turbine, aircraft and rotorcraft communities is given.

2.1 Axis Systems

Before discussing atmospheric turbulence modeling, it is relevant to first specify the various axis systems which necessarily arise during the flight simulation calculations [12, 19]. There are five relevant coordinate frames. These are (1) the inertial frame, (2) the atmospheric frame, (3) the body frame, (4) the shaft-normal frame and (5) the blade element frame.

The inertial frame is fixed or in uniform rectilinear motion relative to the distant stars. (See F_I in Figure 2-1.) For most flight simulations, the Earth's rotation can be neglected, so the inertial frame also corresponds to an axis system which is fixed with respect to the Earth's surface. The inertial $\hat{x}$, $\hat{y}$ and $\hat{z}$-axes are traditionally oriented North, East and Down, respectively.

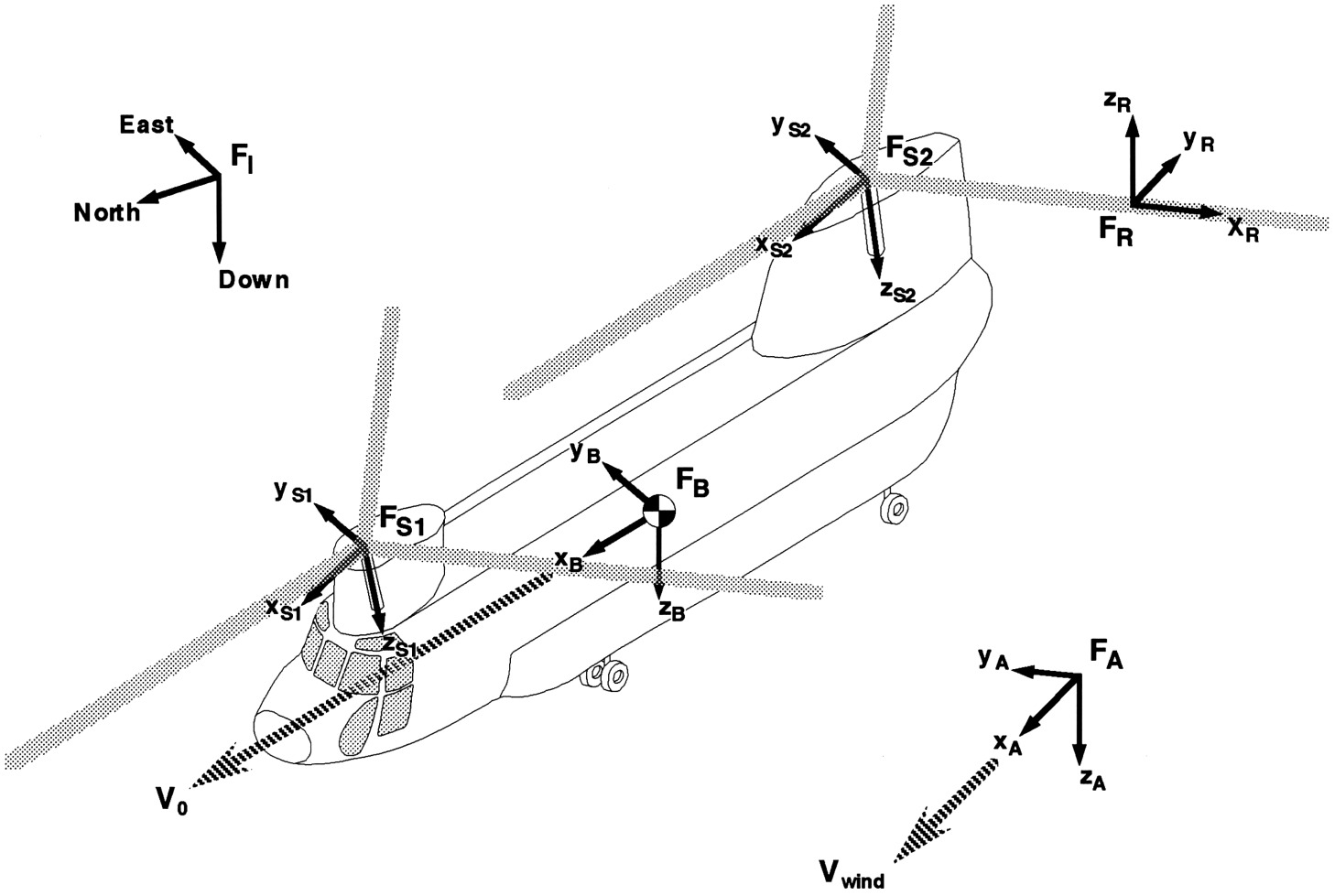

Figure 2-1: Axis Systems of Rotorcraft Flight Simulation

The atmospheric frame convects with the mean wind, and its $\hat{x}$-axis is oriented in the direction of the mean wind velocity vector. (See F_A in Figure 2-1.) This motion defines each individual patch of turbulence to be fixed with respect to the atmospheric frame. For this research, the mean wind was restricted to be parallel to the Earth's surface, i.e., no mean updrafts. Therefore, the atmospheric $\hat{z}$-axis is oriented Down, and the atmospheric $\hat{y}$-axis is chosen to complete the right-hand axis system.

The body frame is fixed with respect to the aircraft's center of gravity. (See F_B in Figure 2-1.) Most flight vehicles, the CH-47D included, display a plane of physical symmetry. This plane of symmetry is traditionally defined to be the $\hat{x}$-$\hat{z}$ plane. The body $\hat{x}$-axis is oriented through the nose of the aircraft, and the body $\hat{z}$-axis is oriented through the bottom of the aircraft. The body $\hat{y}$-axis is chosen to complete the right-hand axis system, and is therefore out the right side of the aircraft.

The shaft frame is fixed with respect to the main rotor hub, but does not rotate. (See F_{S1} and F_{S2} in Figure 2-1.) For the CH-47D, there are two shaft frames, one for each main rotor. The shaft $\hat{z}$-axis is oriented along the rotor shaft. Since the CH-47D's rotor shafts are tilted longitudinally[1], but not laterally, the shaft $\hat{y}$-axis is aligned parallel to the body $\hat{y}$-axis. The shaft $\hat{x}$-axis is chosen to complete the right-hand axis system.

The blade element frame is fixed with respect to an individual blade element, so it rotates at the rotational speed of the main rotor. (See F_R in Figure 2-1.) The blade element $\hat{x}$-axis is oriented in the spanwise direction of the blade element, and the blade element $\hat{y}$-axis is oriented in the chordwise direction of the blade element. The blade element $\hat{z}$-axis is chosen to complete the right-hand axis system. For this research, there were six blade element frames, each located at the $^3/_4$ radius of a different rotor blade.

Once defined, these axis systems allow the spatial location of any point in one frame to be mapped to the unique spatial location in any other frame. Similarly, the atmospheric turbulence velocity vector at any point fixed in the atmospheric frame (where it is assumed

[1] The forward rotor shaft is pitched forward 9° and the aft rotor shaft is pitched forward 4°.

to be temporally constant) may be related to the velocity vector at the respective point in the blade element frame.

2.2 General Atmospheric Turbulence Models

When modeling atmospheric turbulence for flight simulation, it is generally assumed that the atmospheric aerodynamics occur independent of the aircraft aerodynamics. Therefore, the aircraft does not affect the atmospheric turbulence field, while the atmospheric turbulence field does affect the aircraft. The aircraft simply samples the velocity field, and possible aerodynamic interactions are not modeled. The two general techniques of modeling atmospheric turbulence for flight simulation are the discrete gust model and the stochastic gust model [15].

2.2.1 Discrete Gust Model

The discrete gust model injects a deterministic time signal into the relative mean wind velocity vector of the aircraft. Several different discrete gust "shapes" are typically used to disturb the aircraft. Standard time signals include step functions, ramp functions, sine functions and one-minus-cosine functions. Examples are illustrated pictorially in Figure 2-2. Although the discrete gust model does not actually resemble atmospheric turbulence, it has been found to be quite useful during the preliminary design process for the prediction of ultimate aircraft loads and worst case scenarios. Also, sinusoidal discrete gusts have been used to investigate the extent of possible excitation of specific resonant modes of the aircraft by flight through atmospheric turbulence.

For discrete gust analyses, two methods are used to inject the time signal into the mean wind velocity vector of the aircraft. These are the instantly engulfing discrete gust and the gradually penetrating discrete gust. The instantly engulfing discrete gust abruptly changes the mean wind velocity vector of the entire aircraft. The gust velocity is spatially uniform along the entire aircraft, and it resembles a simple perturbation in the aircraft's

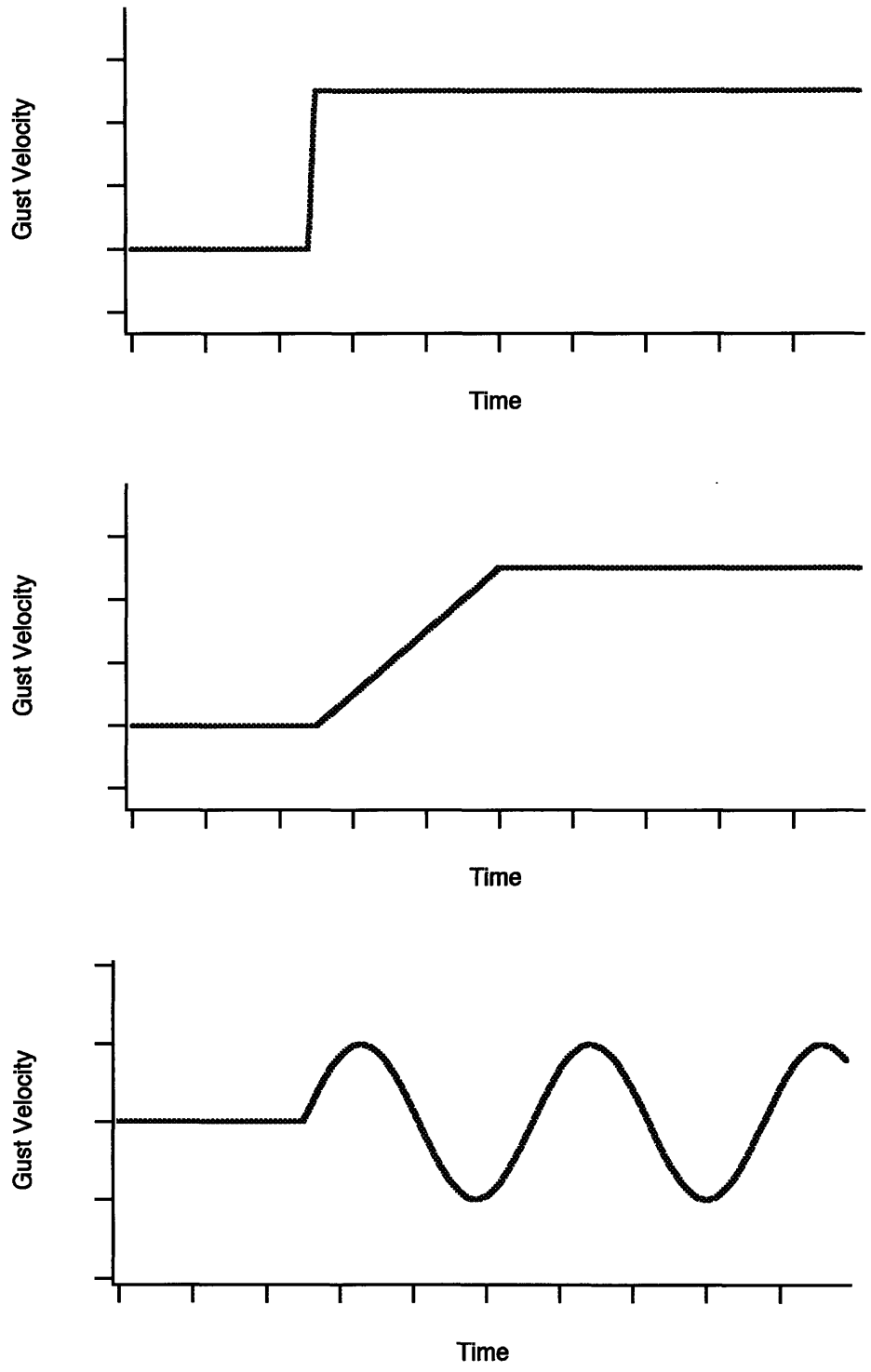

Figure 2-2: Typical Discrete Gust Time Samples

rigid body linear and rotational velocities. The gradually penetrating discrete gust varies spatially along the aircraft by considering the relative spatial position of the aircraft's aerodynamic components in the atmospheric turbulence field. The discrete gust convects past the aircraft at the true airspeed. Inclusion of this relative motion allows the different aerodynamic surfaces of the aircraft to experience the appropriate time lags associated with their sampling of the velocity field. Earlier research into helicopter response to gusts has shown that it is important to use gradually penetrating discrete gusts to obtain realistic rigid body responses and gust load factors [8].

2.2.2 Stochastic Gust Model

The stochastic gust model injects a continuous random time signal into the relative mean wind velocity vector of the aircraft. This random time signal has the amplitude and frequency content characteristic of a specific atmospheric condition. Figure 2-3 shows a typical time sample of atmospheric turbulence. Several standard stochastic models are used to represent the atmospheric turbulence field in terms of meteorological and geographical parameters. These statistical definitions of the atmosphere are discussed in Sections 3.1 and 3.3. Although this research used analytical models of the atmosphere, closed-form solutions, while convenient, are not sufficiently accurate for all atmospheric conditions. Wherever possible, empirical models, describing specific geographical locations and atmospheric conditions, should be used instead.

Like the deterministic time signal of the discrete gust model, two methods are used to inject the random time signal into the mean wind velocity vector of the aircraft. For rotorcraft analyses, these are commonly referred to as hub-fixed sampling and full-field sampling. Hub-fixed sampling models sample the atmospheric turbulence field at a single point fixed in the body frame, typically the aircraft center of gravity or the main rotor hub. The atmospheric turbulence velocity is thereby assumed to be spatially uniform along the entire aircraft with this sampled velocity. This point approximation is valid only when the

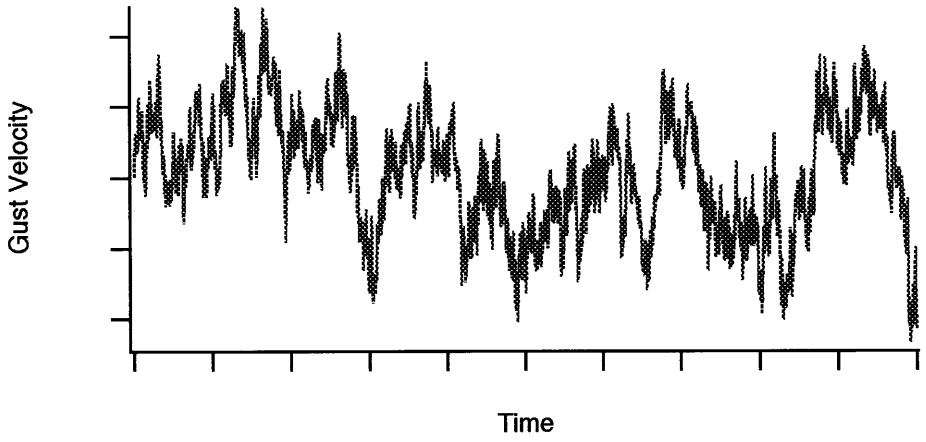

Figure 2-3: Typical Stochastic Gust Time Sample

physical dimensions of the aircraft are small with respect to the wavelengths of the significant spectral components of the velocity field [12]. However, rotorcraft often operate in atmospheric conditions where this criterion is not adequately satisfied. For example, at low altitude, the dominant wavelengths of the velocity field may be of an order equal to the physical dimensions of the aircraft. As a result, spatial variations of the velocity field across the rotor disks will be important. Under these circumstances, individual points on the aircraft must be considered separately. Full-field sampling models sample the atmospheric turbulence field at multiple points fixed on individual fuselage panels and blade elements. The sampled atmospheric turbulence velocities then include the correct spatial variations along the aircraft and the correct rotational sampling along the rotor.

2.3 Atmospheric Turbulence Simulation Techniques

In the previous section, general methods of modeling atmospheric turbulence for flight simulation were outlined. Little elaboration needs to be made about the implementation of a discrete gust model. Conversely, the stochastic gust model is considerably more complex, and several techniques can be used for its implementation into flight simulators. These techniques include measured turbulence, linearly filtered white noise and summation of sinusoids [18]. This section now discusses these techniques from the standpoint of their statistical fidelity to atmospheric turbulence and their suitability for real-time flight simulation.

2.3.1 Measured Turbulence

Flight recordings of atmospheric turbulence obviously produce statistically realistic time samples. Unfortunately, several problems make this method unsuitable for flight simulation. First, it is difficult, if not impossible, to adapt the measured time samples to atmospheric conditions other than those for which they were specifically recorded. Therefore, to accommodate changes of altitude or atmospheric conditions, a prohibitively

large database of recorded time samples must be available during flight simulation. Second, the measured time samples have fixed lengths. Extended time samples can only be produced by repetition of the measured time samples. This repetition is objectionable to pilots who are expecting random disturbances. Finally, even with a large database of recorded time samples, pilots may begin to recognize the prominent features of individual measured time samples after multiple exposures to them. Such recognition allows the pilots to better anticipate future aircraft disturbances. Subsequently, they are able to input more phase lead compensation into their response, effectively canceling the effects of these disturbances. Therefore, except in limited circumstances[2], recorded time samples of atmospheric turbulence are not suitable for flight simulation.

2.3.2 Linearly Filtered White Noise

Linearly filtering white noise is the classical method for generating atmospheric turbulence time samples for flight simulation. When white noise is passed through the appropriate shaping filter, the statistics of the output time sample match the statistics of the theoretically derived atmospheric turbulence model. For steady translation, the shaping filter representing the atmospheric turbulence velocities sampled at the aircraft center of gravity is remarkably easy to implement, since it is first-order and stationary. Spatial variations, e.g. the distribution along the wingspan or along the fuselage, may be included by correctly correlating multiple white noise sources. Conversely, for steady rotation, the shaping filter representing the atmospheric turbulence velocities sampled at the $^3/_4$ radius of a helicopter rotor blade is high order and cyclostationary with a period equal to the rotational velocity of the rotor. Such numerically complicated shaping filters may be designed, but they are difficult to adapt to atmospheric conditions other than those for which they were specifically developed. Therefore, linearly filtered white noise is not suitable for flight simulation of rotorcraft.

---

[2] Measured time samples are not suitable for real-time flight simulation for the reasons discussed above, but they do provide a way to reproduce actual flight scenarios in a controlled and repeatable environment.

2.3.3 Summation of Sinusoids

With the advent of high-speed digital computers, the summation of sinusoids promises to become the standard technique of atmospheric turbulence modeling for flight simulation. A velocity field matching the frequency content and amplitude statistics of the intended atmospheric turbulence field may be reconstructed by a series of sinusoids with weighted amplitudes, specially chosen frequencies and uniformly distributed random phases. The summation of sinusoids technique was used for this research. (See Section 3.2.)

2.4 Taylor's Frozen Field Hypothesis

Atmospheric turbulence modeling for flight simulation relies on an assumption known as Taylor's Frozen Field hypothesis [31]. Atmospheric turbulence is obviously a very complicated phenomena which varies both spatially and temporally. However, Taylor found that for a point fixed with respect to the atmosphere frame, the temporal variations in the velocity field are small compared to spatial variations. The implication of this hypothesis is that the turbulence induced responses of the aircraft result almost entirely from the motion of the aircraft relative to the velocity field. The effect of spatial variations of the velocity field is large with respect to the effect of temporal variations of the velocity field. Hence, the velocity field can be considered frozen in time but steadily convecting at the true airspeed with respect to the aircraft. As the aircraft moves through the atmosphere, the statistics of the frozen velocity field are stationary; that is, the statistics of individual patches of turbulence are independent of time. With this assumption, the velocity field produced by the summation of sinusoids is statistically valid, and the turbulence velocity at any point in the atmospheric frame can be calculated.

2.5 Related Work

Recently, there have been several reports which have given detailed accounts of the principle works on modeling atmospheric turbulence for aerodynamic systems [6, 25]. The reader is referred to these works for an extensive review of atmospheric turbulence applications. In this section, only a small subset of those works which direct impacted this investigation of the rotorcraft atmospheric turbulence problem are discussed.

2.5.1 Wind Turbine Research

The first theoretical work investigating the effects of atmospheric turbulence on a rotating wind turbine blade was published by Rosenbrock in 1955 [28]. The Rosenbrock Model used an isotropic frozen field approximation of the atmosphere and exponential approximations of the fundamental correlations. Like fixed wing models, it assumed the atmospheric turbulence velocity was uniform across the rotor disk at any given instant, but unlike previous models, the atmospheric turbulence field was sampled at a "representative" blade station, namely the rotor blade tip. This unique approach yielded the now familiar power spectrum of axial atmospheric turbulence velocities having energy shifted to higher frequencies and peaks centered at integer multiples of the rotor rotational frequency.

In 1977, Pacific Northwest Laboratory validated Rosenbrock's earlier theoretical work by conducting a field experiment to examine the effects of rotational sampling of atmospheric turbulence [35]. The rotation of a hypothetical large horizontal-axis wind turbine was simulated by cyclically sampling the atmosphere using a set of fixed anemometers placed around the circumference of a vertical grid. The resulting power spectrum of axial atmospheric turbulence velocities showed the same qualitative energy shift and peaks at integer multiples of the rotational frequency predicted by Rosenbrock's model. (See Figure 2-4.) Additional field experiments were later conducted using a hot film anemometer on a rotating boom and a circle scanning laser anemometer. These also yielded qualitatively similar results [3].

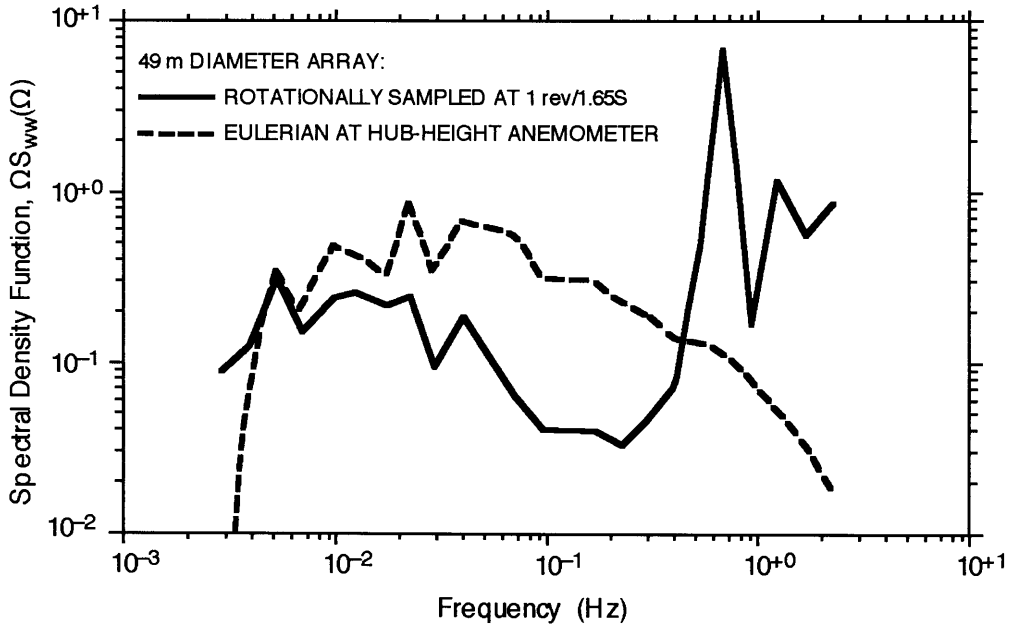

Figure 2-4: Spectra of wind speed fluctuations derived from measurements by rotationally sampling wind speed values around a circular array of anemometers in a vertical plane. Figure is adapted from Connel [3].

A fundamentally different wind turbine model, known as the Sandia Method, was developed by Veers in 1988 [33, 34]. Unlike previous work which attempted to analytically derive the specific atmospheric turbulence statistics sampled by a rotating blade, the Sandia Method computed a fully three-dimensional grid of wind velocities with the same spectral characteristics as the atmospheric turbulence field. A wind turbine blade sampled this velocity field as the field convected and the blade rotated. The main difference between this simulation method and earlier wind turbine methods was that in this simulation, the velocity field was based solely on first-order and second-order statistics without regard to the complex fluid dynamics of the atmosphere. Hence, the biggest advantage of this technique, and similarly the full-field technique developed for this research, was its ability to be easily integrated into a comprehensive wind turbine (or rotorcraft) model. Unfortunately, the Sandia Method generated a grid of atmospheric turbulence velocities. The disadvantage of the well-populated grid was that velocities were then calculated for many points in space and time that the blades would never occupy. This wasted a large amount of storage space and made real-time execution impossible.

2.5.2 Rotary Wing Aircraft Research

Lately, considerable work has been done in the rotorcraft community to adapt the horizontal axis wind turbine models to rotorcraft specific models designed to investigate the effects of atmospheric turbulence on rotorcraft handling qualities. Although numerous studies have investigated these effects, none have achieved real-time pilot-in-the-loop flight simulation.

In 1992, Costello developed a frequency domain model describing the atmospheric turbulence velocity field as sampled by the aerodynamic surfaces of a general tandem rotorcraft [6]. Atmospheric turbulence over any particular rotor blade was approximated by a series of radial and azimuthal shape functions. This model marked a departure from previous rotorcraft atmospheric turbulence models. It used statistics for the velocity field

sampled by the translating and rotating blade element, rather than the statistics for the velocity field sampled by the translating center of gravity of the aircraft. Costello concluded that atmospheric turbulence modeling for rotorcraft needed to be considerably more complex than for fixed wing aircraft. Also, proper modeling of rotational sampling significantly affected both the amplitude and frequency content of the atmospheric turbulence induced disturbances. Cast in the frequency domain, however, this work was not directly applicable to real-time flight simulation.

Concurrent with Costello's work, Riaz developed a time domain method for simulating the vertical component of atmospheric turbulence seen by a translating and rotating helicopter rotor blade [25]. This method used Shinozuka's algorithm to express the atmospheric turbulence field as a series of cosine functions with weighted amplitudes, evenly spaced frequencies and uniformly distributed phase angles [30]. Results of this simulation method also indicated rotorcraft response to rotationally sampled atmospheric turbulence can differ significantly from rotorcraft response to hub-fixed sampled atmospheric turbulence. However, the effects of these differences on flight simulation realism, and more specifically, the pilot perception of these changes, have not been investigated. This method, while in the time domain, was not suitable for real-time execution because of the excessive amount of computations it required to accurately reconstruct the atmospheric turbulence field. Riaz concluded, however, that Shinosuka's algorithm could be adapted to the case of cyclostationary turbulence as seen by the translating and rotating blade element.

2.5.3 Fixed Wing Aircraft Research

One work for fixed wing aircraft deserves mention because it is the only known investigation of aircraft handling qualities using piloted flight simulation with motion cues to compare atmospheric turbulence models. In 1975, Jacobson and Joshi investigated the influence of simulated atmospheric turbulence on fixed wing aircraft handling qualities.

through the use of piloted flight simulation [18]. A modified version of the Dryden atmospheric turbulence model was used for the atmospheric turbulence model. It allowed the turbulence intensities and turbulence length scales to differ for each component of the velocity field in order to reproduce the anisotropy of the atmosphere, and it allowed the turbulence intensities to vary with time in order to reproduce the intermittent and patchy nature of atmospheric turbulence. Pilots evaluated the handling qualities of a simulated aircraft for a constant altitude tracking task through the simulated atmospheric turbulence. It was concluded from these evaluations that handling qualities studies are critically affected by the choice of atmospheric turbulence model.

Chapter 3

Stochastic Model of Atmospheric Turbulence

The purpose of this chapter is to develop the full-field atmospheric turbulence model. The full-field model consists of a computation algorithm adapted from a multidimensional random process algorithm proposed by Borgman [1] and an associated computation scheme specific to this research and capable of real-time piloted flight simulation. Additionally, this chapter includes descriptions of the von Kármán spectral model of atmospheric turbulence and the military specification MIL-F-8785C [32] models of relevant meteorological parameters in the Earth's atmosphere.

3.1 Atmospheric Turbulence Spectral Density Functions

3.1.1 Autospectral Density Functions

The autospectral density function of a random process provides statistical information about the average contribution to the total process of the individual frequency components. Two forms of autospectral densities for atmospheric turbulence commonly used in engineering simulations are the von Kármán model, and its rational approximation, the Dryden model [11, 36]. In some instances, the Dryden model has been used in place of the von Kármán model, because it is numerically easier to simulate rational spectra rather than irrational ones. However, experimental data show that the autospectral densities of atmospheric turbulence decrease asymptotically according to the $^{-5}/_{3}$ power of spatial

frequency for high frequencies [9]. The von Kármán model accurately represents this behavior, while the Dryden model approximates it with a high frequency asymptote equal to the –2 power of spatial frequency. Since the von Kármán model is the better fit to experimental data, it was used for this research.

The two-dimensional von Kármán autospectral densities are

$$S_{uu}(\Omega_1,\Omega_2)=\frac{\sigma_u^2}{6\pi}(aL_u)^2\frac{1+(aL_u)^2\left(\Omega_1^2+\frac{11}{3}\Omega_2^2\right)}{\left[1+(aL_u)^2\left(\Omega_1^2+\Omega_2^2\right)\right]^{7/3}}\ , \tag{3.1.1}$$

$$S_{vv}(\Omega_1,\Omega_2)=\frac{\sigma_v^2}{6\pi}(aL_v)^2\frac{1+(aL_v)^2\left(\frac{11}{3}\Omega_1^2+\Omega_2^2\right)}{\left[1+(aL_v)^2\left(\Omega_1^2+\Omega_2^2\right)\right]^{7/3}}\ , \tag{3.1.2}$$

$$S_{ww}(\Omega_1,\Omega_2)=\frac{4\sigma_w^2}{9\pi}(aL_w)^4\frac{\left(\Omega_1^2+\Omega_2^2\right)}{\left[1+(aL_w)^2\left(\Omega_1^2+\Omega_2^2\right)\right]^{7/3}}\ , \tag{3.1.3}$$

where

$$a=\frac{\Gamma\left(\frac{1}{3}\right)}{\sqrt{\pi}\Gamma\left(\frac{5}{6}\right)}\approx 1.339\ . \tag{3.1.4}$$

Equations (3.1.1) through (3.1.4) represent the longitudinal, lateral and vertical autospectral densities in terms of streamwise and spanwise spatial frequencies, Ω_1 and Ω_2.[1] A computationally less intense, one-dimensional form of the von Kármán model (streamwise variations only) is also used in engineering simulations, because of its simplicity [29]. Rotorcraft operate almost exclusively at low altitude, where the significant atmospheric scales are their smallest. In this flight regime, it is necessary to include both streamwise and spanwise variations of the turbulence field in the simulation, and a one-dimensional von Kármán model is not acceptable for realistic flight simulation [23]. A three-dimensional form of the von Kármán model which includes streamwise, spanwise and normal variations of the turbulence field also has received limited usage [2]. However, the additional computational requirements of this model—both speed and storage—do not permit real-time execution, and it could not be used for this research.[2] Neglecting normal

[1] Streamwise is in the direction parallel to the mean wind velocity vector, and spanwise is in the direction perpendicular to the mean wind velocity vector.

[2] The increase in computation time and memory usage is equivalent to the increase from N^2 for the two-

variations of the velocity field is acceptable, because the range of rotor blade motion in the normal direction is much smaller than the significant atmospheric scales.[3] Large-scale fluctuations—including the variations with altitude of the mean wind, turbulence intensities and turbulence length scales—are computed separately by an atmosphere model. See Section 3.3.

The autospectral densities described by Equations (3.1.1) through (3.1.4) are dependent upon two fundamental parameters: the turbulence intensity, σ, and turbulence length scale, L. The turbulence intensity is equivalent to the root-mean-square (rms) amplitude of the velocity field. Intuitively, the mean square value of the velocity field is the volume of the region contained by the autospectral density and the $\Omega_1 \cdot \Omega_2$ plane, such that

$$\sigma^2 = \int_{-\infty}^{+\infty} \int_{-\infty}^{+\infty} S(\Omega_1, \Omega_2) d\Omega_1 d\Omega_2 \ . \tag{3.1.5}$$

Thus, the level of fidelity between the intended statistics, and the actual statistics recovered in the simulated velocity field, is determined by the discretization method used to approximate the continuous autospectral densities.

The other fundamental parameter in the von Kármán model is the turbulence length scale, L. Intuitively, the length scale measures the extent of significant correlation between turbulence velocities at different spatial locations and the same time. Thus, length scales much larger than the aircraft's physical dimensions correspond to a turbulence field that is nearly uniform across the rotor disks, while length scales approaching to the aircraft's physical dimensions correspond to a turbulence field that shows spatial variation across the rotor disks. Moreover, the effects of the turbulence intensity and the turbulence length scale are best understood in terms of their deterministic counterparts, the discrete gust amplitude and the discrete gust frequency. The intensity determines the rms amplitude of the turbulence field, while the length scale

---

dimensional model to N^3 for the three-dimensional model, where N^2 is the number of harmonics in the discrete spectrum.

[3] For a CH-47D, banked at 30°, the maximum height difference between blade elements at the $^3/_4$ radius, on opposite sides of the rotor disk is less than 21 feet.

determines the frequency content of the turbulence field. The independence of these parameters will be used to simplify the discretization of the autospectral densities in Section 3.2.

3.1.2 Limitations of the Spectral Model

The von Kármán autospectral densities are transformed from the spatial frequency domain to the temporal frequency domain by using Taylor's Frozen Field Hypothesis. (See Section 2.4.) The spatial frequency, equivalent to the inverse of the wave number, is related to the temporal frequency of the velocity field sampled by the aircraft by the aircraft's true airspeed components, U_o and V_o. For an aircraft flying trim and level,

$$\Omega_1 = \frac{\omega_1}{U_o}, \tag{3.1.6}$$

$$\Omega_2 = \frac{\omega_2}{V_o}. \tag{3.1.7}$$

Substitution of Equations (3.1.6) and (3.1.7) into Equations (3.1.1) through (3.1.3) yields the von Kármán autospectral densities in terms of the streamwise and spanwise temporal frequencies, ω_1 and ω_2.

$$S(\omega_1, \omega_2) = \frac{1}{V_T^2} S\left(\Omega_1 = \frac{\omega_1}{U_o}, \Omega_2 = \frac{\omega_2}{V_o}\right), \tag{3.1.8}$$

where

$$V_T^2 = U_o^2 + V_o^2 . \tag{3.1.9}$$

Although this research dealt exclusively with the autospectral densities in terms of spatial frequencies, Equation (3.1.8) shows that the Taylor Frozen Field assumption is not satisfied as the aircraft's true airspeed approaches zero, i.e., as $V_T \to 0$. Near this singularity, a frozen field assumption predicts only very slow variations of the velocity field sampled by the aircraft. In this flight condition, temporal variations of the velocity field are no longer negligible as compared to the spatial variations in the atmosphere frame. Instead, the unmodeled effects of temporal changes in the velocity field, such as self-induced turbulence and rotor wake-turbulence field interaction, become important. Under these circumstances, the turbulence field is essentially stationary (in the physical sense)

relative to the aircraft. Therefore, no attempt should be made to use the stochastic model of atmospheric turbulence for flight conditions where the true airspeed becomes small.

3.1.3 Cross-Spectral Density Functions

The cross-spectral density function of two random processes provides statistical information on the correlation between the two processes. For atmospheric turbulence, there are six cross-spectra correlating the u, v and w components of the velocity field. However, only three cross-spectra are independent—the longitudinal-lateral cross-spectrum, S_{uv}, the longitudinal-vertical cross-spectrum, S_{uw}, and the lateral-vertical cross-spectrum, S_{vw}. Much research, theoretical and experimental, has been conducted to quantify these properties of atmospheric turbulence [22]. In the Earth's boundary layer, it has not been possible to determine any general algebraic form of these cross-spectra, particularly one that includes their dependence on height, heading angle relative to the mean wind and other parameters relevant to flight simulation. Symmetry requires the longitudinal-lateral and lateral-vertical cross-spectra to be identically zero. Experimental data verifies this assumption, but strongly suggests anisotropy results in a non-vanishing longitudinal-vertical spectrum, S_{uw}, at low altitude.

Before implementing the full-field atmospheric turbulence model into Boeing Helicopters' flight simulator, several possible algebraic forms of the longitudinal-vertical cross-spectrum were researched. These cross-spectra are given in References 12 and 24. It was decided that inclusion of a cross-correlation would not significantly enhance the atmospheric turbulence model's performance, while it would greatly complicate real-time execution, since the computation scheme chosen to generate the velocity field is not suitable for incorporating cross-spectra. Therefore, cross-spectra were not included in this research.

3.2 Full-Field Atmospheric Turbulence Computation

3.2.1 Original Computation Scheme

Previous atmospheric turbulence studies for rotorcraft [26] used a time-domain simulation method based on Shinosuka's random process simulation algorithm [30] to generate turbulence sample functions for a translating rotating helicopter rotor blade. These methods use a summation of two-dimensional sinusoids with evenly spaced frequencies and uniformly distributed random phases to reconstruct a velocity field with the correct first-order and second-order statistics. The continuous autospectral density of the turbulence field is discretized by concentrating the spectral energy in each frequency region into individual harmonics with magnitudes equal to the fraction of the total energy contained in each particular region. The research discussed in Reference 26 discretized the spectral densities with a constant linear frequency grid. This is equivalent to a discrete spectrum with spikes at constant linear frequency intervals of $\Delta\Omega_1$ and $\Delta\Omega_2$, each spike having a magnitude equal to $S(\tilde{\Omega}_1,\tilde{\Omega}_2)\Delta\Omega_1\Delta\Omega_2$. Figures 3-1 and 3-2 illustrate the discretization of a sample autospectral density function. The spectral factors of the discrete spectrum are obtained by taking the square root of each spike. Then, using Shinosuka's algorithm, a time simulation of the velocity field is generated by summing these spectral factors. For a two-dimensional autospectral density, the turbulence velocity can be expressed as a function of the blade element's spatial location in the atmosphere frame (X_A, Y_A) by

$$w(X_A,Y_A)=2\sum_{j=1}^{N}\sum_{k=-N}^{N}\sqrt{S\left(\tilde{\Omega}_{1,j},\tilde{\Omega}_{2,k}\right)\Delta\Omega_1\Delta\Omega_2}\,\sin\left(X_A\tilde{\Omega}_{1,j}+Y_A\tilde{\Omega}_{2,k}+\Phi_{jk}\right), \quad (3.2.1)$$

where

$$\tilde{\Omega}_{1,j}=\frac{(2j-1)\Delta\Omega_1}{2}, \quad (3.2.2)$$

$$\tilde{\Omega}_{2,k}=\frac{(2k-1)\Delta\Omega_2}{2}, \quad (3.2.3)$$

$\sqrt{S\left(\tilde{\Omega}_{1,j},\tilde{\Omega}_{2,k}\right)\Delta\Omega_1\Delta\Omega_2}$ is the spectral factor of the discrete spectrum, and $\sin\left(X_A\tilde{\Omega}_{1,j}+Y_A\tilde{\Omega}_{2,k}+\Phi_{jk}\right)$ is its associated two-dimensional harmonic with random

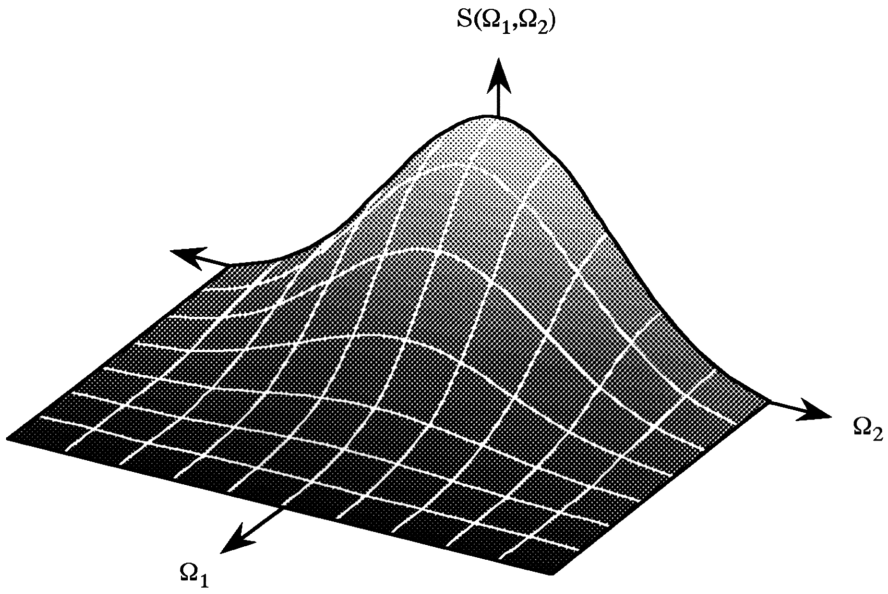

Figure 3-1: Sample Continuous Two-Dimensional Spectrum

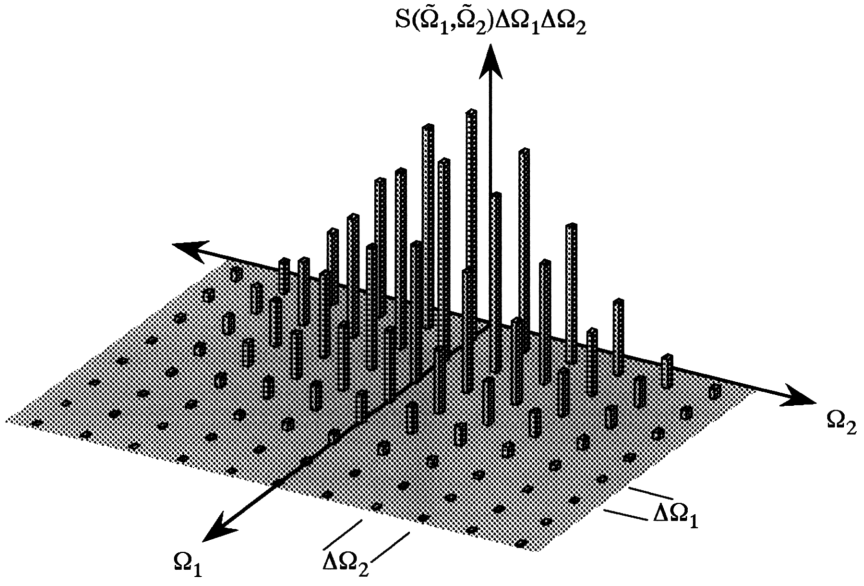

Figure 3-2: Sample Discrete Two-Dimensional Spectrum

phase, Φ_{jk}. This computation scheme is too computationally intensive for real-time execution of the full-field atmospheric turbulence model.

The von Kármán autospectral densities exhibit symmetry, and this topology reduces the execution time by a factor of two when Equation (3.2.1) is simplified to

$$w(X_A, Y_A) = 2\sqrt{2} \sum_{j=1}^{N} \sum_{k=1}^{N} \sqrt{S(\tilde{\Omega}_{1,j}, \tilde{\Omega}_{2,k}) \Delta\Omega_1 \Delta\Omega_2} \sin\left(X_A \tilde{\Omega}_{1,j} + Y_A \tilde{\Omega}_{2,k} + \Phi_{jk}\right) . \quad (3.2.4)$$

Unfortunately, *algebraic* simplification alone will not achieve real time execution of the random process simulation algorithm. Fundamental changes are required.

3.2.2 Limitations of Original Computation Scheme

The discretization method defined by Equations (3.2.2) and (3.2.3) uses a Cartesian spatial frequency grid with the frequency space of interest divided into N^2 equal subdivisions, each $\Delta\Omega_1 \times \Delta\Omega_2$.[4] This method is efficient for discretizing narrowband random processes whose energies are contained within a small frequency bandwidths. However, modifications to the discretization method are required to allow real-time execution of the full-field atmospheric turbulence model.

Two problems associated with Cartesian discretization make it unsuitable for real-time execution. First, a constant linear frequency grid treats all subdivisions of the selected frequency space equally, and there is no weighting of the discretization method for subdivisions with the highest spectral energy density. Instead, every Ω_1 spatial frequency is paired with every Ω_2 spatial frequency to construct the Cartesian frequency grid. This lack of sophistication results in the use of harmonics whose spectral factors are so small that they have a negligible contribution to the fidelity of the random process simulation, while they retain an equal share of the execution time. Also, a Cartesian frequency grid only represents N individual spatial frequencies for N^2 total harmonics. With proper harmonic placement, it is possible to represent nearly N^2 individual spatial frequencies

[4] Each quadrant of frequency space is $N \times N$ subdivisions for a total of $4N^2$ subdivisions.

from N^2 total harmonics. Therefore, Cartesian discretization requires more harmonics, i.e., greater computation time, to attain the same frequency richness as more efficient discretization methods.

Second, the discretization method described by Equations (3.2.2) and (3.2.3) approximates the discrete spectrum by harmonics with magnitudes equal to $S(\tilde{\Omega}_1, \tilde{\Omega}_2)\Delta\Omega_1\Delta\Omega_2$. The exact magnitude of the spectral factor is the integration of the continuous spectrum over its particular frequency subdivision. For small subdivisions, rectangular integration is nearly indistinguishable from analytic integration. However, real-time execution necessitates the use of the fewest harmonics possible. In this circumstance, rectangular integration can adversely affect the fidelity of the full-field atmospheric turbulence simulation. As discussed for Equation (3.1.5), the double integration of a continuous spectrum over all frequency space is the mean square value of the random process. Therefore, a problem affecting the calculation of the discrete spectrum causes discrepancies between the intended mean square value of the process and the actual mean square value recovered during simulation.

Boeing Helicopters previously implemented a similar non-real-time frequency domain atmospheric turbulence model, based on Reference 6, to investigate turbulence induced vibratory loads in the drive system of the CH-47D helicopter [20]. This frequency domain model used rectangular integration and a Cartesian discretization grid similar to that described by Equations (3.2.2) and (3.2.3). During this turbulence study, it was discovered that varying the number of harmonics (while discretizing the same frequency region) caused markedly different spectral results. Indeed, these differences were large enough to be noticed as a deficiency of the computation scheme [21]. Analytic integration solves this computation problem, because the mean-square value of the turbulence field becomes completely decoupled from the number of harmonics in the discrete spectrum. Instead, the number of harmonics determines only the frequency content richness of the simulated velocity field, and does not effect the velocity field's rms amplitude.

3.2.3 Real Time Computation Scheme

A modified random process simulation algorithm, proposed by Borgman for ocean wave simulation [1], was used for this research because it allowed real time execution of the full-field atmospheric turbulence model. Unlike Shinosuka's algorithm that uses equal subdivisions of *frequency* space and rectangular integration of the autospectral densities, Borgman's algorithm uses equal subdivisions of *energy* space and analytic integration. This algorithm defines the harmonics to have equal magnitudes and then solves the integral equation

$$\iint_{\text{freq. region}} S(\Omega_1, \Omega_2) d\Omega_1 d\Omega_2 = \frac{\sigma^2}{4N^2} . \tag{3.2.5}$$

to find the bounds of the individual frequency subdivisions. This contrasts with Shinosuka's algorithm, which defines the frequencies of the harmonics, and then solves the autospectral density function to find the magnitudes. Since Borgman's algorithm uses a set of arbitrarily chosen frequency points, rather than a Cartesian frequency grid, the pair of summations in Equation (3.2.4), each 1 to N, is changed to a single summation in Equation (3.2.5), 1 to N^2. Equation (3.2.5) can be rewritten as

$$w(X_A, Y_A) = 2\sqrt{2} \sum_{l=1}^{N^2} \sqrt{\frac{\int_{-\infty}^{+\infty} \int_{-\infty}^{+\infty} S(\Omega_1, \Omega_2) d\Omega_1 d\Omega_2}{4N^2}} \sin\left(X_A \tilde{\Omega}_{1,l} + Y_A \tilde{\Omega}_{2,l} + \Phi_l\right) . \tag{3.2.6}$$

Substitution of Equation (3.1.5) into Equation (3.2.6) and simplifying, yields

$$w(X_A, Y_A) = \sqrt{2} \frac{\sigma}{N} \sum_{l=1}^{N^2} \sin\left(X_A \tilde{\Omega}_{1,l} + Y_A \tilde{\Omega}_{2,l} + \Phi_l\right) . \tag{3.2.7}$$

Equation (3.2.7) represents the simplest form of the random process simulation algorithm. It requires 72% fewer mathematical operations and 60% less computation time[5] to execute than the less efficient form initially introduced by Equation (3.2.1).

[5] This reduction of execution time is for the random process simulation algorithm only, which accounts for more than 90% of the total execution time of the full-field atmospheric turbulence model. There is additional execution time attributable to the atmosphere model, the coordinate transformations and model I/O.

3.2.4 Exact Integration of the Autospectral Density Functions

This computation scheme requires the autospectral densities to be integrated analytically. As written, Equations (3.1.1) through (3.1.3) cannot be integrated in terms of ordinary algebraic functions. A coordinate transformation converts the autospectral densities to the more appropriate polar coordinates, i.e.,

$$\Omega_1 = \Re\cos\Theta \ , \tag{3.2.8}$$

$$\Omega_2 = \Re\sin\Theta \ . \tag{3.2.9}$$

Substitution of Equations (3.2.8) and (3.2.9) into Equations (3.1.1) through (3.1.3) yields the von Kármán autospectral densities in terms of fictitious radial and azimuthal spatial frequencies, $\Re$ and Θ, so that

$$S_{uu}(\Re,\Theta) = \frac{\sigma_u^2}{6\pi}(aL_u)^2 \frac{1+(aL_u\Re)^2\left[1+\frac{8}{3}\sin^2\Theta\right]}{\left[1+(aL_u\Re)^2\right]^{7/3}} \ , \tag{3.2.10}$$

$$S_{vv}(\Re,\Theta) = \frac{\sigma_v^2}{6\pi}(aL_v)^2 \frac{(aL_v\Re)^2\left[1+\frac{8}{3}\cos^2\Theta\right]}{\left[1+(aL_v\Re)^2\right]^{7/3}} \ , \tag{3.2.11}$$

$$S_{ww}(\Re,\Theta) = \frac{4\sigma_w^2}{9\pi}(aL_w)^4 \frac{\Re^2}{\left[1+(aL_w\Re)^2\right]^{7/3}} \ . \tag{3.2.12}$$

Substitution of Equations (3.2.8) and (3.2.9) into Equation (3.2.5) yields the polar form of the integral equation that defines the bounds of the frequency subdivisions:

$$\int_{\Theta_1}^{\Theta_2}\int_{\Re_1}^{\Re_2} S(\Re,\Theta)\Re\, d\Re\, d\Theta = \frac{\sigma^2}{4N^2} \ . \tag{3.2.13}$$

Thus, the frequency subdivisions correspond to polar sectors rather than Cartesian rectangles in frequency space. The polar autospectral densities, Equations (3.2.10) through (3.2.12), can be integrated by parts to yield

$$\int_{\Theta_1}^{\Theta_2}\int_{\Re_1}^{\Re_2} S_{uu}(\Re,\Theta)\Re\,\partial\Re\,\partial\Theta = -\frac{\sigma_u^2}{4\pi}\left\{\frac{\left[1+\frac{4}{3}(aL_u\Re)^2\right]}{\left[1+(aL_u\Re)^2\right]^{4/3}}\Theta\Big|_{\Theta_1}^{\Theta_2} + \frac{\left[1+\frac{4}{3}(aL_u\Re)^2\right]}{\left[1+(aL_u\Re)^2\right]^{4/3}}(7\Theta-2\sin 2\Theta)\Big|_{\Theta_1}^{\Theta_2}\right\}\Bigg|_{\Re_1}^{\Re_2} \ , \tag{3.2.14}$$

$$\int_{\Theta_1}^{\Theta_2}\int_{\Re_1}^{\Re_2} S_{vv}(\Re,\Theta)\Re\,\partial\Re\,\partial\Theta = -\frac{\sigma_v^2}{4\pi}\left\{\frac{\left[1+\frac{4}{3}(aL_v\Re)^2\right]}{\left[1+(aL_v\Re)^2\right]^{8/3}}\Theta\Big|_{\Theta_1}^{\Theta_2} + \frac{\left[1+\frac{4}{3}(aL_v\Re)^2\right]}{\left[1+(aL_v\Re)^2\right]^{4/3}}(7\Theta+2\sin 2\Theta)\Big|_{\Theta_1}^{\Theta_2}\right\}\Bigg|_{\Re_1}^{\Re_2}, \tag{3.2.15}$$

$$\int_{\Theta_1}^{\Theta_2}\int_{\Re_1}^{\Re_2} S_{ww}(\Re,\Theta)\Re\,\partial\Re\,\partial\Theta = -\frac{\sigma_w^2}{2\pi}\left\{\frac{\left[1+\frac{4}{3}(aL_w\Re)^2\right]}{\left[1+(aL_w\Re)^2\right]^{4/3}}\Theta\Big|_{\Theta_1}^{\Theta_2}\right\}\Bigg|_{\Re_1}^{\Re_2}. \tag{3.2.16}$$

The complete derivation of this integration by parts is given in Appendix A. Notice that Equations (3.2.14) through (3.2.16) are functions of a normalized radial frequency, ($aL\Re$). The significance of this result is that the frequency grids can be computed for the specific number of harmonics, N^2, wholly independent of the turbulence intensity, σ, and the turbulence length scale, L. Substitution of Equations (3.2.14) through (3.2.16) into Equation (3.2.13) and simplifying yields the three equalities that define the longitudinal, lateral and vertical normalized frequency grids, so that

$$-\frac{1}{\pi}\left\{\frac{\left[1+\frac{4}{3}\Re_u^2\right]}{\left[1+\Re_u^2\right]^{8/3}}\Theta\Big|_{\Theta_1}^{\Theta_2} + \frac{\left[1+\frac{4}{3}\Re_u^2\right]}{\left[1+\Re_u^2\right]^{4/3}}(7\Theta-2\sin 2\Theta)\Big|_{\Theta_1}^{\Theta_2}\right\}\Bigg|_{\Re_{u,1}}^{\Re_{u,2}} = \frac{1}{N^2}, \tag{3.2.17}$$

$$-\frac{1}{\pi}\left\{\frac{\left[1+\frac{4}{3}\Re_v^2\right]}{\left[1+\Re_v^2\right]^{8/3}}\Theta\Big|_{\Theta_1}^{\Theta_2} + \frac{\left[1+\frac{4}{3}\Re_v^2\right]}{\left[1+\Re_v^2\right]^{4/3}}(7\Theta+2\sin 2\Theta)\Big|_{\Theta_1}^{\Theta_2}\right\}\Bigg|_{\Re_{v,1}}^{\Re_{v,2}} = \frac{1}{N^2}, \tag{3.2.18}$$

$$-\frac{8}{\pi}\left\{\frac{\left[1+\frac{4}{3}\Re_w^2\right]}{\left[1+\Re_w^2\right]^{4/3}}\Theta\Big|_{\Theta_1}^{\Theta_2}\right\}\Bigg|_{\Re_{w,1}}^{\Re_{w,2}} = \frac{1}{N^2}, \tag{3.2.19}$$

where

$$\Re_u = aL_u\Re, \tag{3.2.20}$$

$$\Re_v = aL_v\Re, \tag{3.2.21}$$

$$\Re_w = aL_w\Re. \tag{3.2.22}$$

Prior to flight simulation, the normalized frequency grids can be calculated to save a considerable amount of computation time. Then, during flight simulation, the normalized frequency grids can be scaled with the turbulence length scale to achieve the appropriate atmospheric condition. Thus, the length scale can be varied continuously (as a function of altitude) during real-time execution without requiring the costly recalculation of the

frequency grid. This capability is not possible with the original computation scheme described by Equations (3.2.1) through (3.2.3), since the spectral factors, $\sqrt{S\left(\tilde{\Omega}_{1,j},\tilde{\Omega}_{2,k}\right)\Delta\Omega_1\Delta\Omega_2}$, are nonlinear functions of length scale that cannot be calculated prior to flight simulation.

3.2.5 Frequency Bounds of the Discrete Spectra

The frequency range spanned by the continuous spectrum is infinite, while the frequency range of the discrete spectrum must be finite. Analytic integration allows the difference between the energies of the discrete and continuous spectra, i.e., the mean-square value of the velocity field corresponding to the finite frequency range of the discrete spectrum to be arbitrarily chosen. For this research, the error in the mean-square value of the velocity field was set at two percent of the intended turbulence intensity.[6] Thus, to satisfy this accuracy requirement, the discretized region of the continuous spectrum will contain 98% of the total spectral energy.

Incidentally, this region spans four decades in the radial direction for the two-dimensional polar von Kármán autospectral densities. Clearly, for each decade to contain enough harmonics to retain adequate frequency richness, too many harmonics would be needed for the Cartesian discretization grid.

The integration bounds of Equation (3.2.13) determine the spatial frequency ranges of the normalized frequency grid. The frequency grid is centered in the autospectral density's energy space, so the frequency ranges of interest are the normalized radial frequency that spans 1% of the spectral energy, given by

$$\int_{\Theta=0}^{2\pi}\int_{\mathfrak{R}=0}^{\mathfrak{R}_{0.01}} S(\mathfrak{R},\Theta)\mathfrak{R}\partial\mathfrak{R}\partial\Theta = 0.01\sigma^2 \ , \tag{3.2.23}$$

and the normalized radial frequency which spans 99% of the spectral energy, given by

[6] This is equivalent to a 1% error in the root-mean-square value of each turbulence field component.

$$\int_{\Theta=0}^{2\pi}\int_{\Re=0}^{\Re_{0.99}} S(\Re,\Theta)\Re\,\partial\Re\,\partial\Theta = 0.99\sigma^2 \,. \tag{3.2.24}$$

Substitution of Equations (3.2.17) through (3.2.22) into Equations (3.2.23) and (3.2.24) yields the normalized radial frequency ranges. The 1% and 99% normalized frequency ranges for the longitudinal, lateral and vertical von Kármán autospectral densities are listed in Table 3.1.[7] Appendix B gives the percentiles of the spectral energy bounded by the origin and any normalized radial frequency for the von Kármán autospectral densities.

Table 3.1: Normalized Radial Spatial Frequency Ranges for the von Kármán Autospectral Density Functions

Velocity Component	$aL\Re_{0.01}$	$aL\Re_{0.99}$
Longitudinal Spectrum	0.2441	1260.1
Lateral Spectrum	0.2441	1260.1
Vertical Spectrum	0.5031	1539.6

The autospectral densities are then discretized over these frequency ranges by iterating Equations (3.2.17) through (3.2.19). However, these equations do not uniquely determine the normalized frequency grids. A constituitive relationship linking the radial and azimuthal frequency increments must be assumed. This research used frequency subdivisions that, while being radial sectors, remained generally rectangular in shape. This geometric constraint was achieved by including additional logic with the discretization method to keep the radial incremental distance of each subdivision approximately equal to its azimuthal incremental distance. Note that this requirement cannot be used as a strict equality, since the azimuthal increment *must* be an integer divisor of the radial frequency range of a quadrant, 0 to $\pi/2$. The complete discretization method is given by

$$\frac{(\Theta_2-\Theta_1)}{2\pi}\cdot\frac{(\Re_2+\Re_1)}{2}\approx(\Re_2-\Re_1)\,, \tag{3.2.25}$$

$$\Theta_2-\Theta_1=\frac{\pi}{2n}\ \{n\colon n \text{ is an integer, } n\geq 2\}\,. \tag{3.2.26}$$

[7] The azimuthal spatial frequency ranges are 0 to 2π.

These additional constraints ensure that the individual harmonics are suitable discrete approximations to the continuous frequency subdivisions they represent, since the bounds of each frequency subdivision are approximately equidistant from its harmonic. When Equations (3.2.17) through (3.2.19) and Equations (3.2.25) and (3.2.26) are iterated with respect to the frequency increments, $\Delta\Re\ (\Re_2 - \Re_1)$and $\Delta\Theta\ (\Theta_2 - \Theta_1)$ the resultant discrete harmonics are weighted by energy density. Thus, regions of the continuous autospectra with the highest energy density will correspond to regions of the discrete spectra with the most harmonics.

Finally, for time simulation, the radial and azimuthal spatial frequencies of the individual harmonics are transformed back into Cartesian spatial frequencies for the random process simulation algorithm of Equations (3.2.8) and (3.2.9). Figures 3-3 through 3-5 present the normalized frequency grids for the longitudinal, lateral and vertical autospectral densities, respectively. These frequency grids contain 225 total harmonics, and are the grids used for this research.

3.3 Statistical Description of the Atmosphere

It is obvious that before the effects of atmospheric turbulence on rotorcraft performance may be investigated, a reasonable mathematical description of the Earth's atmosphere must be made. In the previous sections, a stochastic definition of the turbulence field was defined in terms of two fundamental parameters, the turbulence intensity, σ, and the turbulence length scale, L. These model parameters need to be related to the general meteorological conditions of the physical atmosphere. Because of its complexity, no single set of formulae is adequate to describe all conditions. However, in the absence of empirical formulae for a specific geographic location, the following model can be considered representative and useful for deducing the basic trends. The structure of atmospheric turbulence at low altitude is quite different from its structure at high altitude, and the models representative of these atmosphere zones are described in the next two sections.

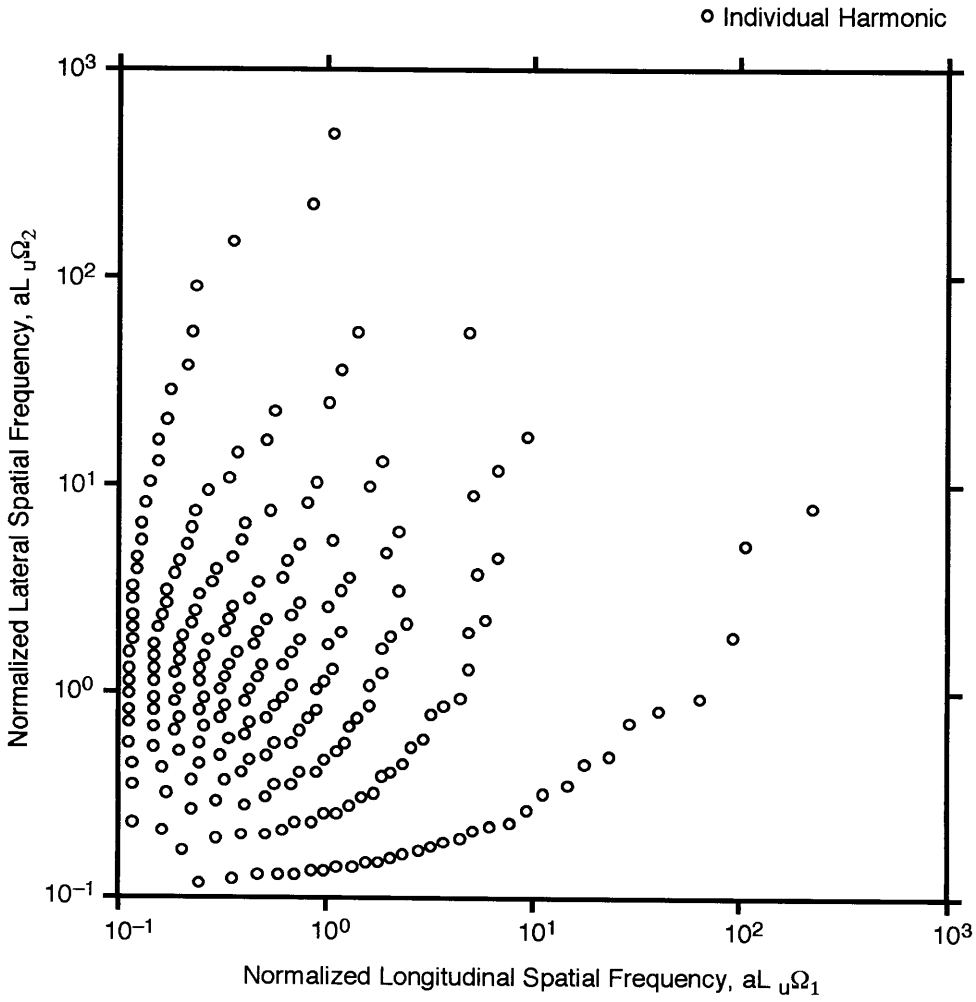

Figure 3-3: Normalized Spatial Frequency Grid for the Discrete von Kármán Longitudinal Autospectral Density Function (N=225 harmonics)

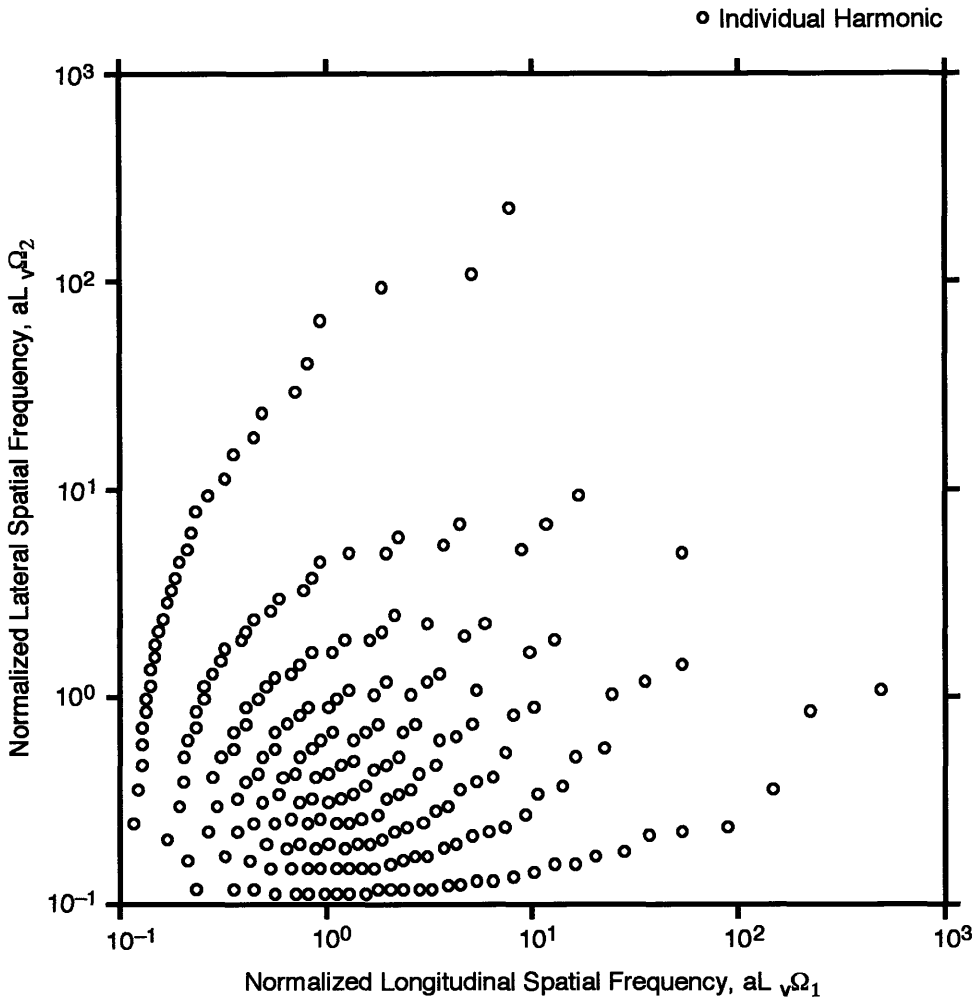

Figure 3-4: Normalized Spatial Frequency Grid for the Discrete von Kármán Lateral Autospectral Density Function (N=225 harmonics)

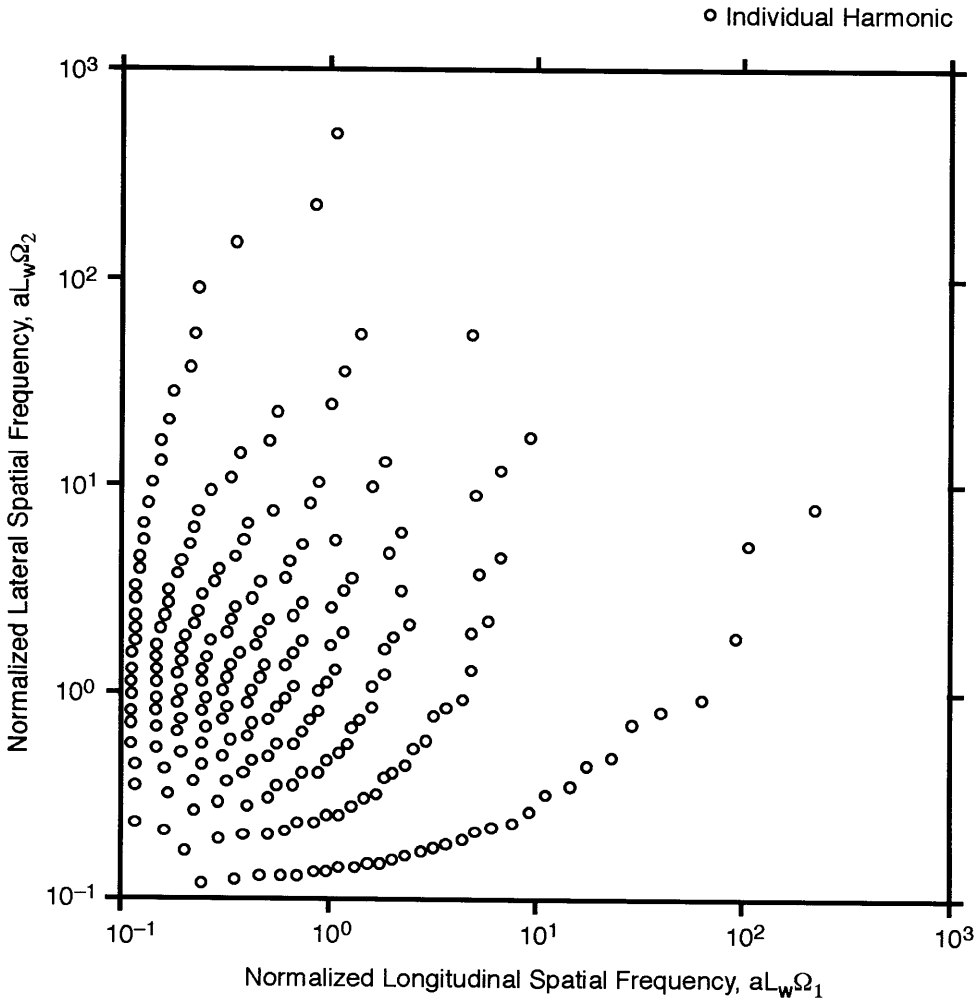

Figure 3-5: Normalized Spatial Frequency Grid for the Discrete von Kármán Vertical Autospectral Density Function (N=225 harmonics)

Additional discussion of these atmosphere models may be found in References 5 and 32.

3.3.1 Low Altitude Atmosphere Structure

The Earth's boundary layer is the region of the atmosphere that extends from the surface up to an altitude of approximately two thousand feet. The typical structure of atmospheric turbulence throughout this region is shown in Figure 3-6, the spectrum of horizontal wind velocities measured by an anemometer fixed with respect to the Earth [12]. The area under the $\omega S_{uu}(\omega)$ curve represents the fraction of wind energy contained in a particular frequency band. Figure 3-6 shows a distinct gap between the low frequency energies of large-scale atmospheric phenomena and the high frequency energies of turbulent motion. Thus, the existence of this gap justifies the division of the atmospheric wind vector into a deterministic slowly varying mean wind component, and a stochastic, rapidly varying turbulence component.

The spectral peak associated with mean wind fluctuations occurs near 0.01 cycles per hour. Thus, the mean wind velocity vector will be assumed constant for the relatively short duration of the flight simulation. At altitudes below 300 feet, the mean wind increases with altitude and has a velocity profile similar to boundary layer flow over a flat plate. This classical logarithmic relationship [32] is described by

$$V_{MW}(h) = V_{MW}(20)\frac{\ln(h/h_0)}{\ln(20/h_0)} \quad . \tag{3.3.1}$$

The mean wind at an altitude of 20 feet, $V_{MW(20)}$, is a reference velocity, and it is common engineering practice to express this reference velocity as a function of its probability of exceedance. The empirical distribution used for this research is taken from Reference 32, and is shown in Figure 3-7. The typical reference velocities corresponding to various qualitative levels of turbulence intensity are indicated. At altitudes above 300 feet, the mean wind is modeled as the velocity calculated for an altitude of 300 feet.

The spectral peak associated with turbulent motions occurs near 50 cycles per hour. At altitudes below 300 feet, experimental data indicates the structure of the velocity field is

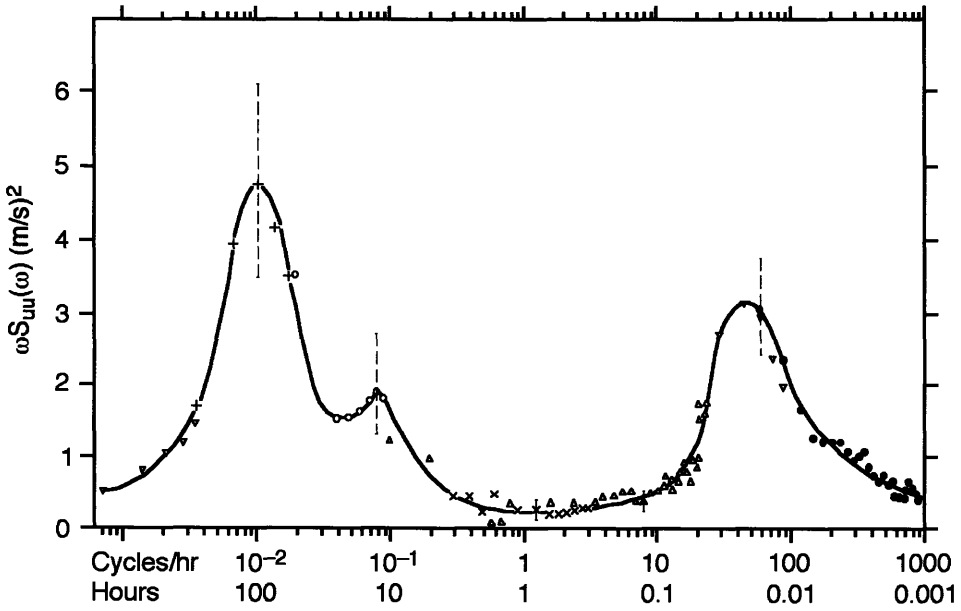

Figure 3-6: Spectrum of Wind Speeds at Low Altitude

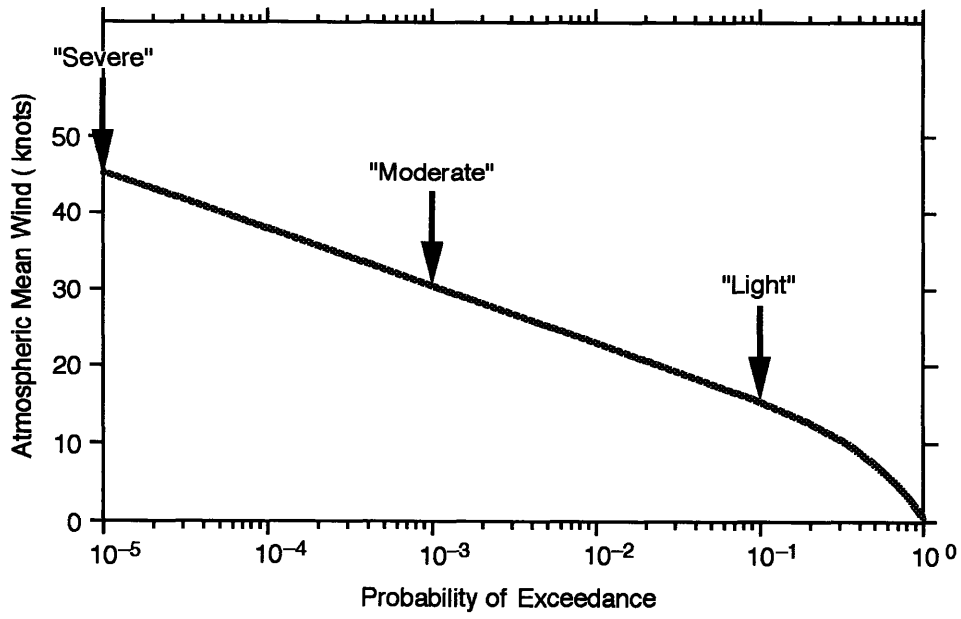

Figure 3-7: Probability of Exceeding the Mean Wind Velocity at 20 feet

anisotropic [12], and the turbulence intensities are different for each velocity component. A representative description of this behavior is given by

$$\sigma_u(h) = 0.10 \frac{V_{MW}(h)}{\ln(h/h_0)}, \tag{3.3.2}$$

$$\sigma_v(h) = 0.08 \frac{V_{MW}(h)}{\ln(h/h_0)}, \tag{3.3.3}$$

$$\sigma_w(h) = 0.05 \frac{V_{MW}(h)}{\ln(h/h_0)}. \tag{3.3.4}$$

Notice, the low altitude model atmosphere model expresses the mean wind and turbulence intensities as functions of a terrain roughness, h_o. Typical values of this parameter for different ground cover and terrain are shown in Table 3.2. A terrain roughness of 1.0 feet was used for this research.

Table 3.2: Typical Terrain Roughness Length Scales

Ground Cover and Terrain	h_o (feet)
Mud Flats, Ice	0.00003 to 0.0001
Smooth Sea	0.0007 to 0.001
Sand	0.0003 to 0.003
Snow Surfaces	0.003 to 0.02
Mown Grass (0.01m)	0.003 to 0.03
Low Grass, Steppe	0.03 to 0.13
Fallow Field	0.07 to 0.1
High Grass	0.13 to 0.33
Forest and Woodland	0.33 to 3.3
Suburbia	3.3 to 6.6
City	3.3 to 13

Inside the Earth's boundary layer, the turbulence length scales increase with altitude. It is important to include this variation for flight simulation, because at low altitude, the length scales are of an order equal to the physical dimensions of the rotorcraft. The equations describing the length scale variation with altitude [32] are

$$L_u(h) = \frac{h}{(0.177 + 0.000823h)^{1.2}}\ , \tag{3.3.5}$$

$$L_v(h) = \frac{h}{(0.177 + 0.000823h)^{1.2}}\ , \tag{3.3.6}$$

$$L_w(h) = h\ . \tag{3.3.7}$$

This atmosphere model is only one of many relating the meteorological parameters to altitude, and most models can be useful for deducing the basic trends. More in-depth investigation requires empirical models for a specific geographic region and flight condition to be used, and their results cannot be extended beyond the limited scope of their physical relevance. However, this atmosphere model allows a convenient comparison of results obtained with the full-field atmospheric turbulence model to previous results obtained with other atmospheric turbulence models available at Boeing Helicopters. Currently, Boeing Helicopters uses this atmosphere model outlined in Reference 32 for flight simulation.

3.3.2 Medium and High Altitude Atmosphere Structure

Experimental data on atmospheric turbulence indicates that outside the Earth's boundary layer, the structure of atmospheric turbulence becomes isotropic. This means that the turbulence intensities and turbulence length scales are equal in every direction. The high altitude atmosphere model begins at an altitude of 2000 feet. To ensure a smooth transition between the otherwise discontinuous low altitude and high altitude models, the turbulence intensities are linearly interpolated between the altitudes of 300 feet and 2000 feet. Similarly, the length scales are linearly interpolated between the altitudes of 1000 feet and 2000 feet. Figure 3-8 shows the turbulence intensity as a function of its probability of exceedance for altitudes above 2000 feet. Again, the various qualitative levels of turbulence intensity are noted and these correspond those noted for the reference mean wind velocity calculation in Section 3.3.1.

Unlike the low altitude model, the high altitude model represents the length scale as a constant, invariant with altitude. Here, the length scale is much larger than the aircraft's physical dimensions. The high altitude length scale used for this research was 2500 feet.

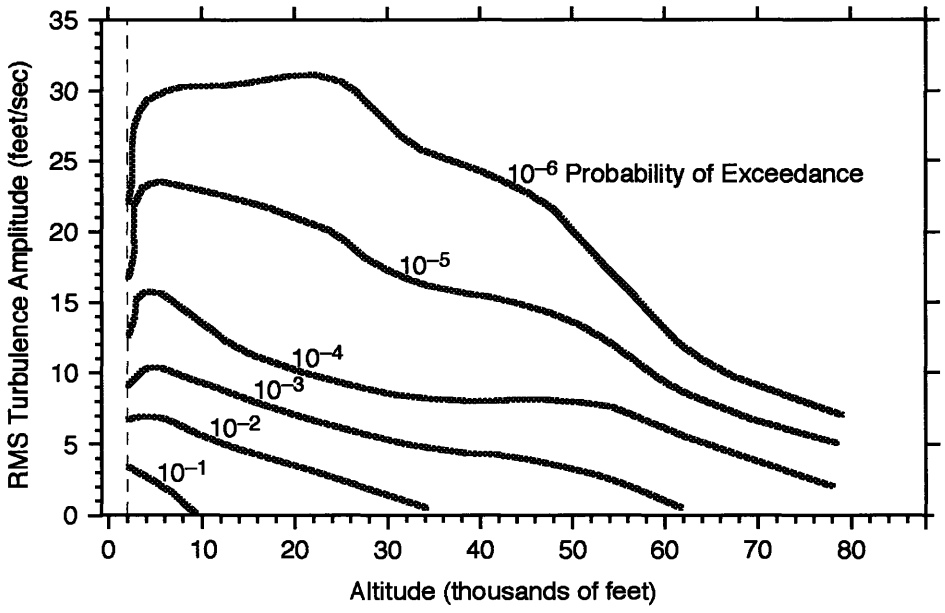

Figure 3-8: Probability of Exceeding Turbulence Intensity

3.4 Non-Gaussian Structure of Atmospheric Turbulence

The full-field atmospheric turbulence model developed in Section 3.2 uses a uniform distribution for the random phase of the individual harmonics. Therefore, by the Central Limit Theorem[8], the summation of these harmonics results in a Gaussian velocity field. Figure 3-9 presents field experiment data from References 10 and 24. Shown are cumulative probability distributions of vertical gusts for several atmospheric turbulence cases. Figure 3-9 is a linear-normal plot, which represents Gaussian processes by straight lines. Notice, the departure of the measured velocity distributions (the light dashed lines) from the Gaussian process (the heavy solid line) indicating an increased probability of large amplitude gusts. Additional field experiment data verifying this non-Gaussian behavior of atmospheric turbulence, particularly at low altitudes, is discussed in Reference 9.

The full-field atmospheric turbulence model approximates the non-Gaussian structure of the velocity field by scaling each Gaussian velocity as a function of its magnitude [24]. This modified velocity is then used for the flight simulation. The heavy dotted line in Figure 3-9 shows the non-Gaussian cumulative probability distribution used for this research. Given a Gaussian velocity, w, the non-Gaussian velocity is described by

$$w_{non-gaussian} = \begin{cases} w_{gaussian} & |w| \le N_{cut}\sigma \\ N_{gauss}\left(w_{gaussian} - N_{cut}\sigma\right) + N_{cut}\sigma & |w| > N_{cut}\sigma \end{cases} . \qquad (3.4.1)$$

where N_{gauss} and N_{cut} are constants estimated from the field experiment data presented in Figure 3-9. Equation (3.4.1) is not meant to be an analytical model of the non-Gaussian structure of atmospheric turbulence. Instead, it is meant to show that magnitude scaling enables a non-Gaussian probability distribution for encounters with large amplitude ($|w| > 2\sigma$) gusts to be easily integrated into the flight simulation without affecting the spectral statistics of the velocity field.

[8] The Central Limit Theorem states that the summation of N identically distributed independent random variables has an asymptotically normal distribution as $N \to \infty$.

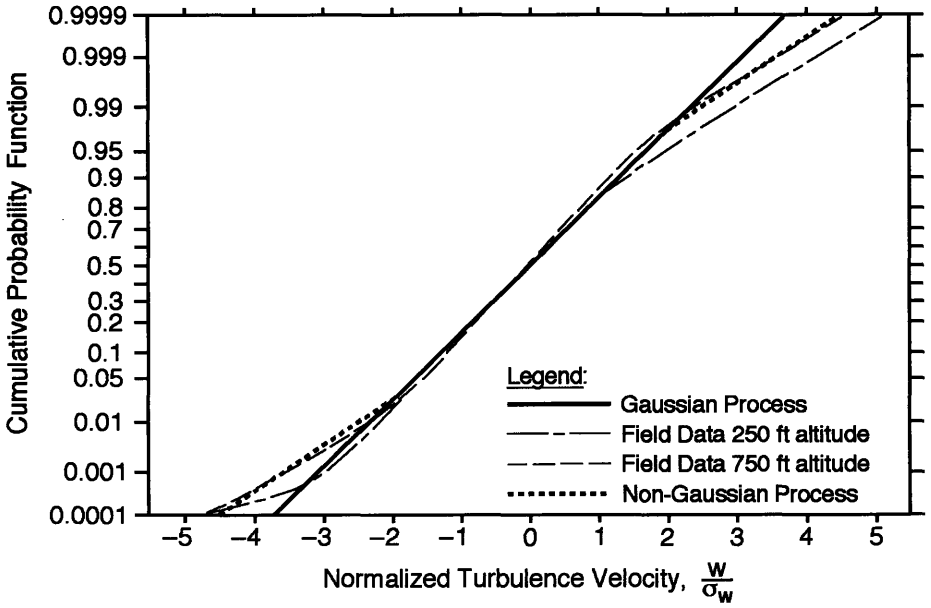

Figure 3-9: Non-Gaussian Cumulative Probability Distributions of Atmospheric Turbulence Velocities

3.5 Real-Time Issues of the Full-Field Model

The full-field atmospheric turbulence model developed in Sections 3.1 through 3.4 is considerably more efficient than earlier models but it remains extremely computationally intensive because of the large number of harmonics involved in the summation. To allow real-time execution, two important implementation requirements need to be satisfied.

First, the full-field model must be interfaced with a rotorcraft simulator that uses a blade-element rotor model for its aerodynamic calculations. The blade element rotor model treats each blade as a separate degree of freedom, thus allowing the framework for analytically simulating the blade forces, moments and motion. This allows the turbulence induced changes of *local* blade angle of attack to affect the state of the aircraft. Classical actuator disk models do not model spatial variations of the rotor states across the disk, so full-field atmospheric turbulence models cannot be used with them. Typically for real-time execution, five blade elements are included in the calculations.[9] While the full-field model is capable of generating the turbulence sample functions for any number of blade elements, the computational requirements realistically limit this number to a single blade station. Therefore, for this research, the full-field model samples the velocity field at each $^3/_4$ radius blade station and uses this velocity along the entire length of the corresponding blade. The $^3/_4$ radius serves as a representative blade station.[10] This assumption has been shown to be adequate for obtaining reasonably accurate blade responses in the wind turbine community [23] and in the rotorcraft community [37].

The other requirement is that the full-field model should be interfaced with computer hardware that allows parallel processing. For this research, the full-field model was executed in parallel on four fully dedicated processors. Thus, each of these processors handled only one-quarter of the computational workload due to the full-field atmospheric

[9] Both Sikorsky Helicopter's GenHel and Boeing Helicopter's BHSim use 5 blade stations for their blade element rotor models.

[10] Reference 37, from the wind turbine community finds that the 80% radius blade station is actually the best approximation to use for single point sampling of atmospheric turbulence.

turbulence model. Three additional processors were fully dedicated to the blade element rotor model. Technically, parallel processing is not necessary, but a machine whose single processor contains the computational power capable of real-time *serial* execution of the blade-element rotor model and the full-field atmospheric turbulence model is neither readily available nor cost effective for flight simulation. Further, parallel processing allows reduction of the overall simulation time frame without increasing the CPU speed of the individual processors, because it executes separate parts of the math model simultaneously. Section 4.2 discusses the simulation architecture used for this research.

Chapter 4

The Flight Simulation Experiment

This chapter describes the flight simulation atmospheric turbulence experiment conducted at Boeing Helicopters' Flight Simulation Laboratory, including detailed descriptions of the flight simulation hardware and software, the atmospheric turbulence cases, the pilot tasks and the pilots' flight experience. The goal of the flight simulation experiment was to determine whether pilots perceive any differences in the overall turbulence simulation realism between the Hub-Fixed model and the Full-Field models. For this, the pilots executed a series of maneuvers while trying to minimize any turbulence-induced aircraft excursions. Later, the pilots responded to a survey of questions about the realism of the atmospheric turbulence simulation.

4.1 Aircraft Simulated

This research was conducted exclusively at Boeing Helicopters' Flight Simulation Laboratory in Philadelphia, PA. This facility supports the flight simulation programs for three different aircraft: the CH-47 Chinook, the V-22 Osprey and the RAH-66 Comanche. The purpose of this research was to determine the extent of possible benefits to flight simulation realism gained by using more complicated atmospheric turbulence models, like the Full Field model. Recall that such atmospheric turbulence models require the flight simulation to include a blade element rotor model in its aerodynamic calculations. This

prerequisite limited the choice of which aircraft to simulate to the CH-47 or the RAH-66, because the V-22 simulation currently relies on aerodynamic table look-ups, rather than a blade element rotor approach. While the RAH-66 has the more popular single main rotor design, it is still in the validation/demonstration stage of development, so pilots do not have firsthand experience flying this aircraft. Conversely, the CH-47 family of tandem main rotor helicopters has been in service since the 1960's, and it is currently undergoing modernization which will extend its service lifetime well into the future. Thus, the handling qualities of the CH-47D are well documented, and a large supply of experienced pilots are readily available for participation in the flight simulation experiment. It was decided that the pilots needed to have experience with the actual aircraft in order to offer the best assessments of the simulated turbulence. Clearly, this is not possible with the RAH-66, so the CH-47D was the aircraft simulated for this research. See Figure 4-1.

The CH-47D Chinook, manufactured by Boeing Helicopters, is a 34% overlapped tandem rotor medium-lift helicopter with three, 30 foot radius, 32 inch chord blades per rotor system. It has a maximum gross weight of 54,000 pounds and an operating empty weight of 24,000 pounds. Cruise velocity is 137 knots and maximum velocity is 174 knots.. A medium gross weight configuration of 33,000 pounds was used for this research.[1] The flight control system consists of mechanical and automatic system components which mix the pilot's control inputs to produce collective and cyclic pitch commands at the rotor heads. The CH-47D includes a Stability Augmentation System (SAS) in its automatic flight control system to provide artificial rate damping in the pitch, roll and yaw axes. The pilot uses this system to hold steady attitudes and rates during hands-off operation. A detailed description of the CH-47 is contained in Reference 14. The dimensional stability derivatives of the CH-47D are listed in Appendix C for flight conditions of 20, 60 and 100 knots true airspeed.

[1] This configuration represents a CH-47D with a full complement of fuel but without any cargo.

Figure 4-1: Boeing CH-47D Chinook Tandem Rotor Helicopter

4.2 Flight Simulation Software

The Boeing Helicopters' simulation math model is a total force, full flight envelope, real-time six degree-of-freedom generic tandem rotor helicopter model. A blade element rotor model, based on the NASA-Ames GENHEL [16, 17, 19] rotor model is integrated into the simulation. Each rotor blade is composed of five blade segments whose individual forces and moments are summed to determine the total forces and moments acting on the aircraft at each of the rotor hubs. For this research, radial flow effects were not included in these force and moment calculations. Rotor inflow was calculated by an extended classical approximation of the uniform component, λ_o, and the first harmonic components, λ_{1c} and λ_{1s}. Nonlinear rotor flapping dynamics were included in the simulation. Rotor-on-rotor interference, usually computed from wind tunnel derived factors, was unintentionally omitted from the simulation. Also, higher frequency rotor dynamics, including lead-lag motion and elastic blade motion, were not calculated because of numerical stability problems related to the size of the overall time frame.

The aircraft model was executed on the IRIS7, a Silicon Graphics 4D/480 computer with 8–36 mips (millions of instructions per second) processors, while the control system model was executed on the MPS4, a Concurrent 3280 MultiProcessing System with 4–6 mips processors. During every time frame, the following procedure is completed by the flight simulation software: At the beginning of the time frame, the major components of the aircraft model are executed by a single parent processor on the IRIS7. These calculations include the engine model, the landing gear model, the fuselage aerodynamic model, etc. At the appropriate instance during the time frame, this parent processor signals two child processors, and these three processors execute the computationally intensive blade element rotor model in parallel. Upon completion of the blade element rotor model, the child processors exit to a wait state, and control is regained by the parent processor. Next, a final set of aircraft model calculations (including the summation of the body forces and moments) for the time frame is executed in the parent processor. Then, the

IRIS7 passes control to the MPS4, which executes the flight control system model. The time frame is complete when control is passed back to the IRIS7, and the aircraft model is initialized for the next time frame. The full-field atmospheric turbulence model is calculated in parallel with this entire procedure on the other four IRIS7 processors. Once per time frame, the parent processor on the IRIS7 receives a set of atmospheric turbulence velocities from these four child processors to be used in its calculation of the local blade angles of attack. This parallel execution is completely transparent to the rest of the simulation and allows the whole time frame to be used for calculations of the velocity field.

Although the aircraft model and the full-field atmospheric turbulence model could be executed in less than ten milliseconds per time frame, additional computation time was necessary for the communication between the IRIS7 and MPS4 computers and I/O to the motion base hardware, strip chart recorders, and magnetic tape drives. To minimize the effective overall time frame, and thereby increase numerical stability, the blade element rotor model was sub-iterated 5:1 with the aircraft and control system models [27]. This computation technique allows the faster rotor dynamics to be integrated five times per time frame while the slower body dynamics are integrated only once per time frame. Figure 4-2 shows this computation technique in flowchart form.

The minimum overall time frame achieved for real-time simulation (therefore, the time frame used for this research) was 50 milliseconds, i.e., a simulation update rate of 20 Hertz. According to Nyquist sampling theory, a rate of $2W$ Hertz is the minimum sampling rate required to preserve all the spectral content information of a continuous signal contained in the bandlimit less than W Hertz. Therefore, an overall time frame of 50 milliseconds is only able to preserve the atmospheric turbulence energy in the frequency band less than 10 Hertz, and the atmospheric turbulence energy in the frequency band greater than 10 Hertz will not be present in the simulation.

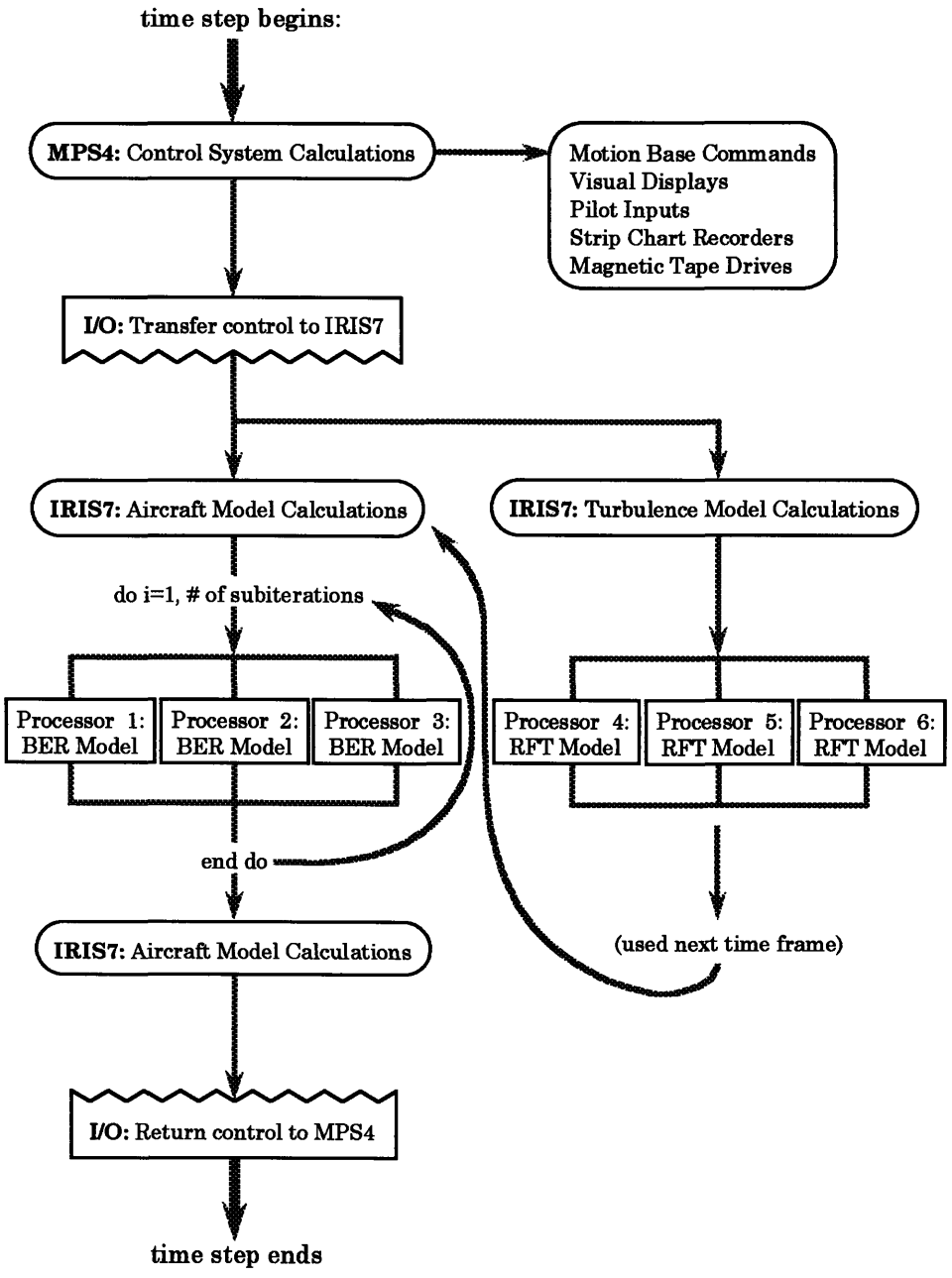

Figure 4-2: Flowchart of Real-Time Simulation Methodology

4.3 Flight Simulation Hardware

The Boeing Helicopters' six degree-of-freedom, motion-base flight simulator was used for this research. (See Figure 4-3) The synergistic motion base assembly consists of six 22 inch stroke hydraulic cylinders which generate the motion cues for the simulator. As a result of these relatively short stroke lengths, the overall cab travel is quite restricted in the translational and rotational degrees-of-freedom. Table 4.1 shows a set of nominal performance specifications given by the motion base manufacturer. These values are based on single degree-of-freedom motion, so simultaneous excursions in multiple degrees-of-freedom limit the overall cab travel further. The motion cues are computed from the double time integration of the aircraft accelerations. To prevent the motion base from contacting its mechanical stops, the aircraft's attitudes and velocities are not integrated, and the aircraft accelerations are hard limited[2] and passed through washout filters.

4.4 Experiment Cases

The flight simulation experiment consisted of three atmospheric turbulence model test cases, each based on a slightly different method for sampling the velocity field.

4.4.1 Hub-Fixed Turbulence Model

This model duplicated the Linearly Filtered White Noise turbulence model, which is the standard atmospheric turbulence model of Boeing Helicopters' flight simulation. The original LFWN method was not working properly, and could not be used for the flight simulation experiment. The Hub-Fixed Turbulence model sampled the turbulence velocities at the aircraft's center-of-gravity and treated these velocities as simple perturbations of the aircraft's total velocities: u, v and w. The turbulence velocity field for the Hub-Fixed Turbulence model was constructed using a summation of sinusoids.

[2] Translational accelerations were hardlimited to 0.25 g's, and rotational accelerations were hardlimited to 0.50 rad/sec^2

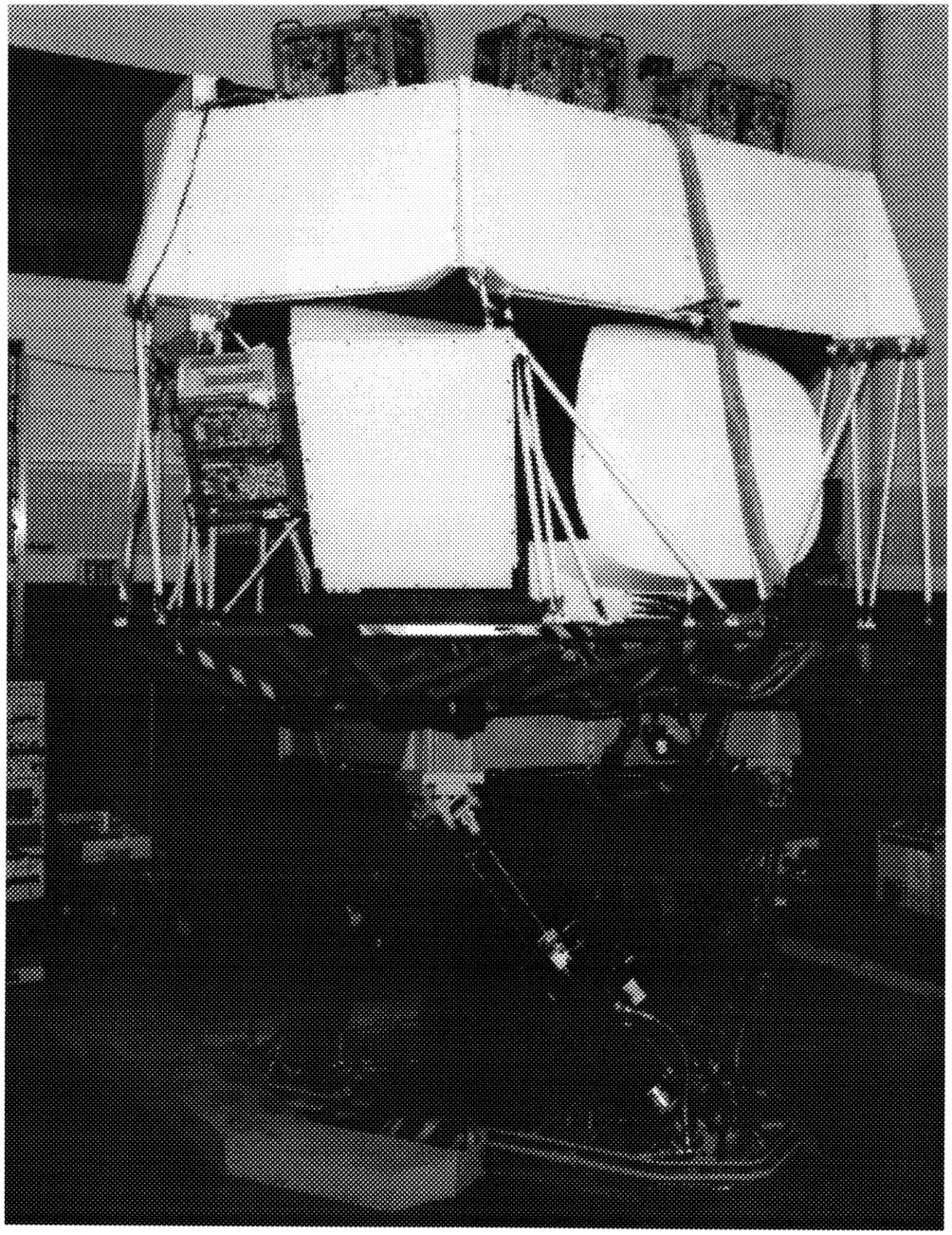

Figure 4-3: Boeing Helicopters Rotorcraft Flight Simulator

Table 4.1: Nominal Performance Specifications for the Boeing Helicopters Motion Base Flight Simulator

1. Dynamic Platform Maximum Excursions	
Pitch	+20 degrees
	−18 degrees
Roll	±19 degrees
Yaw	±23 degrees
Longitudinal	+21 inches
	−16 inches
Lateral	±18 inches
Vertical	+14 inches
	−13 inches
2. Dynamic Platform Maximum Velocities	
Pitch	±40 degrees/sec
Roll	±40 degrees/sec
Yaw	±40 degrees/sec
Longitudinal	±24 inches/sec
Lateral	±24 inches/sec
Vertical	±24 inches/sec
3. Dynamic Platform Maximum Accelerations	
Pitch	±250 degrees/sec^2
Roll	±250 degrees/sec^2
Yaw	±250 degrees/sec^2
Longitudinal	±32 feet/sec^2
Lateral	±32 feet/sec^2
Vertical	±32 feet/sec^2

Therefore, this velocity field may have recovered the statistics of the atmosphere better than a velocity field simulated using the original LFWN method. Like the LFWN method, this model was a single point approximation of the aircraft, and it did not account for the phase lag between the rotors or spatial variations during gust encounters. The cumulative probability distribution of the velocity field was kept Gaussian.

4.4.2 Full-Field Normal (Component) Turbulence Model

This model approximated the Full-Field 3-Dimensional model. The normal turbulence velocities included spatial variations across the rotor disks, while the longitudinal and lateral turbulence velocities were sampled at the aircraft center-of-gravity, like the Hub-Fixed Turbulence model. Earlier atmospheric turbulence work in the rotorcraft community used this approach, since variation of the in-plane turbulence velocities were considered to have a negligible effect [13]. The Full-Field Normal Turbulence model sampled the normal turbulence velocities at each $^3/_4$ radius blade station and used this velocity along the entire length of each blade. The vertical turbulence velocity component in the atmosphere frame was used as the normal velocity component in the blade element frame. This simplification, applicable to level flight, reduced the model's computation time by eliminating the coordinate transformations from the atmosphere frame to the blade element frames. Unlike the Hub-Fixed Turbulence model, the Full-Field Normal Turbulence model properly accounted for the phase lag between the rotors and the blades (only for the normal turbulence component). The Gaussian cumulative probability distribution of the velocity field was mapped to a more representative non-Gaussian form.

4.4.3 Full-Field 3-Dimensional Turbulence Model

This model extended the Full-Field Normal Turbulence model to include spatial variations of *each* velocity component. For the Full-Field 3-Dimensional Turbulence model, the u, v and w turbulence velocity components included spatial variations across the rotor disks, and they were individually transformed from the atmosphere frame to the blade

element frames. In the atmosphere frame, the u, v and w turbulence velocity components were treated as uncorrelated, equivalent to neglecting the atmospheric turbulence cross-spectrum, S_{uw}. The Gaussian cumulative probability distribution of the velocity field was mapped to a more representative non-Gaussian form.

Each atmospheric turbulence model test case used the same atmosphere model to compute the variations with altitude of the mean wind velocity, the turbulence intensities and the turbulence length scales. Therefore, the simulated velocity fields for each test case used the same autospectral density functions. The only differences between the cases were the method for sampling the velocity field and the velocity field's cumulative probability distribution.

4.5 Flight Simulation Task

The flight task consisted of three elements: a precision hover, a level cruise and a constant bank angle coordinated turn. This series of maneuvers, illustrated in Figure 4-4, was executed by the pilot for each test case of the flight simulation experiment. The first element of the flight task required the pilot to maintain a precision hover at an altitude of 15 feet. The desired performance level was a position error of less than 5 feet in all directions, while the acceptable performance level was a position error of less than 10 feet in all directions. To aid the pilot during this station-keeping activity, the aircraft was positioned above a helipad between a pair of visual cue reference poles. These poles stood 10 feet tall, were spaced 50 feet apart and were marked with height in units of feet. The aircraft heading was West, and the mean wind direction was North. This arrangement was chosen so the mean wind velocity vector convected the turbulence field laterally across the rotor disks, and any problems associated with a stationary turbulence field were avoided.[3] The precision hover task was sustained for a duration of three minutes. During

[3] This phenomena results when the aircraft has little airspeed. The simulated turbulence velocity field will become almost stationary relative to the aircraft, and the simulated turbulence velocities sampled by the rotor

this time, the aircraft's velocities and accelerations, the position errors and the pilot's control inputs were recorded for later analysis.

The second element of the flight task required the pilot to hold the aircraft in level cruise at an altitude of 1500 feet. While holding an airspeed of 100 knots, the pilot was instructed to minimize all attitude excursions, i.e., pitch, roll and yaw. The desired performance level was attitude excursions less than 5 degrees and altitude excursions less than 50 feet, while the acceptable performance level was attitude excursions less than 10 degrees and altitude excursions less than 100 feet. The level cruise task was sustained for a duration of three minutes. During this time, the aircraft's velocities and accelerations, the attitude excursions and the pilot's control inputs were recorded for later analysis.

The third element of the flight task was a constant bank angle, coordinated turn, which required the pilot to hold a steady bank angle of 30° while performing a coordinated turn to his left. The pilot was instructed to maintain an altitude of 1500 feet and an airspeed of 100 knots throughout the entire maneuver. Again, the desired performance level was attitude excursions less than 5 degrees and altitude excursions less than 50 feet, while the acceptable performance level was attitude excursions less than 10 degrees and altitude excursions less than 100 feet. After a heading change of 720° (two revolutions), the pilot leveled the aircraft and the flight task was complete. The coordinated turn task lasted approximately two minutes. During this time, the aircraft's velocities and accelerations, the attitude excursions and the pilot's control inputs were recorded for later analysis.

4.6 Flight Simulation Procedure

The pilots participating in the flight simulation experiment had different levels of experience with aircraft simulators. Therefore, to accustom each pilot to Boeing Helicopters' flight simulator and its ride characteristics, the flight simulation experiment

---

blades become essentially constant. Under these conditions, the frozen field assumption is not valid. The turbulence model developed in this thesis is not meant to be used for investigation under flight conditions such as this.

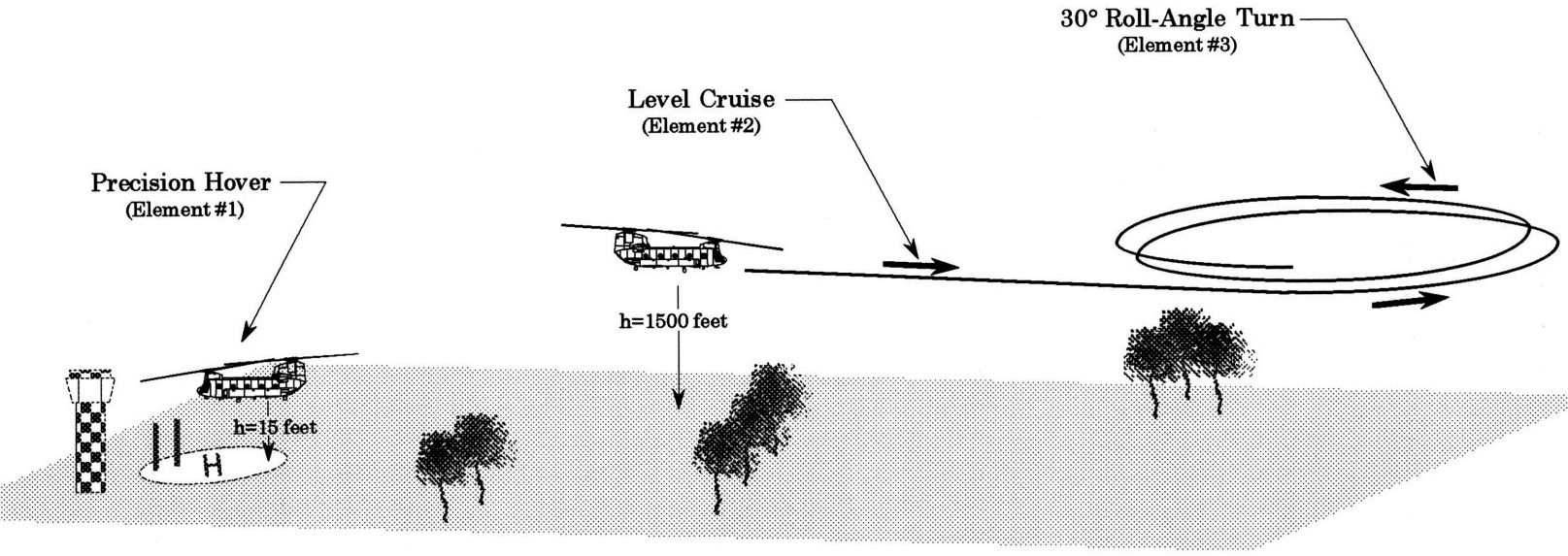

Figure 4-4: Flight Tasks Executed for the Atmospheric Turbulence Model Evaluation

began with a five minute pre-simulation flight. During this time, the pilot flew the simulator in calm air, following no specific flight plan. The pilot was questioned about any differences between the real aircraft and the simulated aircraft which would effect his ability to evaluate the atmospheric turbulence models. These included differences in aircraft response characteristics or differences in the physical layout of the cockpit and flight controls. After this warm-up time, the four test cases of the flight simulation experiment were performed.

During each flight, the pilots completed the flight task for the three different turbulent air models. The three atmospheric turbulence model test cases were presented to the pilot in a random order. The only information about the model given to the pilot was that the intended level of the simulated turbulence was moderate, and the mean wind velocity was thirty knots from the North. It was decided that having the pilot evaluate the turbulence models blindly would yield the most consistent results by limiting the level of outside influence.

During each run, the pilots were encouraged to offer comments about the quality, i.e., the realism, of the simulated turbulence. After completion of the flight task, the pilot was prompted for additional remarks about the turbulence simulation by means of a survey. The simulation survey, given in Appendix D, included questions which asked the pilot to estimate the turbulence intensity and overall realism and the Cooper-Harper rating for the aircraft/turbulence/task combination. Other questions investigated the reasons for possible pilot dissatisfaction with the realism of the simulated turbulence. These questions consisted of pilot ratings of (1) the relative amplitudes of excursions in the six degrees-of-freedom: surge, sway, heave, pitch, roll and yaw, (2) the patchiness of the turbulence, (3) the frequency content of the turbulence, and (4) the occurrence of sudden large amplitude gusts.

The simulation survey represented a source of subjective data used to measure qualitative changes in the realism of the turbulence simulation as perceived by the pilot.

In addition to this survey, a set of flight parameters were output onto strip charts for real-time visual inspection and recorded on magnetic tape for later analysis. The flight parameter set was the source of numerical data used to measure quantitative changes in the realism of the simulated turbulence.

4.7 Pilot Experience

Three pilots from Boeing Helicopters' flight test program participated in the atmospheric turbulence simulation experiment. Their previous flight experiences are summarized below:

Table 4.2: Flight Experience of the Pilot's Participating in the Atmospheric Turbulence Evaluation

	Total No. of Hours	Hours in CH-46/47	Hours in Simulators
Pilot A	6,500	155	75
Pilot B	8,900	480	450
Pilot C	11,000+	7,000+	600+

It should be noted that Pilot C has participated in other projects aimed at improving the realism of atmospheric turbulence simulations. Most recently, Pilot C participated in a project investigating the fidelity of the British International Helicopters' (BIH) Chinook Simulator. During this time, Pilot C evaluated the atmospheric turbulence model available in the BIH helicopter simulator.

Chapter 5

Results and Discussion

This chapter discusses the results obtained from the full-field atmospheric turbulence model implemented into Boeing Helicopters' tandem helicopter flight simulator. The discussion begins with a description of the results used to determine the best discretization method and the adequate number of harmonics for the von Kármán autospectral densities. Results verifying the increase in computational efficiency obtained with this method are shown. Comparisons of the traditional Hub-Fixed model and the new Full-Field models through non-real-time simulation comprise the bulk of the remaining results. General trends seen in the simulated aircraft data measured during the flight simulation experiment, particularly the amplitude and frequency of control inputs, are then analyzed in connection with these non-real-time results. Finally, the pilot comments given during the flight simulation experiment are highlighted and explanations of their meaning are offered where possible.

5.1 Validation of the Full-Field Model

5.1.1 Discretization Methods

Three basic frequency grids for discretization of the von Kármán autospectral densities–constant linear spacing, constant logarithmic spacing and exact integration–were considered relevant for further investigation. Vertical gust time samples were generated

from these frequency grids. These frequency grids are described in the next three sections and typical examples are illustrated pictorially in Figures 5-1a, 5-1b and 3-5, respectively.

5.1.1.1 Constant Linear Spacing

This method used a Cartesian grid consisting of N linearly spaced points along each axis of two-dimensional frequency space. (See Figure 5-1a) Recent rotorcraft atmospheric turbulence models have used this discretization method for non-real-time flight simulation [20, 23]. (See Equations 3.2.2 and 3.2.3) Unfortunately, constant linear spacing is unsuitable for real-time atmospheric turbulence computation with the processing power of the computer hardware currently available for flight simulation. (See Section 3.2.1) It will be shown that for the simulated atmospheric turbulence not to possess uncharacteristic spectral peaks at frequencies corresponding to individual harmonics in the summation, the frequency grid should have at least fifty frequency points per decade along each axis. Unfortunately, real-time execution requires the total number of harmonics in the summation to be less than approximately 1000. For constant linear spacing of a two-dimensional autospectral density, this requirement constrains the frequency grid to only 33 points along each axis, (i.e. $33 \times 33 \approx 1000$). Recall that the discretized von Kármán autospectral densities span more than three decades to recover 98% of the turbulence energy. Therefore, the spectral requirement and real time execution cannot be satisfied. For 50 points along each axis in the lowest decade of the frequency grid, the total number of harmonics needed for constant linear spacing would be

$$total\ \ harmonics = \left[\sum_{j=1}^{\substack{no.\ of \\ decades}} \left(no.\ points\ per\ decade \right) \cdot 10^{j-1} \right]^{\substack{no.\ of \\ dimensions}}, \qquad (5.1.1)$$

or more than 30 million total harmonics for the two-dimensional von Kármán autospectral density. Consequently, constant linear spacing was deemed too computationally intensive for real-time execution, and it was not further investigated.

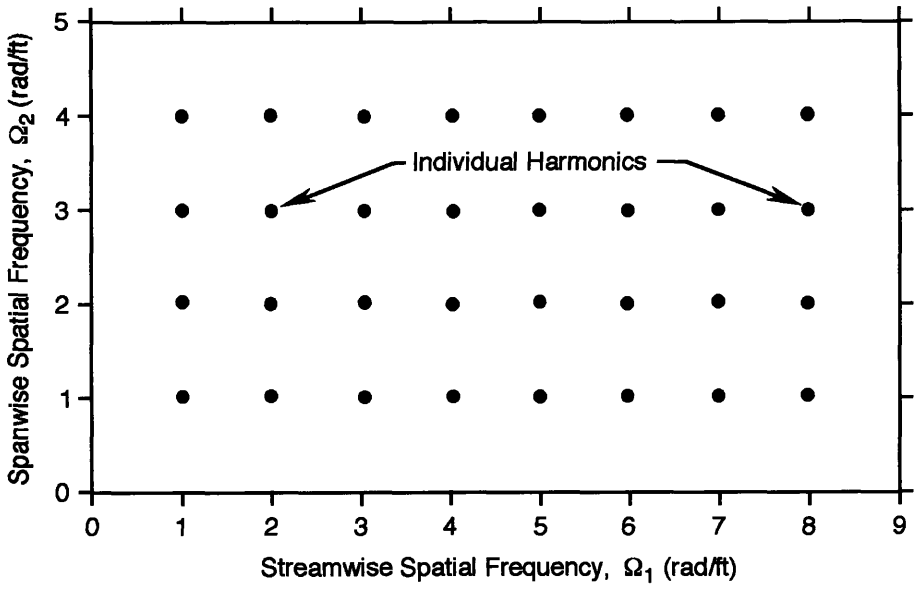

Figure 5-1a: Pictorial Frequency Grid for Constant Linear Spacing

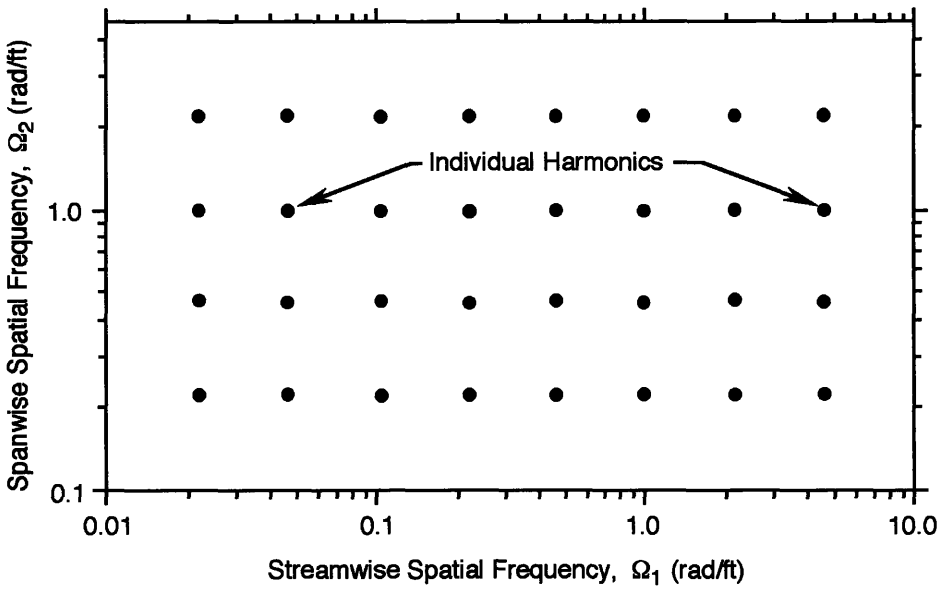

Figure 5-1b: Pictorial Frequency Grid for Constant Logarithmic Spacing

5.1.1.2 Constant Logarithmic Spacing

This method used a Cartesian grid consisting of N logarithmically spaced points along each axis of two-dimensional frequency space. (See Figure 5-1b) Constant logarithmic spacing allows a better discretization of processes which span several decades, since the frequency increment is not constant. The computational kernel of the full-field atmospheric turbulence model was transferred to MATLAB. Here, it generated the vertical gust time samples for a rotor hub of a helicopter flying trimmed and level. The frequency ranges of the logarithmic grid were adjusted so the gust time samples showed spectral content throughout the temporal frequency range of interest, 0.01 rad/sec $\leq \omega \leq$ 20.00 rad/sec. The turbulence intensity, turbulence length scale and true airspeed were chosen to be representative of the low altitude, low airspeed flight condition flown during Task I of the flight simulation experiment. The values of these turbulence parameters were σ_w=5.0 feet/sec, L_w=400 feet and V_{TAS}=20 knots. The sampling rate and the overall time history length were chosen to satisfy the Nyquist Sampling Theorem and to yield an accurate discrete Fourier transform in the temporal frequency range of interest. The values of these simulation parameters were Δt=20 milliseconds and T=200 seconds.

5.1.1.3 Exact Integration

This method used a frequency grid determined by the exact integration of the two-dimensional von Kármán autospectral density, S_{ww}. The harmonics were chosen so that each contributed an equal fraction of energy to the total turbulent energy. (See Figure 3-5) The aircraft's trajectory through the atmospheric turbulence field and its attitudes along that trajectory were trimmed and level, so that these vertical gust time samples would be comparable to those generated with the constant logarithmic spacing in MATLAB. The chosen frequency ranges for the exact integration were discussed in Section 3.2.4. The turbulence parameters were the same as for the constant logarithmic spacing: σ_w=5.0 feet/sec, L_w=400 feet and V_{TAS}=20 knots. The simulation parameters were also the same as for the constant logarithmic spacing: Δt=20 milliseconds and T=200 seconds.

5.1.2 Processing of the Simulated Gust Time Samples

Comparison of the different frequency grid types was made to determine (1) whether the summation of sinusoids algorithm had sufficient spectral fidelity compared to the linearly filtered white noise algorithm, and (2) whether the additional computational requirements of either constant logarithmic spacing or exact integration were justified by an improvement in the spectral fidelity of the summation of sinusoids algorithm.

5.1.2.1 Amplitude Scaling

Each gust time sample was first scaled to have a mean amplitude equal to zero and a root mean square (rms) amplitude equal to the intended turbulence intensity (in this case, 5.00 feet/sec). This ensured that only the spectral content would vary between the time samples, and this variation would be related to the number of harmonics and choice of frequency grid type.

5.1.2.2 Data Windowing

A Hanning window was applied to each scaled gust time sample in preparation for the discrete Fourier transform. The Hanning window is a unity amplitude sine wave with a period equal to twice the time sample's length. The major influence of a data window is to damp out the effects of the Gibb's phenomena resulting from a truncation of the infinite time sample into a T-second sample. Recall that the time sample must be normalized by the rms amplitude of the data window. For the Hanning window, the rms amplitude is equal to $\frac{\sqrt{2}}{4} \approx 0.35355$.

5.1.2.3 Discrete Fourier Transform

The autospectral density function $S_{ww}(\omega)$, of a stationary process, $w(t)$, is related to its discrete Fourier transform by

$$S_{ww}(\omega) = E\left[\frac{\Delta t}{T}\left|\mathfrak{F}\{w(t)\}\right|^2\right] \text{ for } \frac{T}{\Delta t} \rightarrow large \ , \qquad (5.1.2)$$

where $|\mathfrak{F}\{w(t)\}|$ is the magnitude of the discrete Fourier transform of $w(t)$. The quantity inside the brackets is known formally as the *periodogram* of $w(t)$. The periodogram of a stationary process is an asymptotically unbiased estimate of the autospectral density. Therefore, as the number of periodograms becomes large, the expected value of the periodogram approaches the autospectral density. It is reasonable to assume, however, that during each flight simulation session, pilots are exposed to only a few, relatively brief time samples of simulated atmospheric turbulence. Therefore, realistic flight simulation requires the spectral content of the simulated atmospheric turbulence not vary widely between the time samples. The periodogram of each time sample should be independently comparable to the intended autospectral density. Thus, an adequate number of harmonics must be used in the summation so that the periodogram converges *rapidly* to the autospectral density. For this research, the average of three periodograms was defined as the approximate autospectral density produced by the atmospheric turbulence model.

5.1.3 Comparison of the Different Discretization Methods

Two necessary criteria were specified for the time samples of the atmospheric turbulence models. These criteria determined whether the time samples generated by the atmospheric turbulence model had enough spectral fidelity with the von Kármán model.

5.1.3.1 High Frequency Asymptotic Behavior

The overall shape of the approximate autospectral density must closely resemble the von Kármán autospectral density. Large uncharacteristic peaks or gaps in the approximate autospectral density, associated with too few harmonics in the summation or a poorly chosen distribution of harmonics, are unacceptable. Also, the von Kármán autospectral densities decrease asymptotically according to the $-5/3$ power of spatial frequency for high frequencies. Therefore, behavior not following the $-5/3$ power of spatial frequency is also unacceptable.

5.1.3.2 Spectral Coherence Function

Inevitably, the approximate autospectral density will be noisy and have deviations above and below the von Kármán autospectral density. Therefore, the second criteria requires that the envelope containing these deviations not be too large. A spectral coherence function was defined to measure the level of relative spectral fidelity between the approximate autospectral density and the von Kármán autospectral density over the frequency range of interest. The spectral coherence function is

$$J = \log_{10}\left[S_{vk}(\omega)\right] - \log_{10}\left[S_{ww}(\omega)\right], \tag{5.1.3}$$

where $S_{vk}(\omega)$ is the von Kármán autospectral density and $S_{ww}(\omega)$ is the approximate autospectral density. The spectral coherence function for a vertical gust time sample generated by linearly filtered white noise was used as the benchmark for adequate spectral fidelity. This simulation technique is the traditional stochastic method of real-time atmospheric turbulence simulation. Therefore, any new model claiming to be an improvement needed to demonstrate this level of spectral fidelity.

5.1.3.3 Baseline Results for Linearly Filtered White Noise

Figure 5-2a shows the approximate autospectral density computed from a single 285-second time sample of atmospheric turbulence generated from linearly filtered white noise. The approximate autospectral density clearly exhibits asymptotic behavior. However, the asymptote is the –2 power of spatial frequency, rather than the $^{-5}/_{3}$ power. This is the inescapable deficiency of linearly filtered white noise. Rational shaping filters cannot reproduce the von Kármán model's $^{-5}/_{3}$ asymptote, so it is approximated by the Dryden model's –2 asymptote. The solid line in Figure 5-2a is the Dryden autospectral density. Figure 5-2b shows the spectral coherence function for this time sample. Notice, nearly all of the discrete frequency components of the approximate autospectral density are within a one decade-wide envelope for frequencies below 1 Hertz, and within a two decade wide

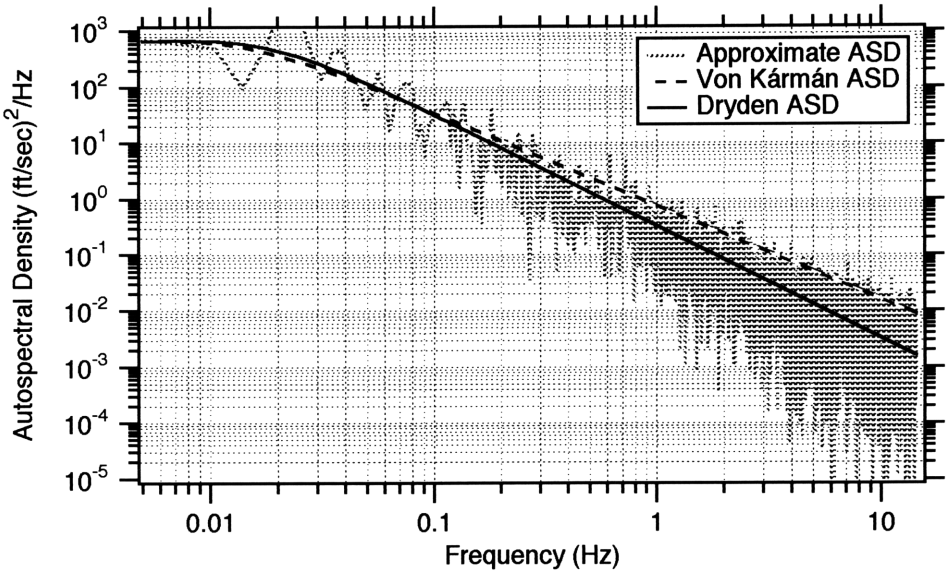

Figure 5-2a: Autospectral Density of a Vertical Gust Time Sample Generated from Linearly Filtered White Noise

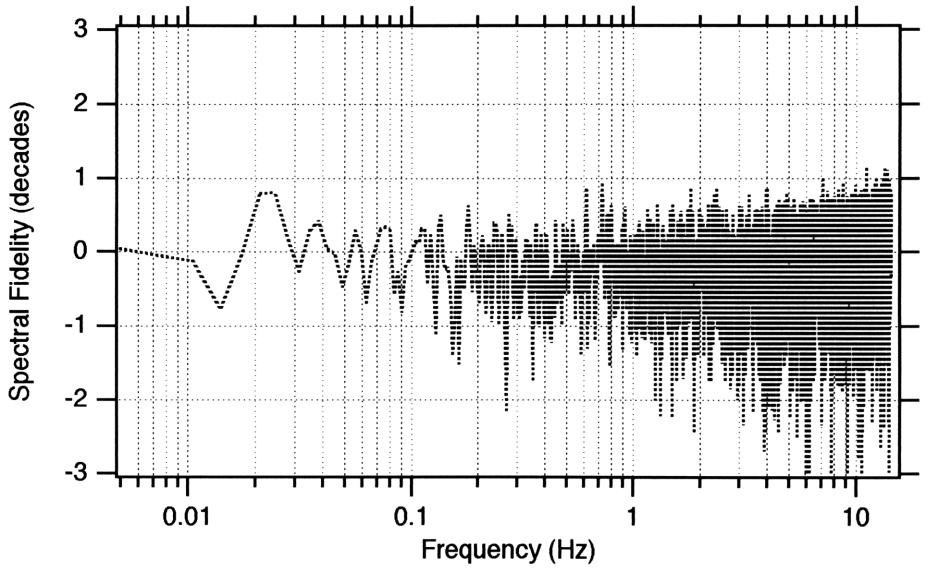

Figure 5-2b: Spectral Fidelity of a Vertical Gust Time Sample Generated from Linearly Filtered White Noise

envelope for frequencies above 1 Hertz. This spectral envelope was defined as the minimal performance needed.

5.1.4 Results for the Summation of Sinusoids

Figure 5-3, Figure 5-4, Figure 5-5 and Figure 5-6 show the approximate autospectral densities and spectral fidelity functions for constant logarithmic spacing of 225, 2500, 10000 and 40000 harmonics, respectively. Figure 5-7 and Figure 5-8 show the approximate autospectral densities and spectral fidelity functions for exact integration of 225 and 2500 harmonics, respectively.

5.1.4.1 Results for Constant Logarithmic Spacing

Figure 5-3a shows the autospectral density for 225 harmonics and constant logarithmic spacing. This model[1] is not an adequate approximation. The autospectral density does not exhibit asymptotic behavior. Instead, it has large peaks that do not resemble the smooth von Kármán autospectral density. Inspection of these peaks shows that their frequencies correspond to the frequencies of the individual harmonics. The spectral coherence function (see Figure 5-3b) exceeds the maximum allowable value for frequencies greater than ~0.04 Hertz. Therefore, these results do not satisfy the required criteria.

Figure 5-4a shows the autospectral density for 2500 harmonics and constant logarithmic spacing. There is a noticeable improvement, but this model is still not an adequate approximation. The autospectral density continues to have large peaks corresponding to the individual harmonics, but the spectral fidelity at lower frequencies is improved. Now, the frequency range of acceptable spectral coherence values (see Figure 5-4b) extends to frequencies of ~0.1 Hertz. Again, these results still do not satisfy the required criteria.

---

[1] Throughout the remainder of section 5.1, the phrase "model" will refer to the combination of the number of harmonics and the choice of frequency grid type.

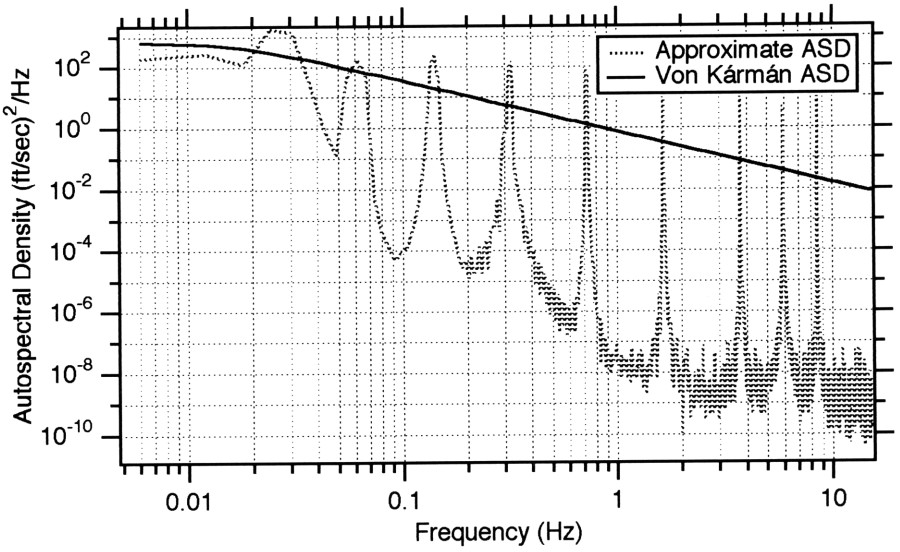

Figure 5-3a: Autospectral Density of a Vertical Gust Time Sample Generated from the Summation of 225 Harmonics and Constant Logarithmic Spacing

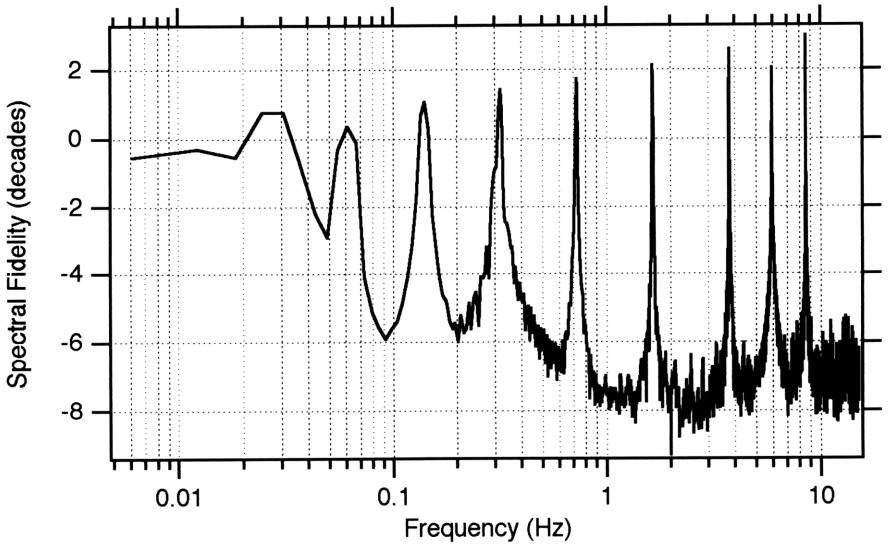

Figure 5-3b: Spectral Fidelity of a Vertical Gust Time Sample Generated from the Summation of 225 Harmonics and Constant Logarithmic Spacing

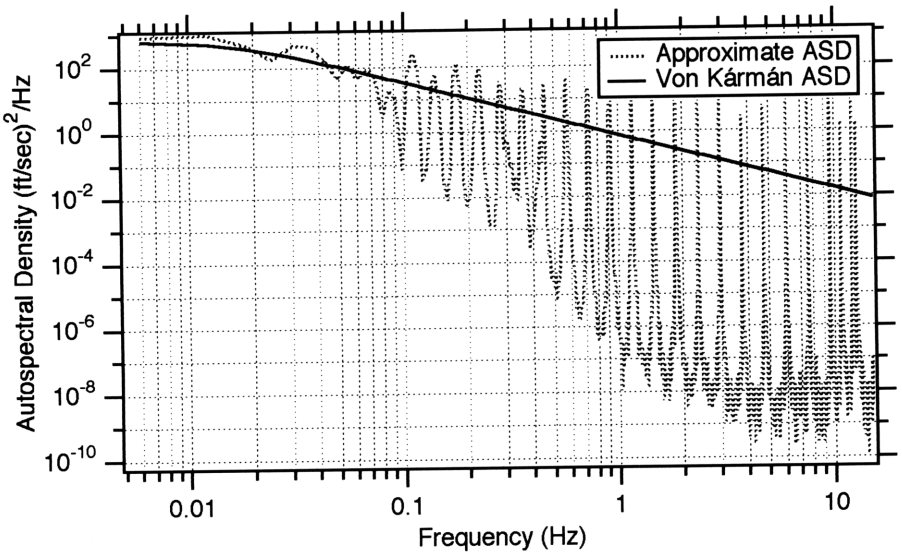

Figure 5-4a: Autospectral Density of a Vertical Gust Time Sample Generated from the Summation of 2500 Harmonics and Constant Logarithmic Spacing

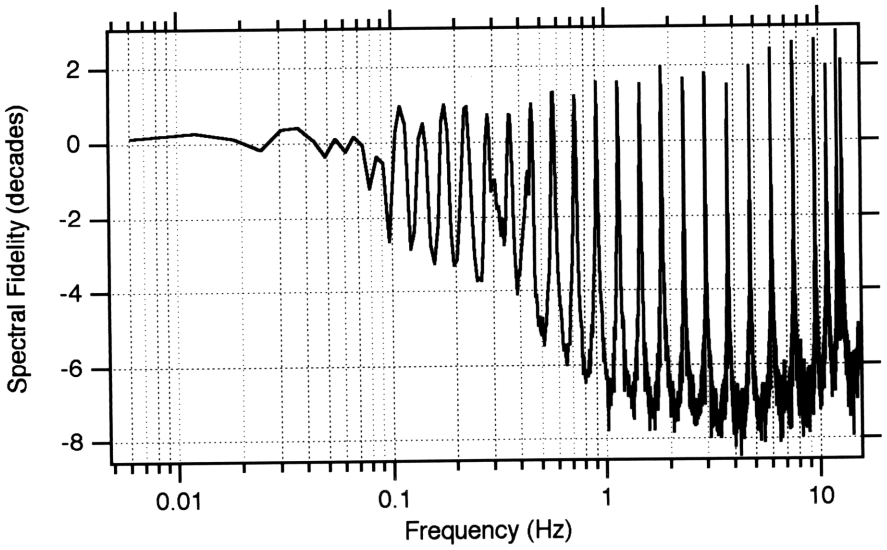

Figure 5-4b: Spectral Fidelity of a Vertical Gust Time Sample Generated from the Summation of 2500 Harmonics and Constant Logarithmic Spacing

The addition of still more harmonics to the summation continues to yield improving results, but at the expense of exceeding the maximum computation time limit. Figure 5-5a and Figure 5-6a show the autospectral densities for 10000 and 40000 harmonics, respectively. This number of harmonics in the summation is not possible during real-time simulation. Alone, this is sufficient reason for this model to be considered inadequate. However, the spectral coherence function continues to not satisfy the required criterion. Figure 5-5b shows that the range of acceptable spectral coherence values for 10000 harmonics only extends to frequencies of ~0.2 Hertz. Figure 5-6b shows that the frequency range of acceptable spectral coherence values for 40000 harmonics only extends to frequencies of ~0.5 Hertz.

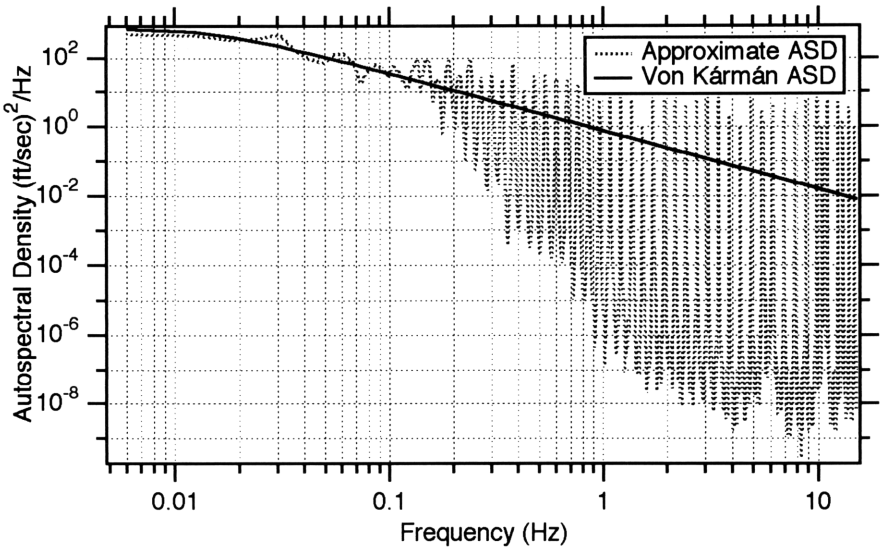

Figure 5-5a: Autospectral Density of a Vertical Gust Time Sample Generated from the Summation of 10000 Harmonics and Constant Logarithmic Spacing

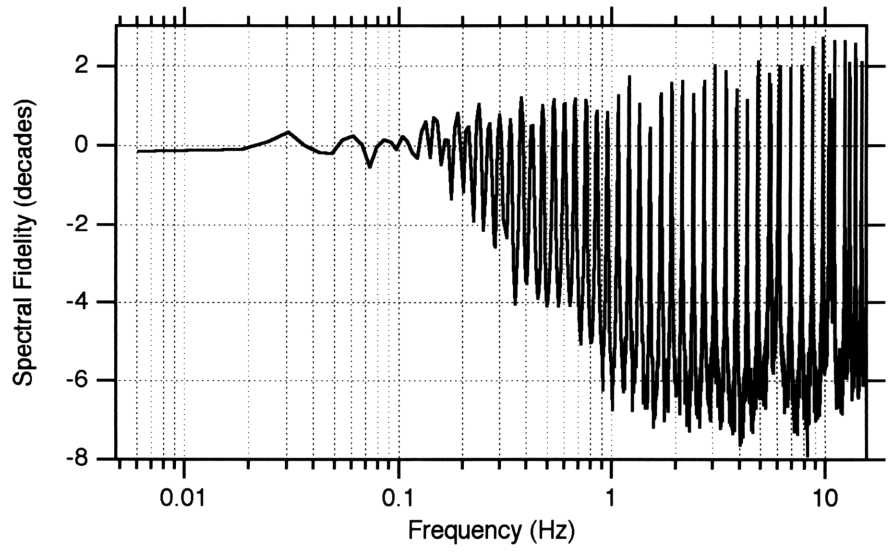

Figure 5-5b: Spectral Fidelity of a Vertical Gust Time Sample Generated from the Summation of 10000 Harmonics and Constant Logarithmic Spacing

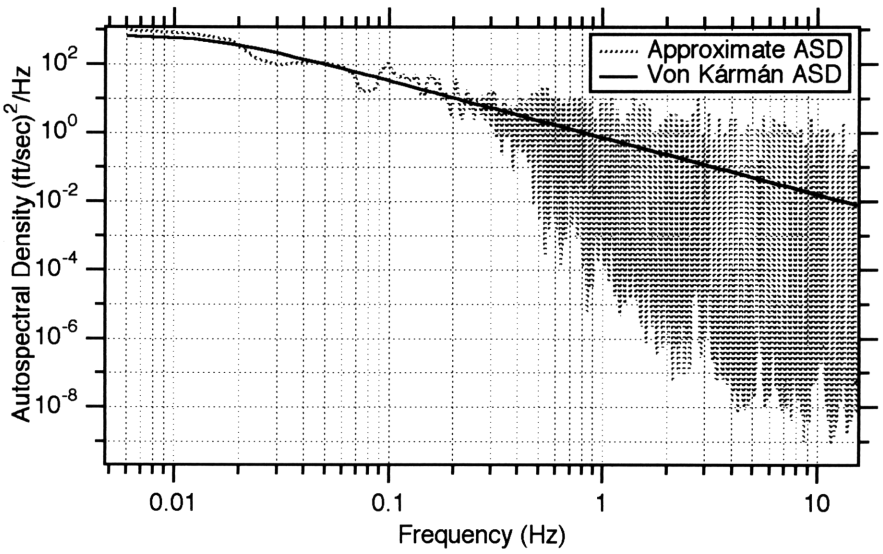

Figure 5-6a: Autospectral Density of a Vertical Gust Time Sample Generated from the Summation of 40000 Harmonics and Constant Logarithmic Spacing

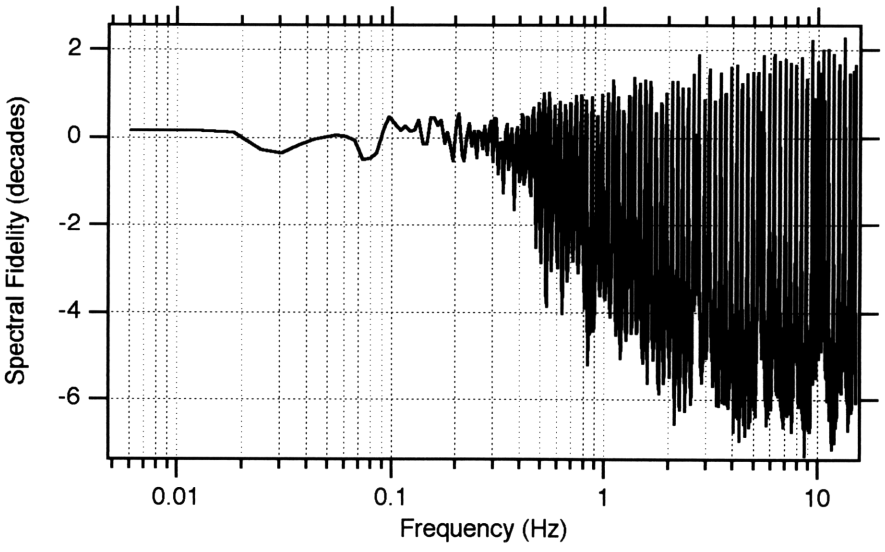

Figure 5-6b: Spectral Fidelity of a Vertical Gust Time Sample Generated from the Summation of 40000 Harmonics and Constant Logarithmic Spacing

5.1.4.2 Results for Exact Integration

Figures 5-7a shows the autospectral density for 225 harmonics and exact integration. Unlike the models using constant logarithmic spacing, this model adequately satisfies the required criteria. The autospectral density has the correct asymptote, and there are no uncharacteristic peaks. The spectral coherence function shows that the autospectral density is within the one decade wide envelope for frequencies below 1 Hertz and within the two decade wide envelope for frequencies above 1 Hertz.

Notice that over the frequency range of ~7.8 to ~11.1 Hertz, the spectral coherence function falls to an unsatisfactory level. This gap exists because very few harmonics cover this frequency region in the discretized autospectral density. Although not ideal performance, this was considered acceptable, because this frequency band contributes less than 1% of the total turbulent energy. Exact integration scales the location of this gap with turbulence length scale and true airspeed, so it remains in the same relative location of von Kármán autospectral density. As a result, the gap will always contribute less than 1% of the total energy, regardless of atmospheric condition.

Figures 5-8a shows the autospectral density for 2500 harmonics and exact integration. Given enough computation time, this model would have been used. The autospectral density has the correct asymptote, and the spectral coherence function (see Figure 5-8b) is well within the one decade wide envelope for *all* frequencies less than 15 Hertz.

5.1.4.3 Frequency Grid for Real-Time Simulation

Both models using exact integration satisfy the spectral criteria outlined in Section 5.1.3. However, the ultimate criterion that must be satisfied for real-time atmospheric turbulence simulation is the computation time limit. Only the model with 225 harmonics adequately satisfies the spectral criteria and does not require more computation time than possible for real-time execution. Therefore, all subsequent non-real-time and real-time evaluations of the full-field atmospheric turbulence model use 225 harmonics in

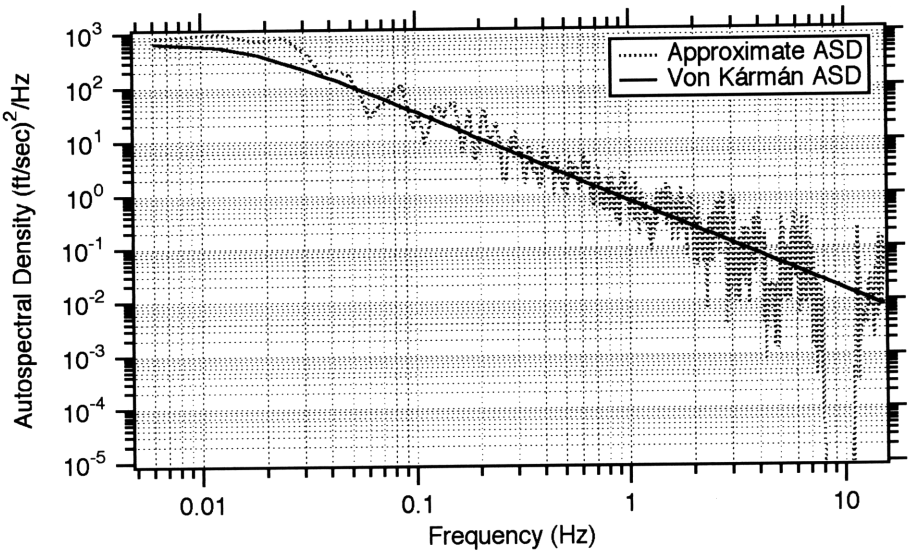

Figure 5-7a Autospectral Density of a Vertical Gust Time Sample Generated from the Summation 225 Harmonics and Exact Integration

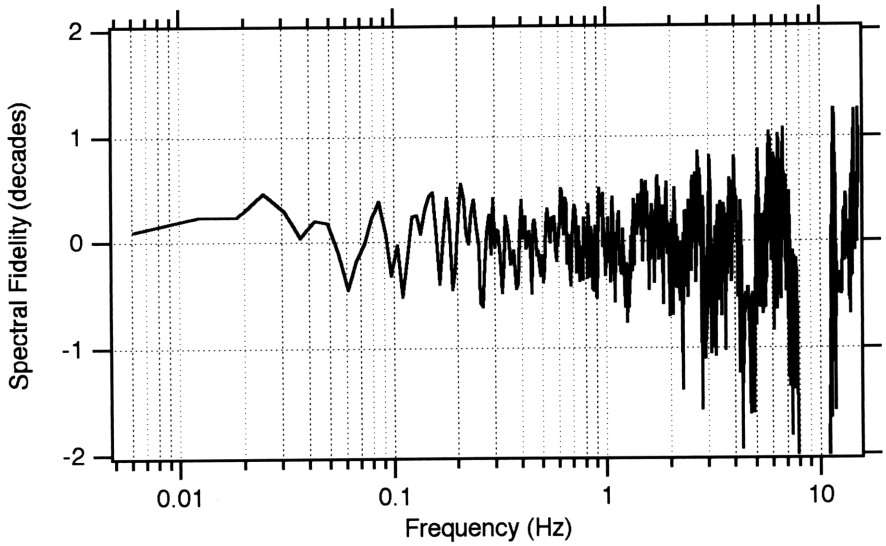

Figure 5-7b: Spectral Fidelity of a Vertical Gust Time Sample Generated from the Summation of 225 Harmonics and Exact Integration

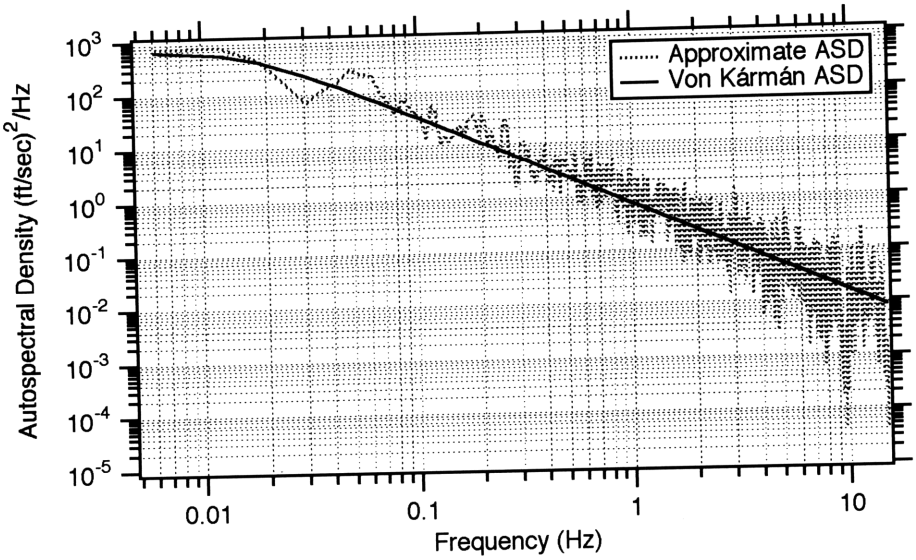

Figure 5-8a: Autospectral Density of a Vertical Gust Time Sample Generated from the Summation of 2500 Harmonics and Exact Integration

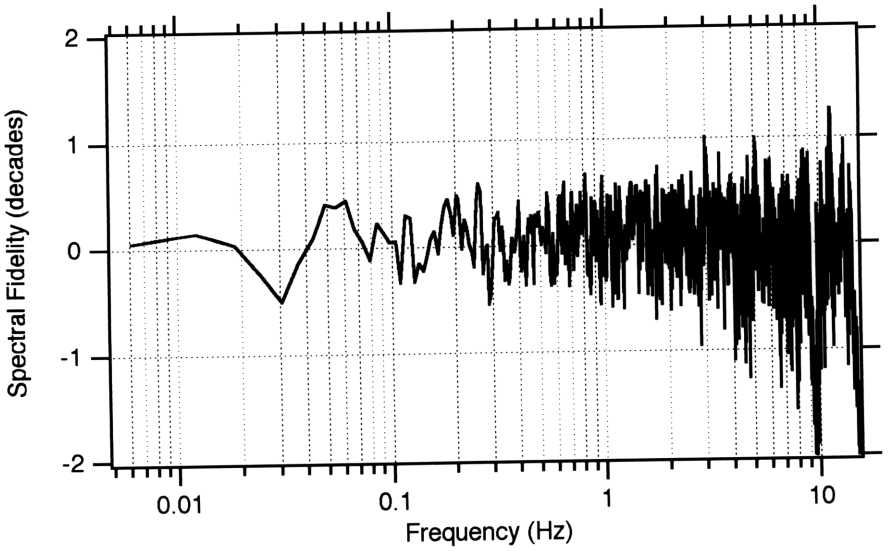

Figure 5-8b: Spectral Fidelity of a Vertical Gust Time Sample Generated from the Summation of 2500 Harmonics and Exact Integration

the summation with the frequency grid chosen by exact integration of the von Kármán autospectral densities.

5.2 Non-Real-Time Evaluation

Prior to the flight simulation experiment, a non-real-time evaluation of the Full-Field atmospheric turbulence model was performed. The purpose of this preliminary analysis was to determine the changes in aircraft rigid body accelerations caused by using the Full-Field models rather than the Hub-Fixed model. Then, it could be decided if the changes in predicted aircraft accelerations represented differences which should be discernible by the pilots flying the flight simulator.

5.2.1 Flight Condition

For a proper comparison of the atmospheric turbulence models, it was desired to have the aircraft follow the same flight path through the same atmospheric turbulence field during each trial. Thus, the aircraft's rigid body state variables (u, v, w, θ, ϕ and ψ) and state variable derivatives ($\dot{u}$, $\dot{v}$, $\dot{w}$, $\dot{\phi}$, $\dot{\theta}$ and $\dot{\psi}$) had to be nulled to their trim values at the completion of every time step. This allowed the incremental forces and moments due to atmospheric turbulence to be computed while keeping the aircraft isolated from the otherwise induced rigid body rates and accelerations. In addition, the simulated atmospheric turbulence would often overpower the CH-47D's stability augmentation system and cause the aircraft's flight path to diverge when the state variables were not fixed at their trim values. The flight path was trimmed level flight, in the direction parallel to the mean wind velocity vector.

During the non-real-time evaluation, two flight parameters–the aircraft's true airspeed and the turbulence length scale–were varied independently for the Hub-Fixed and Full-Field models. First, the airspeed was varied from 20 knots to 100 knots for length scales of 60 feet, 200 feet and 1000 feet. Second, the length scale was varied from 60 feet to 1000

feet for airspeeds of 20 knots, 60 knots and 100 knots. Multiple trials (varying between three and eight) were executed for each combination of airspeed, length scale and atmospheric turbulence model. The atmospheric turbulence models were the same models described in Section 4.4.: the Hub-Fixed model, the Full-Field Normal model and the Full-Field 3-Dimensional model. The computations were executed with the same flight simulator set-up described in Section 4.2, except the calculations were non-real-time and without a pilot. Like the flight simulation experiment, the blade element rotor model was sub-iterated 5:1 with the aircraft and control system models. The overall time step was 50 milliseconds and each simulation lasted 500 seconds.

5.2.2 Effect of Restricted Rigid Body Motion

The restriction of aircraft rigid body motions to the predefined level flight path removed from the full equations of motion those terms which depended on the rigid body dynamic states. Most of these terms would act to stabilize the aircraft, so removing them should magnify the effects of the atmospheric turbulence. However, under certain conditions, it is conceivable that this constraint may attenuate the effects of the atmospheric turbulence. Therefore, these non-real-time results are only intended to quantify the *relative* differences in rigid body accelerations due to full-field sampling, as it pertains to piloted flight simulation. It is assumed that this attenuation is uniform between atmospheric turbulence models for small disturbances, and comparison of the results for this isolated aircraft configuration will be a valid approximation to the results for the full aircraft.

5.2.3 Processing of the Non-Real-Time Aircraft Data

5.2.3.1 Root Mean Square Accelerations

The root mean square (rms) rigid body forces and moments were calculated for each 500-second time sample. The rms linear accelerations ($\dot{u}$, $\dot{v}$, $\dot{w}$) and rotational

accelerations ($\dot{\phi}$, $\dot{\theta}$, $\dot{\psi}$) were found by scaling the rms forces by the aircraft's mass and the rms moments by the aircraft's moments of inertia.

5.2.3.2 Normalized Root Mean Square Accelerations

Scaling the rms accelerations for the Full-Field Normal and Full-Field 3-Dimensional models by the average rms accelerations for the Hub-Fixed model yields the proportional increase or decrease of that model with respect to the Hub-Fixed model. In Figures 5-9 through 5-20, the average normalized accelerations are indicated by the curves, and the 95% confidence intervals of these curves are indicated by the $\mathbf{I}$ symbols.

5.2.3.3 Confidence Intervals for the Estimated Means

The rms accelerations were assumed to have normal distributions. For n samples of a normal distribution, the 95% confidence intervals of the estimated mean are described by a t distribution with $(n\text{-}1)$ degrees of freedom. Thus, the true mean, M, can be predicted with 95% confidence to lie in the interval

$$\overline{M} - t_{0.975,n-1}\frac{\overline{\sigma}}{\sqrt{n}} \le M \le \overline{M} + t_{0.975,n-1}\frac{\overline{\sigma}}{\sqrt{n}} , \qquad (5.2.1)$$

where $\overline{M}$ is the estimated mean and $\overline{\sigma}$ is the estimated standard deviation. $t_{0.975,n-1}$ is the 97.5 percentile value for the t distribution with $(n\text{-}1)$ degrees of freedom. Table 5.1 defines these values.

Table 5.1: t Distribution Confidence Intervals, $t_{0.975,n-1}$ vs. Number of Samples, n

$(n\text{-}1)$	1	2	3	4	5	6	7	8	9	10
$t_{0.975,n-1}$	12.71	4.30	3.18	2.78	2.57	2.45	2.36	2.31	2.26	2.23
$\frac{t_{0.975,n-1}}{\sqrt{n}}$	12.71	3.04	1.84	1.39	1.15	1.00	0.89	0.82	0.75	0.71

5.2.4 Results of Non-Real-Time Simulation

5.2.4.1 Human Thresholds for the Detection of Acceleration

The *just noticeable difference* (JND) of a sensory stimulus is defined as that stimulus increment for which the difference between the steady value and the steady value-plus-increment may be distinguished by human subjects. The Weber-Fechner Law states that the just noticeable difference in a sensory stimulus is proportional to the stimulus level [38]. This relationship is given by

$$\frac{\Delta I}{I} \cong K \,. \tag{5.2.2}$$

ΔI is the just noticeable difference in the stimulus, I is the steady stimulus level and K is an empirically-derived constant. In laboratory experiments, K was found to be of order equal to –20 decibels, or 10% [39]. This really is a minimum bound for the sensory threshold, since unlike flight simulation, these experiments were single axis tasks with few external distractions and complete subject dedication to magnitude estimation. It is not the purpose of this research to explore the detailed physiological effects of motion simulation. Rather, the given thresholds are intended to indicate typical human performance found by earlier experiments. Considering these thresholds, it can be decided whether or not the differences in aircraft response for the Hub-Fixed model and the Full-Field models represent changes which are great enough to be reliably perceived by the pilots in the flight simulator. For this research, the just noticeable difference in stimulus will be defined to be twice this minimum threshold, 20%, to account for the additional distractions and infidelities of the flight simulator.

5.2.4.2 Effect of Airspeed Variations

Longitudinal Acceleration Figure 5-9 shows the normalized longitudinal accelerations for airspeed variations. At small length scales (see Figure 5-9a), the Full-Field 3-Dimensional model predicts 35-45% less longitudinal acceleration, and the Full-Field Normal model predicts 25-35% less longitudinal acceleration. Therefore, the pilot should be able to

distinguish between the Hub-Fixed model and both Full-Field models, but probably not between the Full-Field models themselves. At large length scales (see Figure 5-9c), the Full-Field 3-Dimensional model predicts only 10-20% less longitudinal acceleration, and the Full-Field Normal model predicts no noticeable difference in longitudinal acceleration. Therefore, it is unlikely that the pilot will be able to distinguish between the models.

Lateral Acceleration Figure 5-10 shows the normalized lateral accelerations for airspeed variations. At small length scales (see Figure 5-10a), the Full-Field 3-Dimension model predicts only 10-20% less lateral acceleration, and the Full-Field Normal model predicts no noticeable difference in lateral acceleration. At large length scales (see Figure 5-10c), there is no noticeable difference between any of the models. Therefore, it is unlikely that the pilot will be able to distinguish between the models.

Vertical Acceleration Figure 5-11 shows the normalized vertical accelerations for airspeed variations. At small length scales (see Figure 5-11a), both Full-Field models predict 25-50% less vertical acceleration. At large length scales (see Figure 5-11c), both Full-Field models predict 15-35% less vertical acceleration. The pilot should be able to distinguish between the Hub-Fixed model and the Full-Field models, but probably not between the Full-Field models themselves.

Roll Acceleration Figure 5-12 shows the normalized roll accelerations for airspeed variations. At all length scales, the Full-Field 3-Dimensional model predicts ~20% more roll acceleration at low airspeeds, the same roll acceleration at moderate airspeeds, and ~20% less roll acceleration at high airspeeds. At all length scales, the Full-Field Normal model predicts 20-50% more roll acceleration. The pilot should be able to distinguish between the Hub-Fixed and the Full-Field Normal model. Conversely, the pilot may not be able to distinguish between the Full-Field 3-Dimensional model and the other models because of its ambiguity.

Pitch Acceleration Figure 5-13 shows the normalized pitch accelerations for airspeed variations. At small length scales (see Figure 5-13a), both Full-Field models predict 275-400% more pitch acceleration. At large length scales (see-Figure 5-13c), both Full-Field models predict 200-375% more pitch acceleration. The pilot should be able to distinguish between the Hub-Fixed and Full-Field models, but probably not between the Full-Field models themselves.

Yaw Acceleration Figure 5-14 shows the normalized yaw accelerations for airspeed variations. At all length scales, there is no noticeable difference between any of the models. Therefore, the pilot may not be able to distinguish between the models.

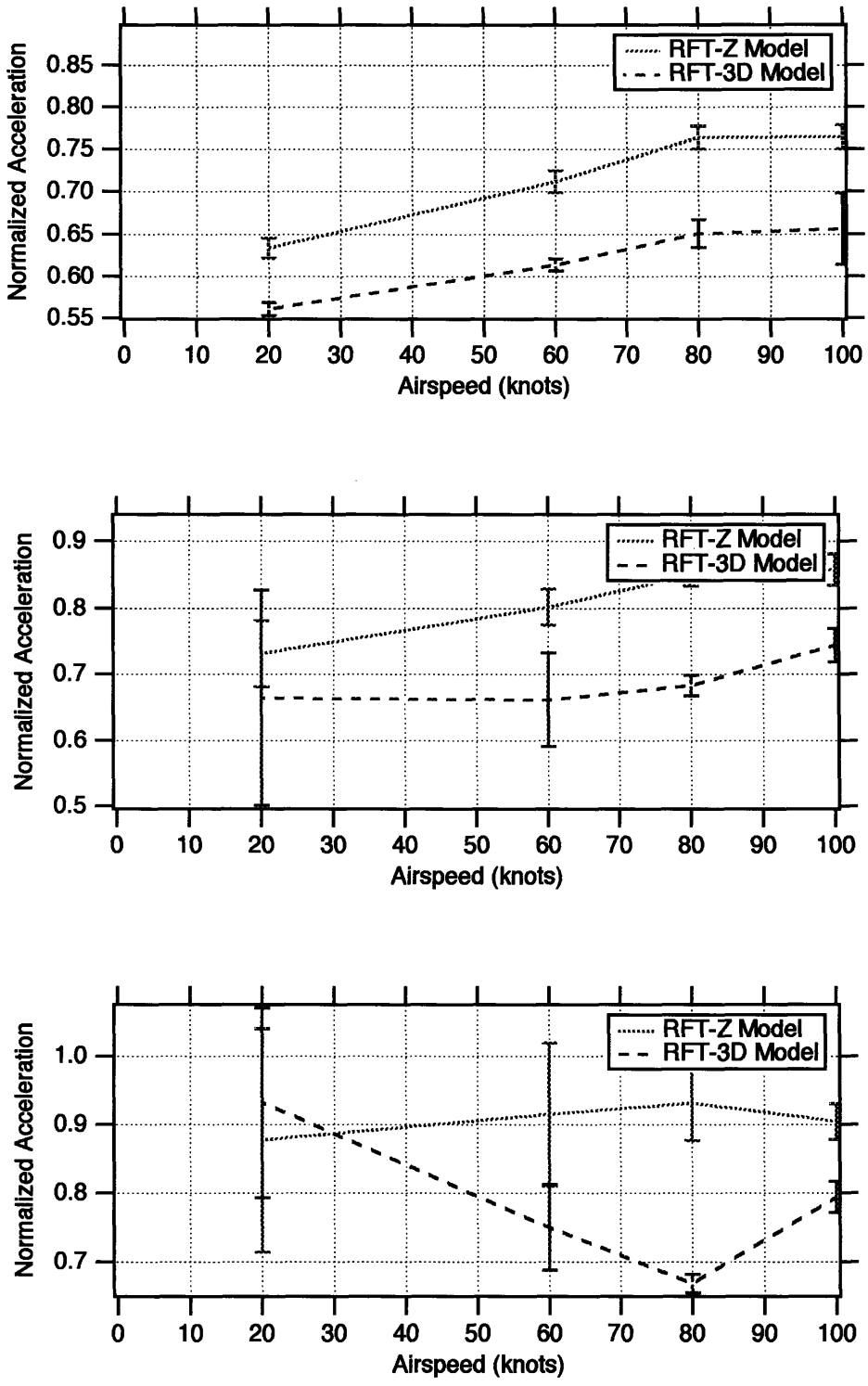

Figure 5-9: Normalized Longitudinal Accelerations for Variations of Airspeed.
(top) L=60 feet, (middle) L=200 feet, (bottom) L=1000 feet

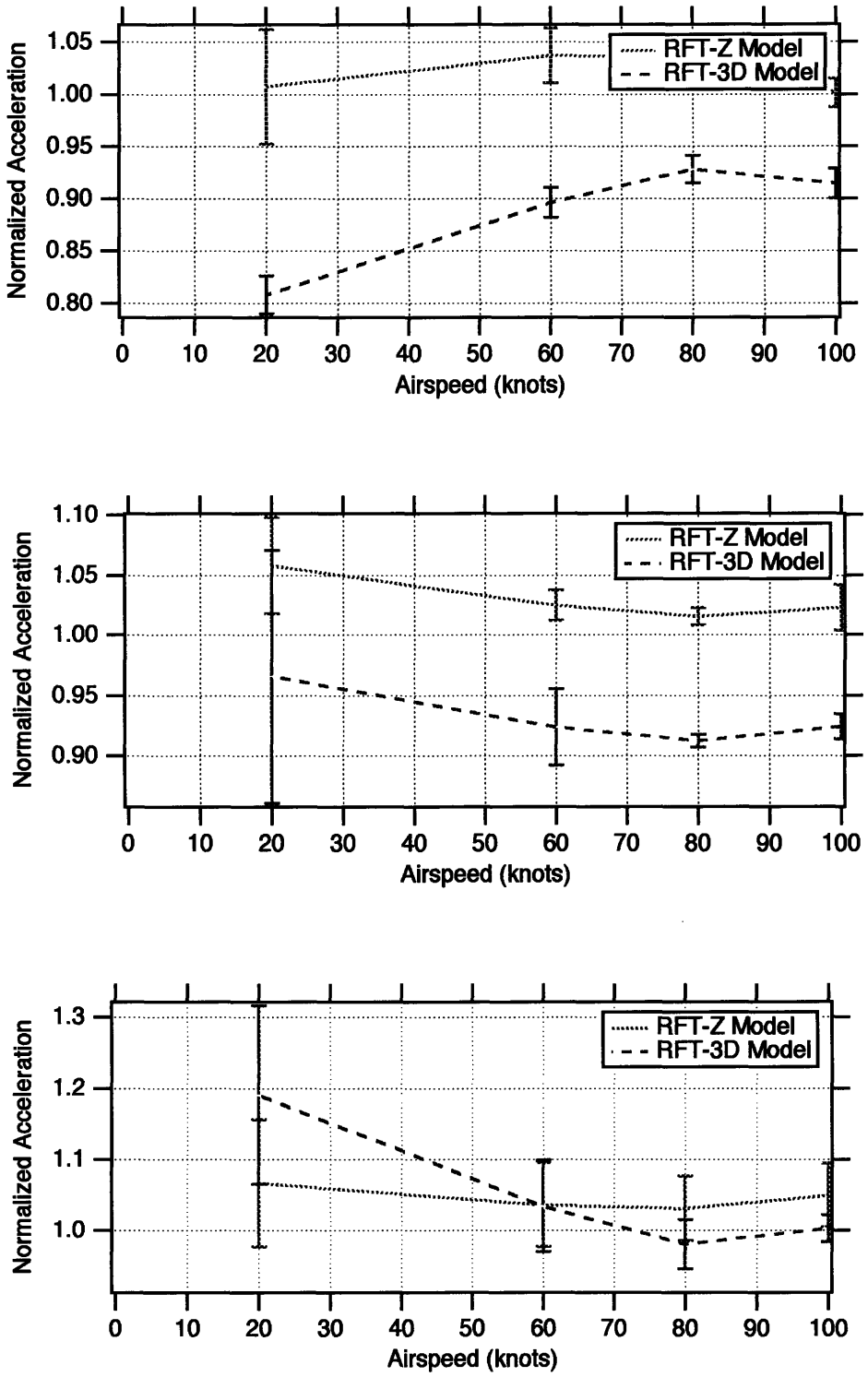

Figure 5-10: Normalized Lateral Accelerations for Variations of Airspeed
(top) L=60 feet, (middle) L=200 feet, (bottom) L=1000 feet

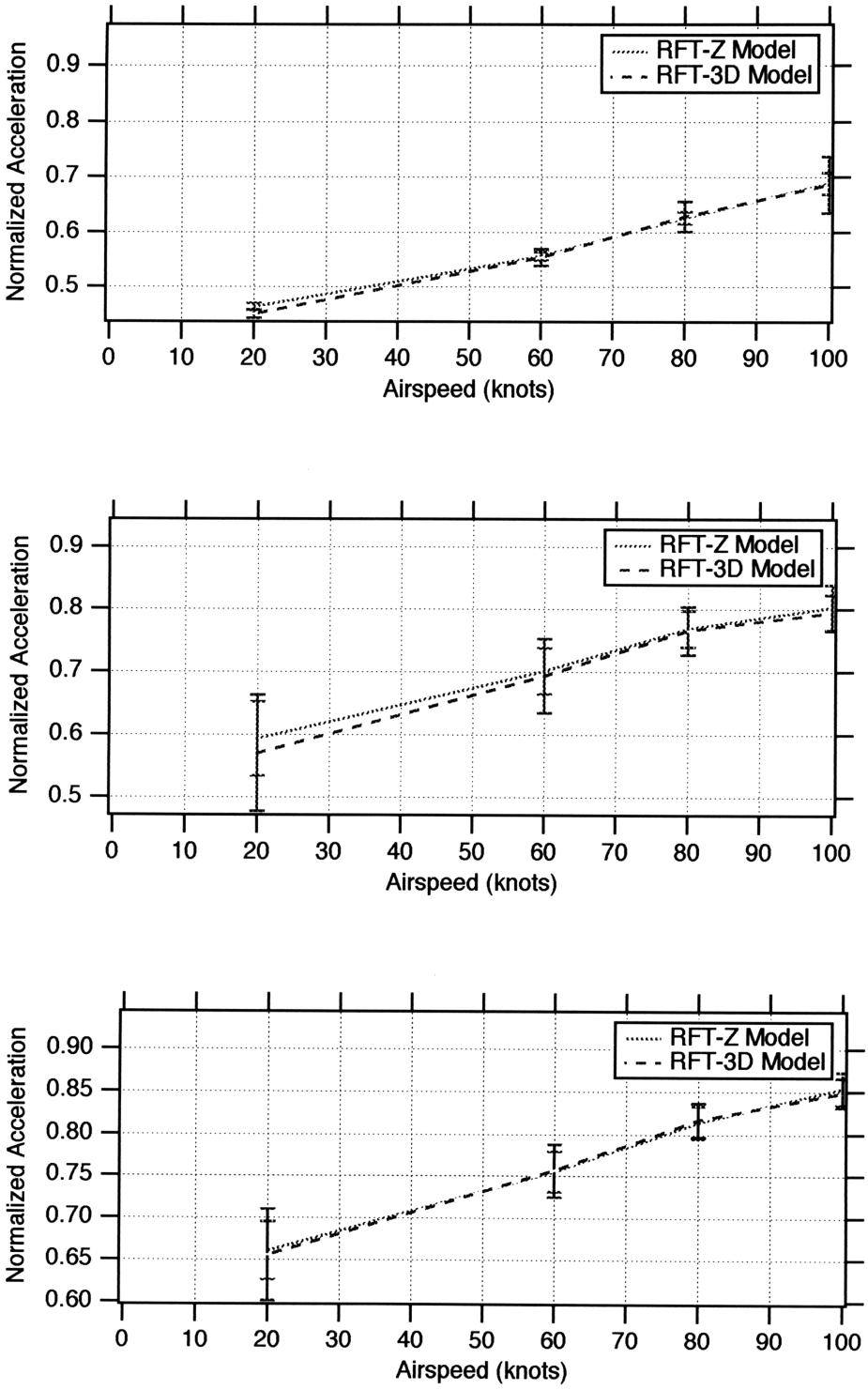

Figure 5-11: Normalized Vertical Accelerations for Variations of Airspeed
(top) L=60 feet, (middle) L=200 feet, (bottom) L=1000 feet

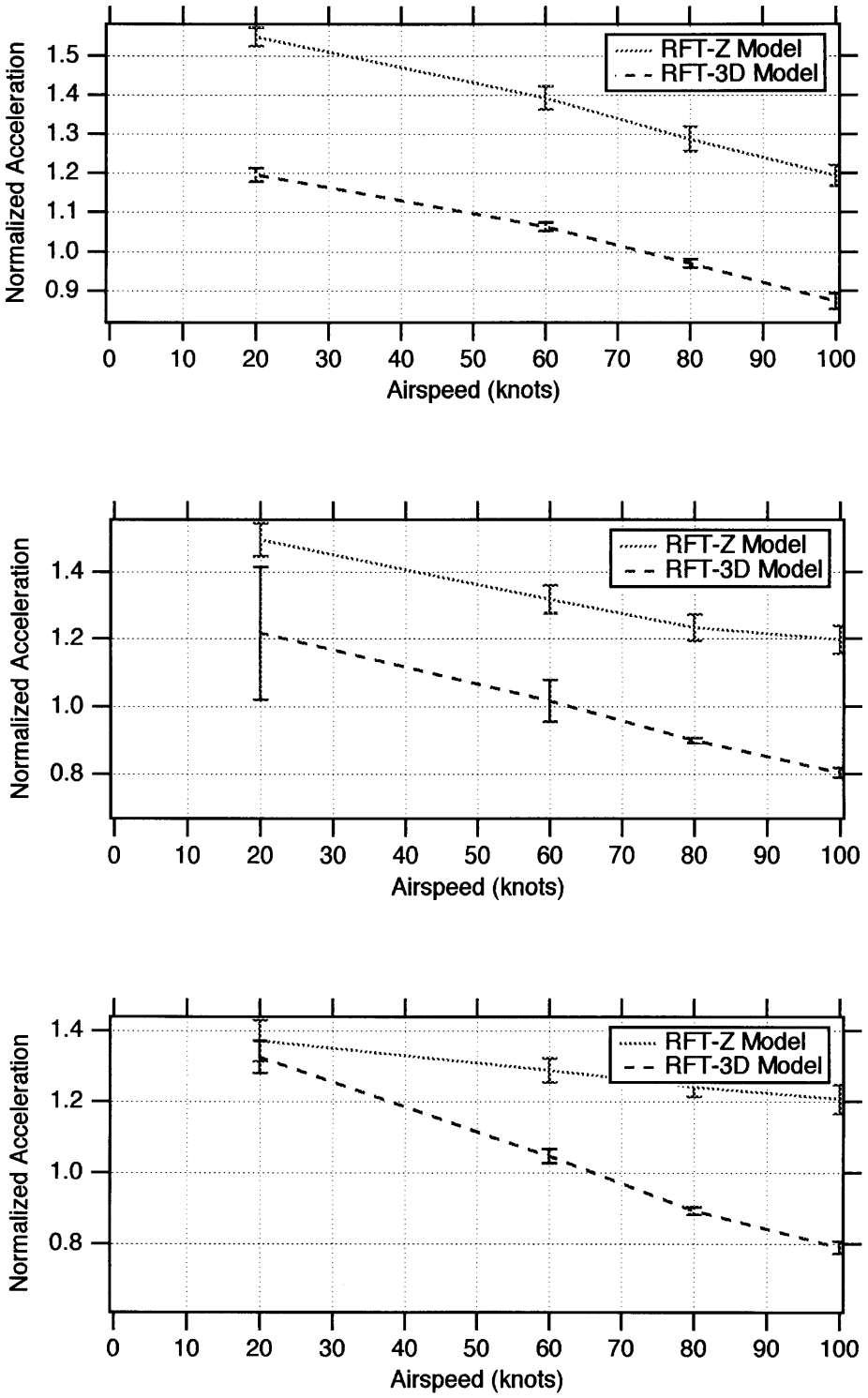

Figure 5-12: Normalized Roll Accelerations for Variations of Airspeed (top) L=60 feet, (middle) L=200 feet, (bottom) L=1000 feet

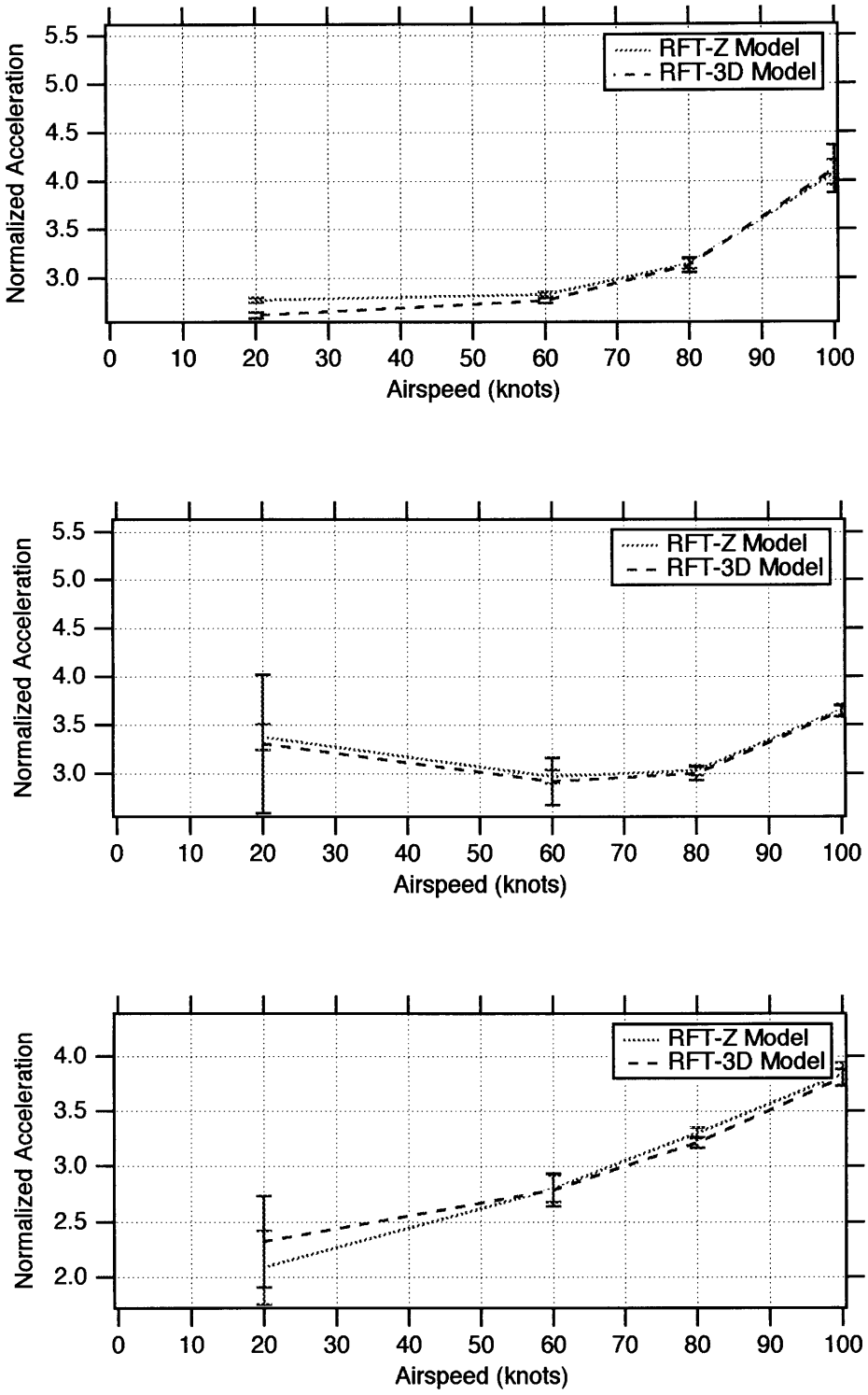

Figure 5-13: Normalized Pitch Accelerations for Variations of Airspeed
(top) L=60 feet, (middle) L=200 feet, (bottom) L=1000 feet

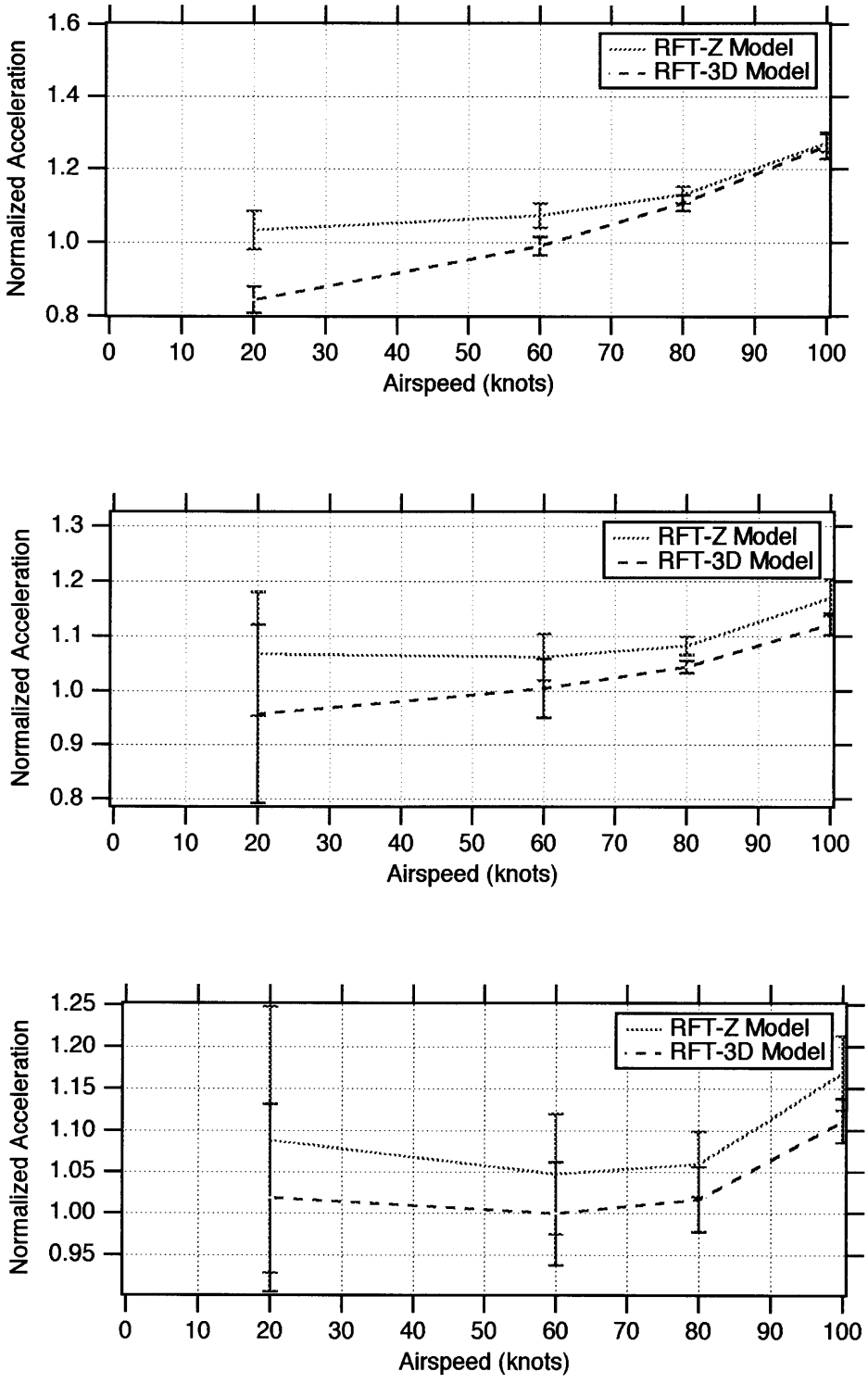

Figure 5-14: Normalized Yaw Accelerations for Variations of Airspeed (top) L=60 feet, (middle) L=200 feet, (bottom) L=1000 feet

5.2.4.2 Effect of Length Scale Variations

Longitudinal Acceleration Figure 5-15 shows the normalized longitudinal accelerations for length scales variations. At low airspeeds (see Figure 5-15a), the Full-Field 3-Dimensional model predicts 20-40% less longitudinal acceleration, and the Full-Field Normal model predicts 10-30% less longitudinal acceleration. Therefore, the pilot should be able to distinguish between the Hub-Fixed model and the Full-Field models, but probably not between the Full-Field models themselves. At high airspeeds (see Figure 5-15c), the Full-Field 3-Dimensional model predicts 15-25% less longitudinal acceleration, and the Full-Field Normal model predicts no noticeable difference in longitudinal acceleration. Therefore, it is unlikely that the pilot will be able to distinguish between the models.

Lateral Acceleration Figure 5-16 shows the normalized lateral accelerations for airspeed variations. At all airspeeds, there is no noticeable difference between any of the models. Therefore, it is unlikely that the pilot will be able to distinguish between the models.

Vertical Acceleration Figure 5-17 shows the normalized vertical accelerations for airspeed variations. At low airspeeds (see Figure 5-17a), both Full-Field models predict 35-50% less vertical acceleration. Therefore, the pilot should be able to distinguish between the Hub-Fixed model and the Full-Field models, but not between the Full-Field models themselves. At high airspeeds (see Figure 5-17c), both Full-Field models predict 10-15% less vertical acceleration. Therefore, it is unlikely that the pilot will be able to distinguish between the models.

Roll Acceleration Figure 5-18 shows the normalized roll accelerations for airspeed variations. At low airspeeds, the Full-Field 3-Dimensional model predicts 20-30% more roll acceleration, and the Full-Field Normal model predicts 40-50% more roll acceleration. The pilot should be able to distinguish between the Hub-Fixed model and the Full-Field models. At high airspeeds, the Full-Field 3-Dimensional model predicts 20-30% less roll acceleration, and the Full-Field Normal model predicts 10-20% more roll acceleration.

Therefore, the pilot should be able to distinguish between the Hub-Fixed and the Full-Field 3-Dimensional model. However, the pilot may not be able to distinguish between the Hub-Fixed model and Full-Field Normal model.

Pitch Acceleration Figure 5-19 shows the normalized pitch accelerations for airspeed variations. At low airspeeds (see Figure 5-19a), both Full-Field models predict 250-350% more pitch acceleration. At high airspeeds (see-Figure 5-19c), both Full-Field models predict 400-500% more pitch acceleration. Therefore, the pilot should be able to distinguish between the Hub-Fixed and Full-Field models, but probably not between the Full-Field models themselves.

Yaw Acceleration Figure 5-20 shows the normalized yaw accelerations for airspeed variations. At all airspeeds, there is no noticeable difference between any of the models. Therefore, it is unlikely that the pilot will be able to distinguish between the models.

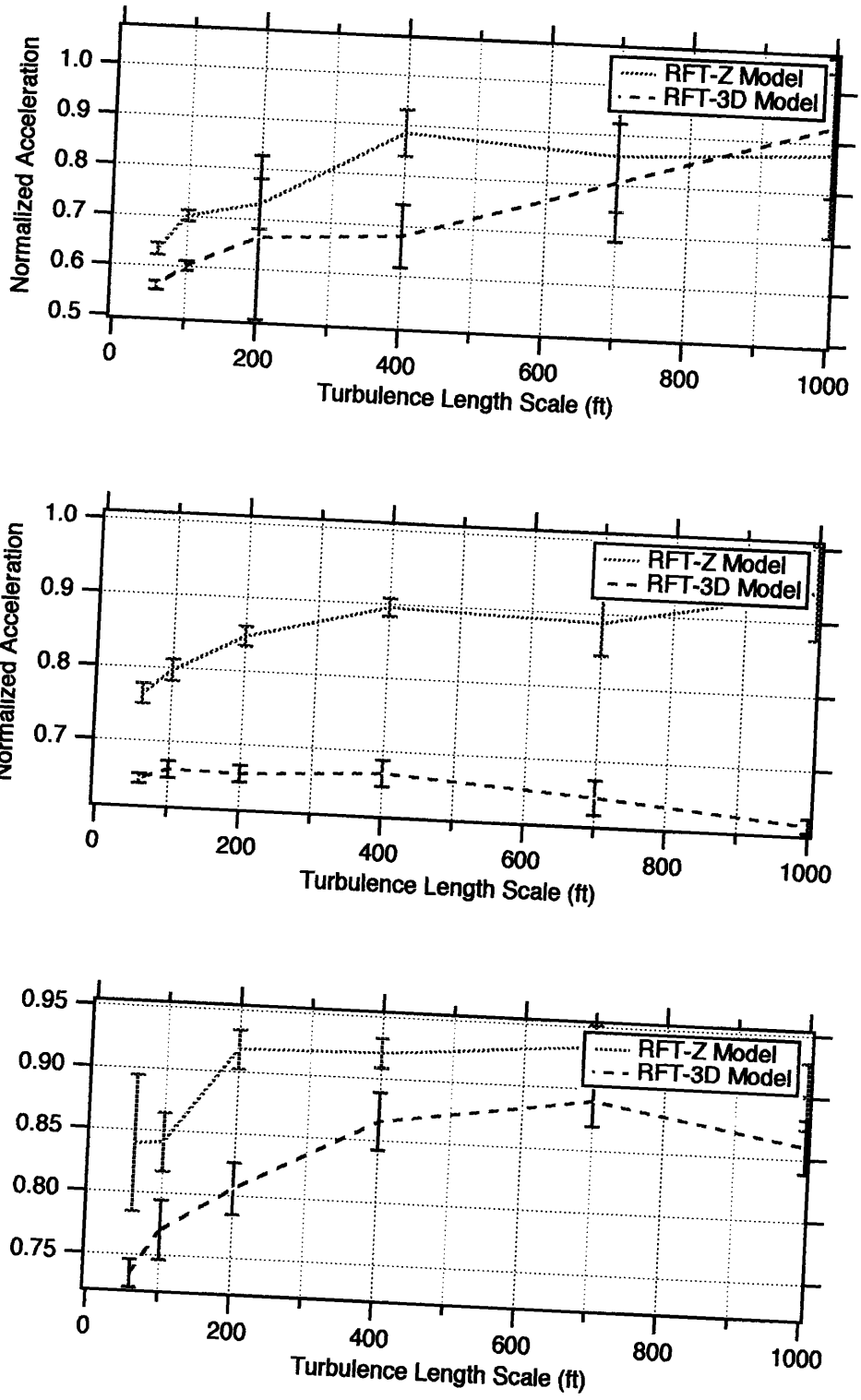

Figure 5-15: Normalized Longitudinal Accelerations for Variations of Length Scale
(top) V=20 knots, (middle) V=60 knots, (bottom) V=100 knots

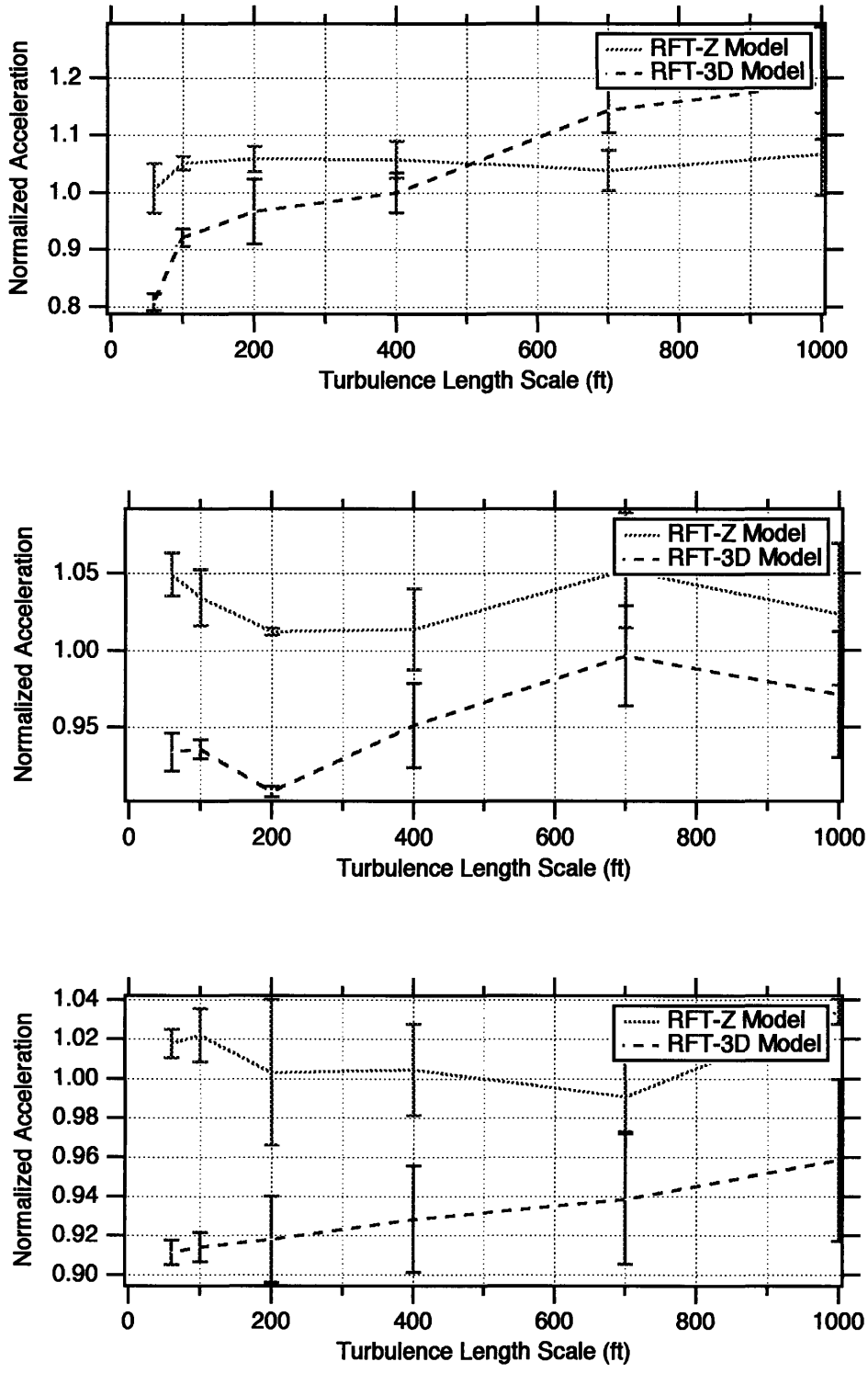

Figure 5-16: Normalized Lateral Accelerations for Variations of Length Scale
(top) V=20 knots, (middle) V=60 knots, (bottom) V=100 knots

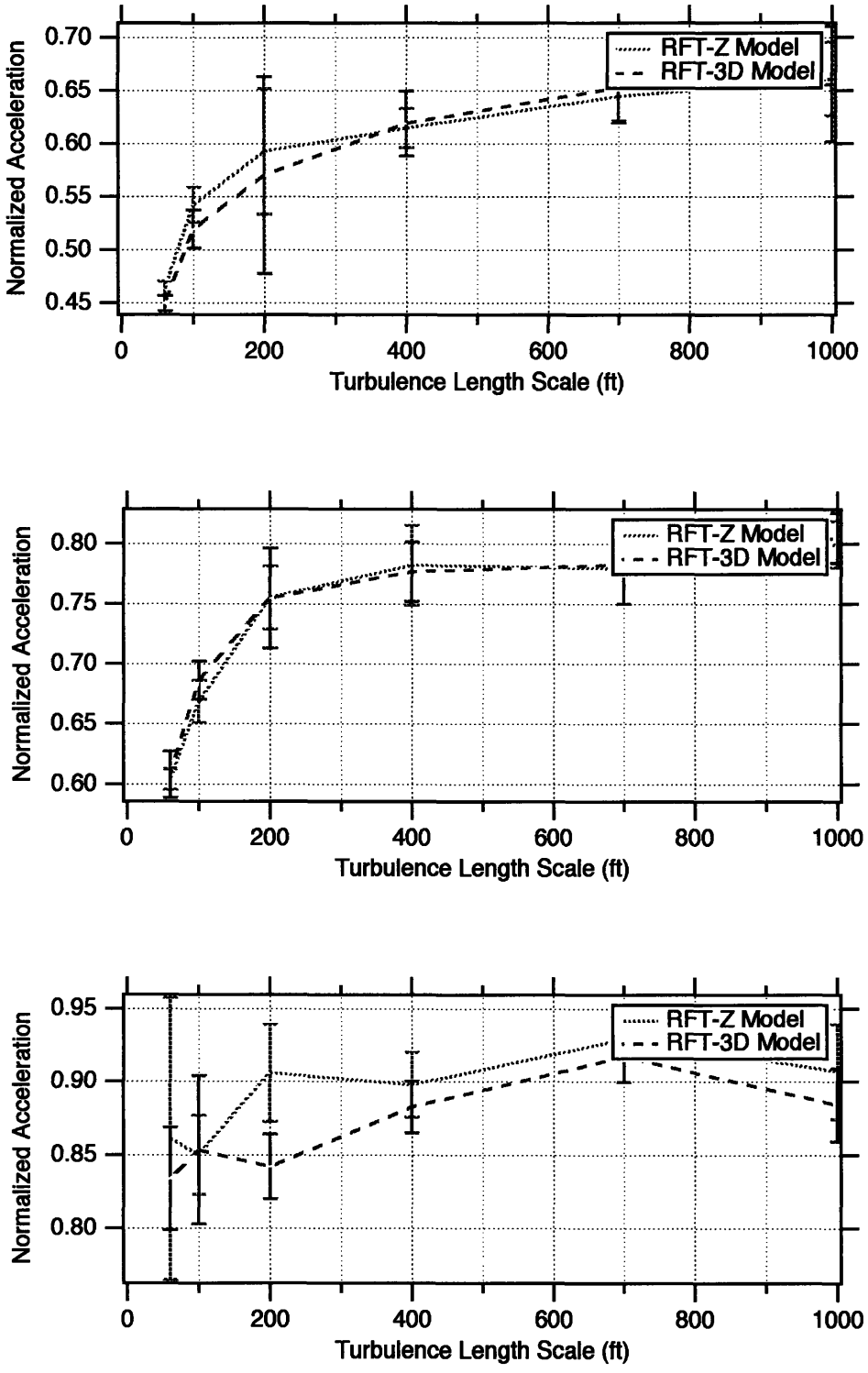

Figure 5-17: Normalized Vertical Accelerations for Variations of Length Scale
(top) V=20 knots, (middle) V=60 knots, (bottom) V=100 knots

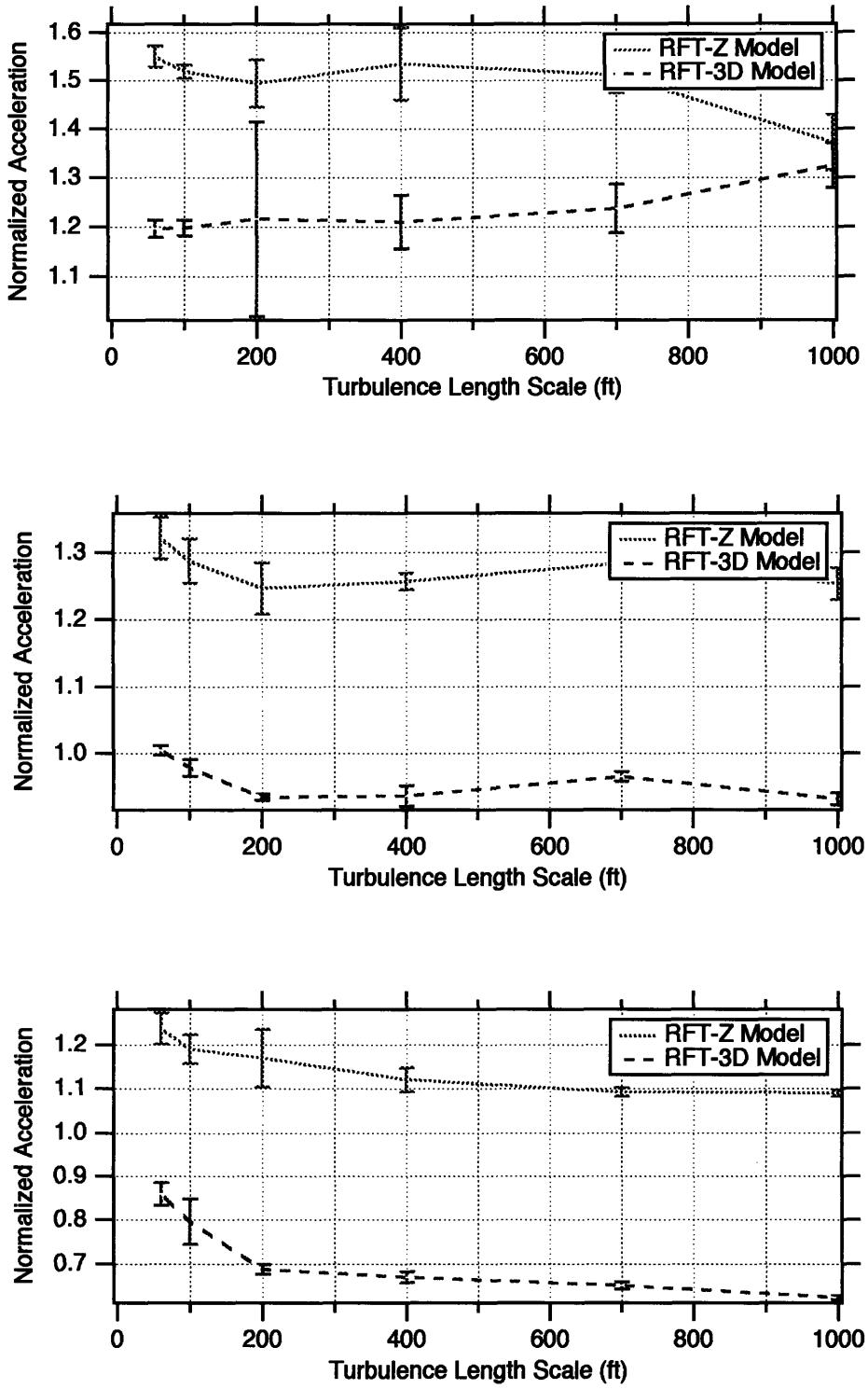

Figure 5-18: Normalized Roll Accelerations for Variations of Length Scale
(top) V=20 knots, (middle) V=60 knots, (bottom) V=100 knots

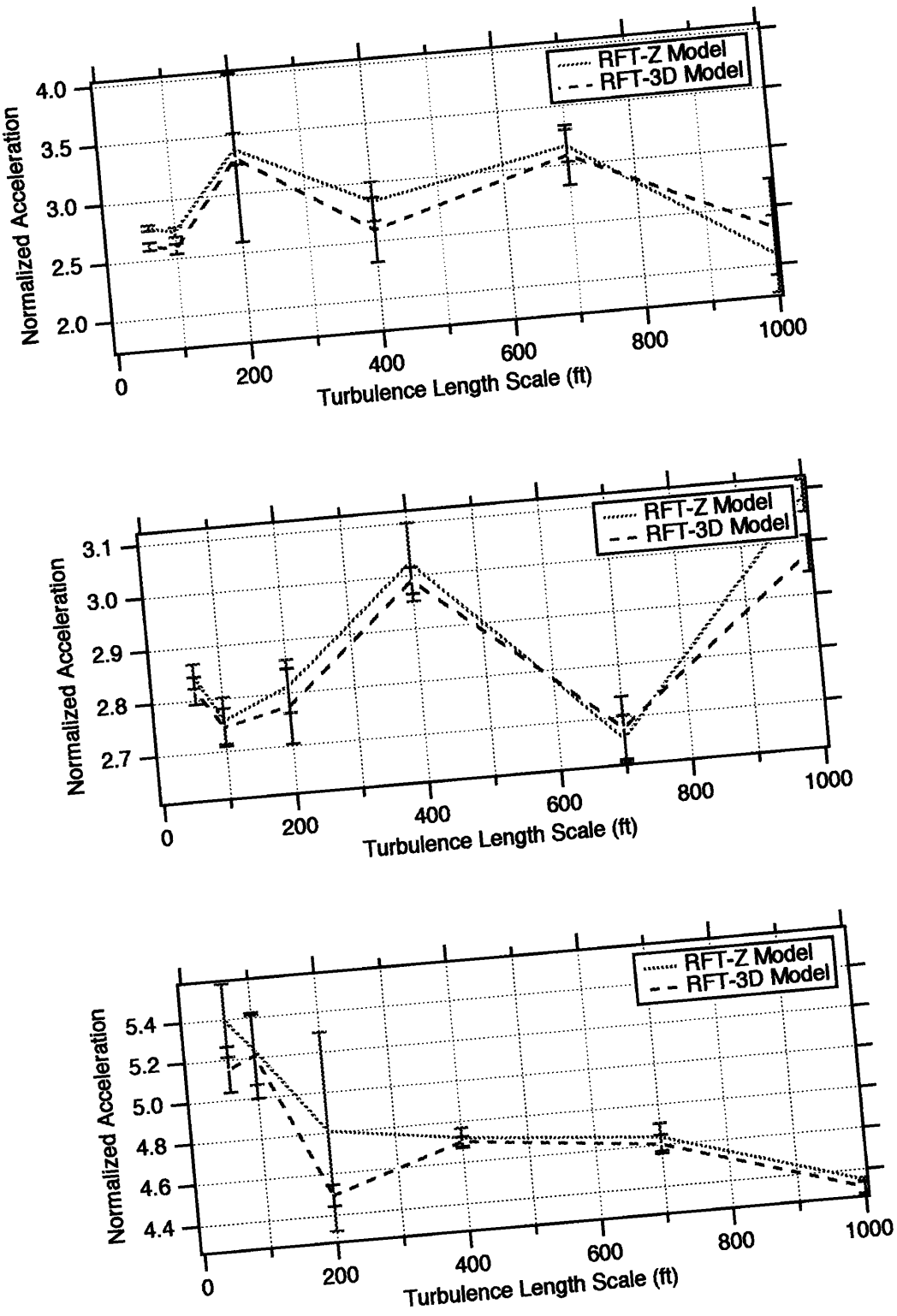

Figure 5-19: Normalized Pitch Accelerations for Variations of Length Scale
(top) V=20 knots, (middle) V=60 knots, (bottom) V=100 knots

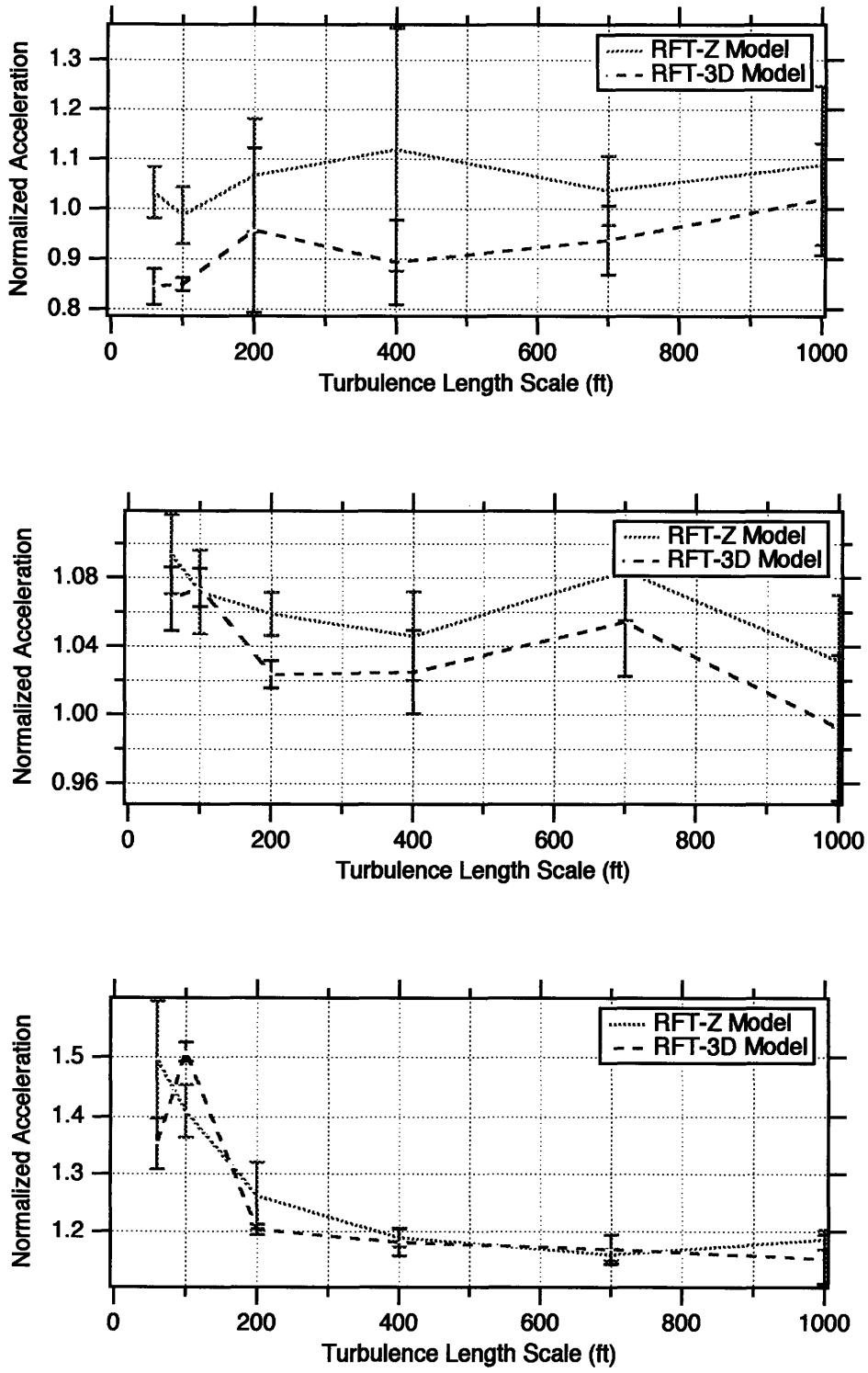

Figure 5-20: Normalized Yaw Accelerations for Variations of Length Scale
(top) V=20 knots, (middle) V=60 knots, (bottom) V=100 knots

5.2.5 Discussion of Non-Real-Time Simulation

From these non-real-time results, several interesting features were found from the aircraft response comparisons.

Inspection of the translational results (see Figures 5-9 through 5-11 and 5-15 through 5-17) shows that, without exception, the Full-Field Normal model predicts more longitudinal and lateral acceleration than the Full-Field 3-Dimensional model, but both models predict nearly the same vertical accelerations. Both Full-Field models predict less longitudinal, lateral and vertical accelerations than the Hub-Fixed model. Therefore, atmospheric turbulence models which do not include spatial variations of the velocity field may over predict (by as much as 60% in some flight conditions) the rms amplitude of linear accelerations. The reason for this difference is easily explained by the physics of the velocity field. For models without spatial variation, the mean turbulence velocity over the entire aircraft, at every instance, will be exactly equal to the sampled velocity. However, for models with spatial variation, the mean turbulence velocity over the entire aircraft, at each instance, will be statistically related to the turbulence length scale and the dimensions of the aircraft. In the hypothetical limit, as the length scales becomes small with respect to the dimensions of the aircraft, the mean turbulence velocity over the entire aircraft at each instance will be nearly zero, and no linear accelerations should be induced by the atmospheric turbulence field.

The rotational results (see Figures 5-12 through 5-14 and 5-18 through 5-20) are more complicated, so each axis will be discussed separately. Inspection of the roll results shows that the Full-Field Normal model predicts more roll acceleration than the Full-Field 3-Dimensional model and the Hub-Fixed model. Again, the reason for this difference can be easily explained by the physics of the velocity field. At low airspeeds, the spatial variation of the vertical velocity component causes both Full-Field models to predict more roll acceleration than the Hub-Fixed model. At higher airspeeds, however, the spatial variations of the longitudinal and lateral velocity components cause the Full-Field 3-

Dimensional model to actually predict less roll acceleration than the Hub-Fixed model. The effect of variations of the longitudinal and lateral velocity components eventually diminish the effect of variation of the vertical velocity component. Therefore, a uniform lateral gust will produce a roll disturbance of order equal to the roll disturbance produced by a spatially varying vertical gust. Caution must be used in drawing additional conclusions about the validity of either Full-Field model, since it is not at all clear from these results which produces more realistic roll disturbances.

Inspection of the pitch results shows that both Full-Field models predict more pitch acceleration than the Hub-Fixed model. Therefore, atmospheric turbulence models which do not include spatial variations of the vertical velocity component may greatly under predict (by as much as a factor of 4) the amplitude of pitch accelerations. There does not seem to be a significant effect on pitch accelerations by the spatial variations of the longitudinal and lateral velocity components. However, this may only be characteristic of the tandem main rotor configuration. At low airspeeds and in hover, the pitch excursions due to longitudinal gusts should be comparable to the roll excursions due to lateral gusts, for the single main rotor configuration.

Finally, inspection of the yaw results show that neither Full-Field model predicts much change from the Hub-Fixed model. For trimmed and level flight, a large part of the yawing moment is due to asymmetric velocity distributions along the aircraft fuselage. Each of the atmospheric turbulence models examined for this research assumed the velocity field was uniform along the fuselage and its velocity was equal to that velocity sampled at the aircraft center of gravity. The remaining part of the yawing moment due to turbulence would be the differential lateral tilt of the lift vector between the two main rotors. This is a small fraction of an already small quantity, and it can be seen that the spatial variation of the velocity field over the main rotors but not along the fuselage does not significantly change the predicted yaw accelerations due to atmospheric turbulence.

5.3 Piloted Evaluation

The piloted evaluation procedure for the flight simulation experiment is described in Chapter 4. The results of this evaluation consisted of (1) pilot surveys and general comments and (2) a limited amount of simulated aircraft data which was recorded during the flight task.

5.3.1 Overall Flight Simulator Fidelity

Before discussing the results of the piloted evaluation, it is relevant to outline some of the difficulties which were encountered during the flight simulation experiment. Boeing Helicopters' flight simulator is a research simulator, typically used for aircraft control systems and handling qualities investigations. It is not meant to be as physically realistic as a training simulator. Therefore, it is often necessary for the pilots to overlook some minor dissimilarities between the simulation and the real aircraft. The general types of discrepancies encountered during the flight simulation experiment included control stick differences, cockpit display differences and motion cue differences. The CH-47D Chinook simulation had been inactive for several months prior to the flight simulation experiment, and the original tandem helicopter simulation did not include a blade element rotor model. Simultaneous integration of the blade element rotor model and full-field atmospheric turbulence model represented a considerable enhancement in the simulation's complexity, and minor glitches were still being worked out even as the flight simulation experiment was being conducted. The cab used for CH-47D simulation was actually the same cab used for V-22 simulation. Therefore, the cockpit was not a duplicate of the CH-47D's actual cockpit, and this was the source of several simulation infidelities.

5.3.1.1 Control Stick Differences

First, there were minor differences in the control stick forces. All of the pilots complained that the control stick force feel settings were somewhat unrealistic. After

investigation, it was determined that the control stick breakout force[2] did not appear to be unreasonable, but the control stick damping may have been slightly too high. Also, the trim release button was difficult to press. This caused a small jump in the controls whenever it was pressed. Ordinarily, these discrepancies would have a negligible impact on the simulation, and the pilot simply ignores them. However, during a precision hover task in moderate turbulence, the pilot must be able to smoothly supply inputs to the control sticks. If the control stick damping is too high or the trim release button is too stiff, the pilot is unable to supply fine control adjustments, and his workload will be increased above what he would expect in the real aircraft.

5.3.1.2 Cockpit Display Differences

Second, the cockpit displays were slightly different than the actual CH-47D displays. The CH-47D has analog displays, while the V-22 has a glass cockpit consisting of numerous multi-function displays. Initially, since it was the V-22 cab, no torque indicator was included in the center console in front of the pilot. Helicopter pilots rely on the torque indicator as a way to determine where they should hold the collective stick. This allows the pilots to maintain a certain flight condition without directly accounting for humidity or temperature. Without this instrumentation, the pilot is required to use visual cues from the outside scenery and motion cues from their vestibular system. This substitution increases the pilot's workload during the precision hover task. In the actual aircraft, these alternate sensory cues contain high frequency components which the pilot does not want. Additionally, in the simulator, these sensory cues are attenuated by the visual system's resolution and the motion system's washout filtering. Pilot A did not have the torque indicator during his flight simulation session. Pilots B and C did have the torque indicator during their sessions.

[2] The breakout force is the initial force the pilot must overcome to move the control stick.

5.3.1.3 Motion Cue Differences

Previous investigations of realistic atmospheric turbulence simulation suggested that it may be important to include motion cues related to turbulence-induced structural dynamics [2]. For example, "ringing" of the fuselage after encountering a sharp gust may be important for the simulated atmospheric turbulence to feel realistic. The servo-actuators which controlled the position of the six hydraulic cylinders of the motion base had an effective frequency range of approximately 7 Hertz. Figure 5-21 shows the ratio of measured cab accelerations to commanded model accelerations for Boeing Helicopters' motion base flight simulator in an open loop single-axis configuration. These curves are reasonably flat until break frequencies of approximately 4 Hertz in the vertical axis and approximately 7 Hertz in the longitudinal and lateral axes. The bandwidth of the motion base may be increased (or decreased) for individual simulation sessions by tuning the servo-actuators. Ideally, the bandwidth of the motion base should include the entire frequency range of important aircraft motions and human perception. In the case of atmospheric turbulence modeling, this would be equivalent to a bandwidth of approximately 10 Hertz. However, the servo-actuators were kept at their nominal settings for the flight simulation experiment. It was decided that the flight simulator should remain in the same general configuration it would be in during typical day-to-day operations. Thus, the results of this research would directly address the issue of the relevance of full-field atmospheric turbulence modeling for ordinary piloted flight simulation of rotorcraft. Unfortunately, the frequency content turbulence induced motion cues was limited by the servo-actuators' bandwidth. For nominal settings of the servo-actuators, the measurements show that Boeing Helicopters' flight simulator adequately supplies turbulence-induced motion cues in the low frequency range, but, like other aircraft simulators, may inadequately supply turbulence-induced motion cues in the high frequency range.

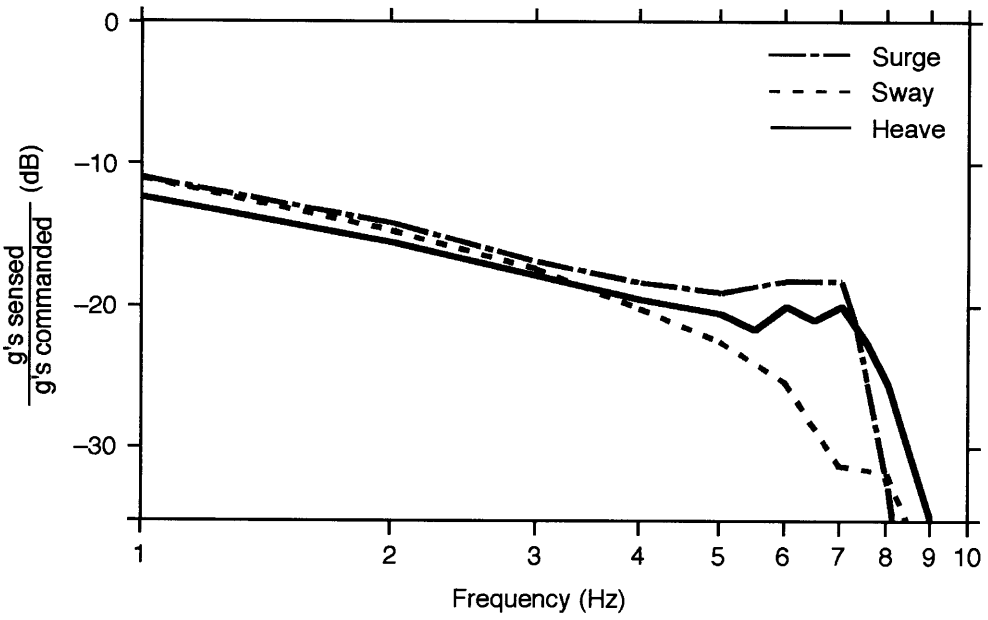

Figure 5-21: Acceleration Response of Boeing Helicopters' Motion Base Flight Simulator in an Open Loop Single Axis Configuration

Apart from the frequency content is the relative amplitude of the simulated motion to the actual motion. The servo-actuators' gains can be adjusted to utilize the greatest amount of the allowable cab travel without contacting the mechanical stops. Initially, it was felt that like the bandwidth, the gains should remain at the nominal settings also. Therefore, Pilot A had nominal motion base settings during his sessions Later, it was decided that the motion base configuration should be changed, since it was possible that attenuation of the motion cues was responsible for the differences between the atmospheric turbulence models not being perceptible. Therefore, Pilots B and C had increased servo-actuator gains during their sessions. This made the cab utilize more of its allowable travel, and thus, produce more perceptible motion cues.

5.3.2 Pilot Survey Results

5.3.2.1 Pilot Background Survey

The results of the pilot background survey are given in Table 5.2. The pilots' rankings of the relative importance of turbulence induced exursions for each axis are listed. The pilots all agreed that atmospheric turbulence affects the helicopter through uncommanded pitch attitude changes. Heave excursions were considered by Pilots A and B to be an important effect of gust encounters. Finally, yaw excursions were also considered important, but Pilot A suggested that this was not because the excursions were large but because the pilot was more sensitive to motions about this axis than the other axes. The pilots also generally agreed that atmospheric turbulence did not have an important effect on either lateral or roll disturbances.

Table 5.2: Pilot Ranking of the Importance of Aircraft Excursions Due to Atmospheric Turbulence

	Pilot A	Pilot B	Pilot C
Longitudinal	–	6	3
Lateral	–	5	6
Vertical	1	1	4
Roll	3	4	5
Pitch	2	2	1
Yaw	1	3	2

5.3.2.2 Flight Simulation Realism Survey

Several questions on the Flight Simulation Realism Survey were ill-conceived and ultimately did not yield much useful information. However, all of the questions are discussed here with the intention of not only relaying the results of this investigation but also improving future piloted evaluations. The pilot rating scale for all of the questions was as follows: a rating of 1 meant the simulated turbulence had too little of the stated quality, a rating of 7 meant the simulated turbulence had too much of the stated quality and a rating of 4 meant the simulated turbulence had the correct level.

Question 1: Turbulence Intensity: Table 5.3 offers the pilots' responses to Question 1 of the flight simulation survey. Pilots A and B indicated that the Full-Field 3-Dimensional model was only slightly more severe than the Hub-Fixed and Full-Field Normal models. Pilot C indicated that the Hub-Fixed model was considerably more severe than the Full-Field models. Unfortunately, this shows the difficulties of a subjective analysis. Pilot C found the vertical axis overly sensitive to control, and this resulted in his perception of severe intensity. If the pilot feels one axis is disproportionate to the other axes, like the vertical axis, it requires him to weight the excursions in all axes to determine an effective turbulence intensity. If the pilot weights the disproportionate axis heavily, the perceived

intensity will be severe, whereas if the piloted weights the disproportionate axis lightly, the perceived intensity will be light.

Table 5.3: Pilot Responses to Question 1 of the Flight Simulation Survey - Turbulence Intensity

	Hub-Fixed	Full-Field 1-D	Full-Field 3-D
Pilot A	2	2	3
Pilot B	5	5	6
Pilot C	6	3	3

Question 2: Overall Realism: Table 5.4 offers the pilots' responses to Question 2 of the flight simulation survey. Pilot A indicated that the Full-Field 3-Dimensional model was the most realistic model. Pilots B indicated that the Full-Field Normal model was only slightly more realistic than the other models. Lastly, Pilot C did not indicate a difference between the models on the flight simulation survey, but his comments during the experiment implied that the Full-Field Normal model was the most realistic model.

Table 5.4: Pilot Responses to Question 2 of the Flight Simulation Survey - Overall Realism of Simulated Turbulence

	Hub-Fixed	Full-Field 1-D	Full-Field 3-D
Pilot A	1	1	4
Pilot B	5	6	2
Pilot C	3	3	3

Question 3 Relative Amplitudes: Table 5.5 offers the pilots' responses to Question 3 of the flight simulation survey. The answers for given by Pilots A and C correlated well with their answers of Question 2. Pilot A indicated that the relative amplitudes were most realistic for the Full-Field 3-Dimensional model which supported his answer to Question 2. Pilot C indicated that the relative amplitudes were most realistic for the Full-Field Normal model which again agreed with his answer to Question 2. Conversely, Pilot B indicated

that the relative amplitudes were most realistic for the Hub-Fixed model, but he indicated the Full-Field Normal model was the most realistic model in Question 2. Pilot B also commented during the experiment that he felt the Hub-Fixed case modeled the turbulence best. Unfortunately, there is no general consensus between the pilots about which model was the most realistic.

Table 5.5: Pilot Responses to Question 3 of the Flight Simulation Survey - Relative Amplitudes of Aircraft Response

	Axis	Hub-Fixed	Full-Field 1-D	Full-Field 3-D
Pilot A	Surge	–	–	–
	Sway	–	–	–
	Heave	6	6	5
	Pitch	2	2	4
	Roll	2	2	3
	Yaw	3	3	3
Pilot B	Surge	2-3	4	3
	Sway	4	4	2-3
	Heave	5	6	6-7
	Pitch	3-4	5	3
	Roll	3	5	2
	Yaw	3-4	3	3-4
Pilot C	Surge	3	4	3
	Sway	4	4	3
	Heave	3	3	2
	Pitch	3	4	2
	Roll	3	4	3
	Yaw	2	4	2

Question 4 Repetitive Pattern: Pilot B indicated that there was a repetitive element in the simulated atmospheric turbulence, while Pilots A and C did not. The autospectral densities of the simulated velocity field have been shown to be correct. Therefore, Pilot B's remarks were taken to be an anomaly.

Question 5 Frequency Content: Unfortunately, the overall simulation motion fidelity did not allow for the pilots to distinguish between the low frequency and the high frequency content in the velocity field. The pilots tended to indicate the low frequency content of their control inputs and not the low frequency content of the atmospheric turbulence for the answer to this question. None of the pilots were able to discern the high frequency content.

Question 6 Sudden Large Amplitude Gusts: Table 5.6 gives the pilots' responses to Question 6 of the flight simulation survey. Pilots B and C indicate that the occurrence of large amplitude gust is moderately realistic. Pilot A, however, indicates the occurrence is too seldom. Unfortunately, Pilot A flew the flight simulator with the nominal gain settings. Therefore, it is likely that his response indicates that he was not feeling the turbulence induced accelerations, because they were below his sensory threshold. Meanwhile, Pilot B's and C's response indicates that these motions were discernible with larger gain settings.

Table 5.6: Pilot Responses to Question 6 of the Flight Simulation Survey - Occurrence of Sudden Large Amplitude Gusts

	Hub-Fixed	Full-Field 1-D	Full-Field 3-D
Pilot A	2	2	3
Pilot B	3-4	4	3
Pilot C	4	4	4

Question 7 Cooper-Harper Ratings: Although Jacobsen and Joshi [18] used this question in their fixed wing aircraft handling qualities investigation, its usefulness in this research was not found. Almost without exception, Pilots A, B and C gave the aircraft-flight task-atmospheric turbulence model combination a handling qualities rating of 5 or 6. This corresponds to the condition where the aircraft characteristics are "very objectionable" and "adequate performance requires extensive pilot compensation."[4] Unfortunately, the

meaning of this information is ambiguous. A handling qualities rating of 6 may correspond to accurate turbulence modeling and a not so well behaved aircraft, inaccurate turbulence modeling and a well-behaved aircraft or some combination of these scenarios. Also, infidelities in the flight simulator that are exacerbated by realistic turbulence modeling, but completely unrelated to it, may worsen the handling qualities rating given by the pilot. Therefore, this question does not seem relevant to the flight simulation experiment.

5.3.3 Simulated Aircraft Data Results

Only the simulated aircraft data recorded during the final simulation session with Pilot C will be presented in this document. Tables 5.7 through 5.9 show the rms aircraft accelerations measured during the three tasks of the flight simulation experiment. The shaded elements in each table indicate the rms aircraft accelerations which are correlated to Pilot C's responses to Question 3 of the Flight Simulation Survey. Notice, for the precision hover task, all of the aircraft accelerations are correlated to the pilot's responses, but during the other tasks, only the heave and pitch accelerations are correlated. The pilot's responses correspond directly to the atmospheric turbulence model which resulted in the largest rms accelerations. It should not be concluded from this behavior, however, that these accelerations model the atmospheric turbulence best. The acceleration commands given to the motion base are significantly attentuated from the accelerations calculated in the aircraft model. Therefore, it is possible that while the attenuated accelerations are much less than those the pilot expects, but the calculated accelerations may be more than those the pilot expects. Also, the fourth column of each table shows that the real-time simulated aircraft data do not consistently correlate to the non-real-time simulated aircraft data. While the vertical and pitch accelerations correlate reasonably well, the lateral, roll and yaw accelerations are typically inconclusive, and the longitudinal acceleration actually show no correlation to the non-real-time results.

Table 5.7: RMS Aircraft Accelerations During the Flight Simulation Experiment. Pilot C Performing the Precision Hover Task.

	Precision Hover Task			Non-Real-Time Correlation
	Hub-Fixed	Full-Field 1-D	Full-Field 3-D	
$\dot{u}$ (feet/sec^2)	0.6468	0.7103	0.6911	no
$\dot{v}$ (feet/sec^2)	0.8447	0.6728	0.5098	yes
$\dot{w}$ (feet/sec^2)	2.5754	2.1172	1.7535	yes
$\ddot{\theta}$ (deg/sec^2)	2.3862	2.9701	2.6638	yes
$\ddot{\phi}$ (deg/sec^2)	3.3271	4.9427	2.8443	—
$\ddot{\psi}$ (deg/sec^2)	0.9037	1.1272	0.6832	—

Table 5.8: RMS Aircraft Accelerations During the Flight Simulation Experiment. Pilot C Performing the Level Cruise Task.

	Level Cruise Task			Non-Real-Time Correlation
	Hub-Fixed	Full-Field 1-D	Full-Field 3-D	
$\dot{u}$ (feet/sec^2)	2.0892	1.7676	2.1719	no
$\dot{v}$ (feet/sec^2)	3.5438	3.3298	3.6120	no
$\dot{w}$ (feet/sec^2)	6.1246	5.2470	3.8794	yes
$\ddot{\theta}$ (deg/sec^2)	4.2636	5.7835	4.4674	yes
$\ddot{\phi}$ (deg/sec^2)	2.9994	3.8954	2.9404	yes
$\ddot{\psi}$ (deg/sec^2)	1.6689	1.5689	2.1025	—

Table 5.9: RMS Aircraft Accelerations During the Flight Simulation Experiment. Pilot C Performing the Coordinated Turn Task.

	Coordinated Turn Task			Non-Real-Time Correlation
	Hub-Fixed	Full-Field 1-D	Full-Field 3-D	
$\dot{u}$ (feet/sec^2)	5.8862	6.0254	6.8432	no
$\dot{v}$ (feet/sec^2)	6.3884	5.9899	6.2652	no
$\dot{w}$ (feet/sec^2)	8.6838	8.1758	6.3527	yes
$\ddot{\theta}$ (deg/sec^2)	4.3332	5.6173	4.7605	yes
$\ddot{\phi}$ (deg/sec^2)	4.0485	4.5061	3.0085	—
$\ddot{\psi}$ (deg/sec^2)	2.7480	2.9756	2.9724	—

Chapter 6

Conclusions

The research performed in this thesis has extended the current state-of-the-art of rotorcraft atmospheric turbulence modeling to include real-time piloted flight simulation capabilities. The new Full-Field atmospheric turbulence model describes the velocity field which is experienced by an arbitrary aerodynamic or structural component of a general configuration tandem rotor helicopter. The model developed in this work is quite different and substantially more numerically robust than earlier atmospheric turbulence models of this type, owing to the novel computation algorithm employed to achieve real-time flight simulation. The velocity field sampled by any point on the aircraft is approximated by a series of sinusoids having equal amplitudes and specially chosen frequencies. The spatial frequencies for the harmonics in the Full-Field model are found by evaluating the exact integrals of the von Kármán autospectral densities. An investigation of the effect of atmospheric turbulence on aircraft handling qualities was performed using the Full-Field model. Pilot evaluations were conducted to determine the increase in flight simulation realism and the extent of pilots perception of differences between the aircraft's response to the Full-Field models and to the traditional Hub-Fixed model.

The major conclusions which may be drawn from the current work are summarized in the following items.

1. Practical computational limitations require the use of a more efficient algorithm than that used for other recent rotorcraft investigations of atmospheric turbulence. These methods, which approximate the velocity field by a series of sinusoids with evenly spaced frequencies and specially chosen amplitudes, are not capable of real-time execution. Clearly, the exact integration required for the Full-Field model is more complicated. However, the additional mathematical complexity required to choose the spatial frequency grids is entirely justified by the several orders of magnitude decrease in computation time. For the Full-Field model with exact integration, a series with 225 harmonics is adequate to meet the spectral fidelity requirements and attain real-time execution. Conversely, for constant linear or logarithmic spacing, a series containing greater than 40,000 harmonics is still inadequate to meet the spectral fidelity requirements and does not attain real-time execution.
2. Exact integration of the von Kármán autospectral densities allows the frequency grids to be chosen so the harmonics have the same amplitude. The frequencies of these harmonics scale proportionally with the turbulence length scale. As a result, unit frequency grids which are normalized by the turbulence length scale may be calculated prior to the flight simulation. This property allows the turbulence length scale to be varied continuously with altitude without any additional computation time penalties. For a series of equal amplitude harmonics, the turbulence intensity of the simulated velocity field is decoupled from the number of harmonics. Then, the only remaining source of error is associated with the truncation of the infinite frequency spans of the autospectral densities. With exact integration, this discrepancy is uniquely defined by the truncated frequency range itself. Therefore, it can be arbitrarily defined (1%, 2%, 5%, etc.), and it remains constant, regardless of the number of harmonics, turbulence length scale, turbulence intensity, or true airspeed.

3. The Full-Field models predict lower rms translational accelerations than the Hub-Fixed model, especially at low airspeeds and low turbulence length scales. This is intuitively appealing, since a uniform velocity field represents the maximum mass flow through the rotor, i.e., the maximum turbulence induced translational acceleration. The longitudinal and vertical accelerations predicted by the Full-Field models were substantially lower those predicted by the Hub-Fixed model. Meanwhile, the lateral accelerations showed no appreciable change between models. In level flight, the longitudinal and vertical gusts act through the plane of the rotor disks, while the lateral gusts will act only in the plane of the rotor disks. Thus, lateral accelerations show no appreciable change between models due to the lack of sensitivity of the fixed system zeroth harmonic in-plane forces to higher harmonic in-plane relative wind perturbations.
4. The Full-Field models predicted higher rms rotational accelerations than the Hub-Fixed model, especially at low airspeeds and low turbulence length scales. This is also intuitively appealing, since the spatial variations of the velocity field will appear as additional rotational disturbances. The pitch and roll accelerations predicted by the Full-Field models were substantially higher than those predicted by the Hub-Fixed model. The change in predicted yaw acceleration is small because tandem rotor yaw acceleration results mainly from differential lateral hub forces. As previously discussed, the lateral hub forces are not sensitive to Full-Field versus Hub-Fixed turbulence modeling assumptions.
5. The impact of the Full-Field model on piloted simulation may be of limited importance since the predicted differences in rigid body accelerations are typically of the same order as the thresholds of human sensory perception. The differences between the models in vertical and pitch accelerations exceed the just noticeable difference. Therefore, the pilot should be able to reliably perceive these differences in the flight simulator. The difference between the models in longitudinal

acceleration also exceeds the just noticeable difference, but to a lesser extent. The difference between the models in lateral, roll and yaw accelerations are of the same order as the just noticeable difference, so the pilots may not be able to reliably perceive these differences in the simulator.

6. The pilots did not decisively identify an atmospheric turbulence model which was more realistic than the others. The pilots expressed comments during the flight simulation experiment which indicated that the Full-Field Normal model was slightly more realistic than the Hub-Fixed and Full-Field 3-Dimensional model. The rms vertical and pitch accelerations measured during the flight simulation experiment were correlated with the rms accelerations calculated during the non-real-time simulation. The other rigid body accelerations did not show any appreciable correlations. Also, the pilot responses on the post flight surveys were reasonably correlated with the simulated aircraft data measured during the precision hover task. Unfortunately, these comments were not substantiated in their post-flight survey responses. As a result, little few conclusions can be reached about the effect of the Full-Field model on flight simulation realism. The ambiguity of the pilot responses to the flight simulation survey reveal the difficulty associated with using human perception to substantiate a model's validity. Ultimately, physically realistic flight simulation requires the simulated aircraft to feel right to the pilot, without necessarily satisfying the formal mathematical models. Therefore, this makes human subjective evaluation the only effective way to determine the worthiness of a specific model.

The current work has developed a Full-Field atmospheric turbulence model for rotorcraft which is capable of real-time execution. Preliminary investigation of the benefits to more realistic rotorcraft handling qualities analysis in turbulent conditions has been done through piloted and unpiloted flight simulation. This is the first real-time implementation of full-field atmospheric turbulence, and there is much work still to be

done. The following list enumerates recommendations for future research in the area of rotorcraft atmospheric turbulence modeling.

1. Presently, there is little high quality experimental data on the nature of atmospheric turbulence in the vicinity of a lifting rotor. A comprehensive examination of the turbulence field and rotor disk interaction must be conducted to validate the full-field sampling approach. This would be most efficiently done in a wind tunnel, since the far-field turbulence field statistics could be controlled and parametric studies could be conducted.

2. On basic assumption of the full-field sampling approach in the current work is that the $^3/_4$ radius can be used as the representative blade station to obtain reasonably accurate blade response statistics. Studies have validated this assumption based on rotor flapping response and blade root bending moment. However, similar parametric analyses should be conducted to show that the $^3/_4$ radius may be used as the representative blade station to obtain reasonably accurate aircraft rigid body response statistics.

3. The pilot evaluation approach is clearly very subjective, and this presents problems for investigating the realism of the simulated atmospheric turbulence. A simplified single axis flight task should be evaluated in the same way the current work evaluated the hover, cruise and coordinated turn tasks. This would alleviate some of the complexities and pilot distractions from the evaluation procedure. It would allow the pilot to focus his attention on the turbulence induced motions more distinctly.

Appendix A

Integration of the von Kármán Autospectra

A.1 Longitudinal Autospectral Density

The von Kármán longitudinal autospectral density in terms of Cartesian spatial frequencies is given by:

$$S_{uu}(\Omega_1,\Omega_2)=\frac{\sigma_u^2(aL_u)^2}{6\pi}\frac{1+(aL_u)^2\Omega_1^2+\frac{11}{3}(aL_u)^2\Omega_2^2}{\left[1+(aL_u)^2(\Omega_1^2+\Omega_2^2)\right]^{\frac{7}{3}}} \tag{A.1.1}$$

A coordinate transformation from Cartesian spatial frequencies to polar spatial frequencies yields:

$$S_{uu}(r,\theta)=\frac{\sigma_u^2(aL_u)^2}{6\pi}\frac{\left[1+(aL_u)^2r^2\left(1+\frac{8}{3}\sin^2\theta\right)\right]}{\left[1+(aL_u)^2r^2\right]^{\frac{7}{3}}} \tag{A.1.2}$$

The indefinite integrals of any arbitrary transformed function must satisfy:

$$\iint S_{uu}(x,y)dxdy=\iint S_{uu}(r,\theta)rdrd\theta \tag{A.1.3}$$

Substitution of Equation (A.1.2) into Equation (A.1.3) yields:

$$\iint S_{uu}(r,\theta)rdrd\theta=\frac{\sigma_u^2(aL_u)^2}{6\pi}\iint\left\{\frac{1}{\left[1+(aL_u)^2r^2\right]^{\frac{7}{3}}}+\frac{(aL_u)^2r^2\left(1+\frac{8}{3}\sin^2\theta\right)}{\left[1+(aL_u)^2r^2\right]^{\frac{7}{3}}}\right\}rdrd\theta \tag{A.1.4}$$

Direct integration of the first term of Equation (A.1.4) yields:

$$\text{Term 1}=\frac{\sigma_u^2(aL_u)^2}{6\pi}\int_{\theta_1}^{\theta_2}d\theta\int_{r_1}^{r_2}\frac{1}{\left[1+(aL_u)^2r^2\right]^{\frac{7}{3}}}rdr \tag{A.1.5}$$

$$= \frac{\sigma_u^2 (aL_u)^2}{6\pi} [\theta]_{\theta_1}^{\theta_2} \left[\frac{-3}{8(aL_u)^2} \frac{1}{\left[1+(aL_u)^2 r^2\right]^{4/3}} \right]_{r_1}^{r_2} \tag{A.1.6}$$

$$\text{Term 1} = \frac{\sigma_u^2}{16\pi} [\theta]_{\theta_1}^{\theta_2} \left[\frac{1}{\left[1+(aL_u)^2 r^2\right]^{4/3}} \right]_{r_1}^{r_2} \tag{A.1.7}$$

Direct integration of the second term of Equation (A.1.4) yields:

$$\text{Term 2} = \frac{\sigma_u^2 (aL_u)^4}{6\pi} \int_{\theta_1}^{\theta_2} \left[1 + \tfrac{8}{3}\sin^2\theta\right] d\theta \int_{r_1}^{r_2} \frac{r^2}{\left[1+(aL_u)^2 r^2\right]^{7/3}} r dr \tag{A.1.8}$$

$$= \frac{\sigma_u^2 (aL_u)^4}{6\pi} \left[\theta + \tfrac{8}{3}\left(\tfrac{1}{2}\theta - \tfrac{1}{4}\sin 2\theta\right)\right]_{\theta_1}^{\theta_2} \int_{r_1}^{r_2} \frac{r^2}{\left[1+(aL_u)^2 r^2\right]^{7/3}} r dr \tag{A.1.9}$$

$$= \frac{\sigma_u^2 (aL_u)^4}{6\pi} \left[\tfrac{7}{3}\theta - \tfrac{2}{3}\sin 2\theta\right]_{\theta_1}^{\theta_2} \int_{r_1}^{r_2} \frac{r^2}{\left[1+(aL_u)^2 r^2\right]^{7/3}} r dr \tag{A.1.10}$$

Integration by parts requires the following change of variables in Equation (A.1.10):

$$\int x dy = xy - \int y dx \tag{A.1.11}$$

where,

$$x = r^2 \qquad y = \frac{-3}{8(aL_u)^2} \frac{1}{\left[1+(aL_u)^2 r^2\right]^{4/3}}$$

$$dx = 2rdr \qquad dy = \frac{1}{\left[1+(aL_u)^2 r^2\right]^{7/3}} r dr$$

Substitution of Equation (A.1.11) into Equation (A.1.10) yields:

$$= \frac{\sigma_u^2 (aL_u)^4}{6\pi} \left[\tfrac{7}{3}\theta - \tfrac{2}{3}\sin 2\theta\right]_{\theta_1}^{\theta_2} \left[\frac{-3}{8(aL_u)^2} \frac{r^2}{\left[1+(aL_u)^2 r^2\right]^{4/3}} + \int \frac{3}{4(aL_u)^2} \frac{1}{\left[1+(aL_u)^2 r^2\right]^{4/3}} r dr \right]_{r_1}^{r_2} \tag{A.1.12}$$

Direct integration of Equation (A.1.12) yields:

$$= \frac{-\sigma_u^2 (aL_u)^2}{16\pi} \left[\frac{7}{3}\theta - \frac{2}{3}\sin 2\theta \right]_{\theta_1}^{\theta_2} \left[\frac{r^2}{\left[1+(aL_u)^2 r^2\right]^{4/3}} + \frac{3}{(aL_u)^2} \frac{1}{\left[1+(aL_u)^2 r^2\right]^{1/3}} \right]_{r_1}^{r_2} \quad \text{(A.1.13)}$$

$$\text{Term 2} = \frac{-\sigma_u^2}{16\pi} \left[7\theta - 2\sin 2\theta \right]_{\theta_1}^{\theta_2} \left[\frac{1+\frac{4}{3}(aL_u)^2 r^2}{\left[1+(aL_u)^2 r^2\right]^{4/3}} \right]_{r_1}^{r_2} \quad \text{(A.1.14)}$$

Finally, combination of Equations (A.1.7) and (A.1.14) yields the exact integral of the von Kármán longitudinal autospectral density:

$$\int_{r_1}^{r_2} \int_{\theta_1}^{\theta_2} S_{uu}(r,\theta) r dr d\theta = \frac{-\sigma_u^2}{16\pi} \left[[\theta]_{\theta_1}^{\theta_2} \left[\frac{1}{\left[1+(aL_u)^2 r^2\right]^{1/3}} \right]_{r_1}^{r_2} + [7\theta + 2\sin 2\theta]_{\theta_1}^{\theta_2} \left[\frac{1+\frac{4}{3}(aL_u)^2 r^2}{\left[1+(aL_u)^2 r^2\right]^{4/3}} \right]_{r_1}^{r_2} \right] \quad \text{(A.1.15)}$$

A.2 Lateral Autospectral Density

The von Kármán lateral autospectral density in terms of Cartesian spatial frequencies is given by:

$$S_{vv}(\Omega_1,\Omega_2)=\frac{\sigma_v^2(aL_v)^2}{6\pi}\frac{1+\frac{11}{3}(aL_v)^2\Omega_1^2+(aL_v)^2\Omega_2^2}{\left[1+(aL_v)^2(\Omega_1^2+\Omega_2^2)\right]^{11/3}} \tag{A.2.1}$$

A coordinate transformation from Cartesian spatial frequencies to polar spatial frequencies yields:

$$S_{vv}(r,\theta)=\frac{\sigma_v^2(aL_v)^2}{6\pi}\frac{\left[1+(aL_v)^2r^2\left(1+\frac{8}{3}\cos^2\theta\right)\right]}{\left[1+(aL_v)^2r^2\right]^{11/3}} \tag{A.2.2}$$

The indefinite integrals of any arbitrary transformed function must satisfy:

$$\iint S_{vv}(x,y)dxdy=\iint S_{vv}(r,\theta)rdrd\theta \tag{A.2.3}$$

Substitution of Equation (A.2.2) into Equation (A.2.3) yields:

$$\iint S_{vv}(r,\theta)rdrd\theta=\frac{\sigma_v^2(aL_v)^2}{6\pi}\iint\left\{\frac{1}{\left[1+(aL_v)^2r^2\right]^{11/3}}+\frac{(aL_v)^2r^2\left(1+\frac{8}{3}\cos^2\theta\right)}{\left[1+(aL_v)^2r^2\right]^{11/3}}\right\}rdrd\theta \tag{A.2.4}$$

Direct integration of the first term of Equation (A.2.4) yields:

$$\text{Term 1}=\frac{\sigma_v^2(aL_v)^2}{6\pi}\int_{\theta_1}^{\theta_2}d\theta\int_{r_1}^{r_2}\frac{1}{\left[1+(aL_v)^2r^2\right]^{11/3}}rdr \tag{A.2.5}$$

$$=\frac{\sigma_v^2(aL_v)^2}{6\pi}[\theta]_{\theta_1}^{\theta_2}\left[\frac{-3}{8(aL_v)^2}\frac{1}{\left[1+(aL_v)^2r^2\right]^{8/3}}\right]_{r_1}^{r_2} \tag{A.2.6}$$

$$\text{Term 1}=\frac{\sigma_v^2}{16\pi}[\theta]_{\theta_1}^{\theta_2}\left[\frac{1}{\left[1+(aL_v)^2r^2\right]^{8/3}}\right]_{r_1}^{r_2} \tag{A.2.7}$$

Direct integration of the second term of Equation (A.2.4) yields:

$$\text{Term 2} = \frac{\sigma_v^2 (aL_v)^4}{6\pi} \int_{\theta_1}^{\theta_2} \left[1 + \tfrac{8}{3}\cos^2\theta\right] d\theta \int_{r_1}^{r_2} \frac{r^2}{\left[1 + (aL_v)^2 r^2\right]^{7/3}} rdr \tag{A.2.8}$$

$$= \frac{\sigma_v^2 (aL_v)^4}{6\pi} \left[\theta + \tfrac{8}{3}\left(\tfrac{1}{2}\theta + \tfrac{1}{4}\sin 2\theta\right)\right]_{\theta_1}^{\theta_2} \int_{r_1}^{r_2} \frac{r^2}{\left[1 + (aL_v)^2 r^2\right]^{7/3}} rdr \tag{A.2.9}$$

$$= \frac{\sigma_v^2 (aL_v)^4}{6\pi} \left[\tfrac{7}{3}\theta + \tfrac{2}{3}\sin 2\theta\right]_{\theta_1}^{\theta_2} \int_{r_1}^{r_2} \frac{r^2}{\left[1 + (aL_v)^2 r^2\right]^{7/3}} rdr \tag{A.2.10}$$

Integration by parts requires the following change of variables in Equation (A.2.10):

$$\int x\,dy = xy - \int y\,dx \tag{A.2.11}$$

where,

$$x = r^2 \qquad y = \frac{-3}{8(aL_v)^2} \frac{1}{\left[1 + (aL_v)^2 r^2\right]^{4/3}}$$

$$dx = 2rdr \qquad dy = \frac{1}{\left[1 + (aL_v)^2 r^2\right]^{7/3}} rdr$$

Substitution of Equation (A.2.11) into Equation (A.2.10) yields:

$$= \frac{\sigma_v^2 (aL_v)^4}{6\pi} \left[\tfrac{7}{3}\theta + \tfrac{2}{3}\sin 2\theta\right]_{\theta_1}^{\theta_2} \left[\frac{-3}{8(aL_v)^2} \frac{r^2}{\left[1 + (aL_v)^2 r^2\right]^{4/3}} + \int \frac{3}{4(aL_v)^2} \frac{1}{\left[1 + (aL_v)^2 r^2\right]^{4/3}} rdr \right]_{r_1}^{r_2} \tag{A.2.12}$$

Direct integration of Equation (A.2.12) yields:

$$= \frac{-\sigma_v^2 (aL_v)^2}{16\pi} \left[\tfrac{7}{3}\theta + \tfrac{2}{3}\sin 2\theta\right]_{\theta_1}^{\theta_2} \left[\frac{r^2}{\left[1 + (aL_v)^2 r^2\right]^{4/3}} + \frac{3}{(aL_v)^2} \frac{1}{\left[1 + (aL_v)^2 r^2\right]^{1/3}} \right]_{r_1}^{r_2} \tag{A.2.13}$$

$$\text{Term 2} = \frac{-\sigma_v^2}{16\pi} \left[7\theta + 2\sin 2\theta\right]_{\theta_1}^{\theta_2} \left[\frac{1 + \frac{4}{3}(aL_v)^2 r^2}{\left[1 + (aL_v)^2 r^2\right]^{4/3}} \right]_{r_1}^{r_2} \tag{A.2.14}$$

Finally, combination of Equations (A.2.7) and (A.2.14) yields the exact integral of the von Kármán lateral autospectral density:

$$\int_{r_1}^{r_2}\int_{\theta_1}^{\theta_2} S_{vv}(r,\theta)\,r\,dr\,d\theta = \frac{-\sigma_v^2}{16\pi}\left[\left[\theta\right]_{\theta_1}^{\theta_2}\left[\frac{1}{\left[1+(aL_v)^2 r^2\right]^{4/3}}\right]_{r_1}^{r_2} + \left[7\theta+2\sin 2\theta\right]_{\theta_1}^{\theta_2}\left[\frac{1+\frac{4}{3}(aL_v)^2 r^2}{\left[1+(aL_v)^2 r^2\right]^{4/3}}\right]_{r_1}^{r_2}\right] \tag{A.2.15}$$

A.3 Vertical Autospectral Density

The von Kármán vertical autospectral density in terms of Cartesian spatial frequencies is given by:

$$S_{ww}(\Omega_1,\Omega_2)=\frac{4\sigma_w^2(aL_w)^4}{9\pi}\frac{\left(\Omega_1^2+\Omega_2^2\right)}{\left[1+(aL_w)^2\left(\Omega_1^2+\Omega_2^2\right)\right]^{7/3}} \tag{A.3.1}$$

A coordinate transformation from Cartesian spatial frequencies to polar spatial frequencies yields:

$$S_{ww}(r,\theta)=\frac{4\sigma_w^2(aL_w)^4}{9\pi}\frac{r^2}{\left[1+(aL_w)^2r^2\right]^{7/3}} \tag{A.3.2}$$

The indefinite integrals of any arbitrary transformed function must satisfy:

$$\iint S_{ww}(x,y)dxdy=\iint S_{ww}(r,\theta)rdrd\theta \tag{A.3.3}$$

Substitution of Equation (A.3.2) into Equation (A.3.3) yields:

$$\iint S_{ww}(r,\theta)rdrd\theta=\frac{4\sigma_w^2(aL_w)^4}{9\pi}\iint\frac{r^2}{\left[1+(aL_w)^2r^2\right]^{7/3}}rdrd\theta \tag{A.3.4}$$

Direct integration of Equation (A.3.4) yields:

$$=\frac{4\sigma_w^2(aL_w)^4}{9\pi}[\theta]\Big|_{\theta_1}^{\theta_2}\int_{r_1}^{r_2}\frac{r^2}{\left[1+(aL_w)^2r^2\right]^{7/3}}rdr \tag{A.3.5}$$

Integration by parts requires the following change of variables in Equation (A.3.5):

$$\int xdy=xy-\int ydx \tag{A.3.6}$$

where

$$x=r^2 \qquad y=\frac{-3}{8(aL_w)^2}\frac{1}{\left[1+(aL_w)^2r^2\right]^{4/3}}$$

$$dx=2rdr \qquad dy=\frac{1}{\left[1+(aL_w)^2r^2\right]^{7/3}}rdr$$

Substitution of Equation (A.3.6) into Equation (A.3.5) yields:

$$= \frac{\sigma_w^2 (aL_w)^4}{6\pi} \left[\frac{7}{3}\theta - \frac{2}{3}\sin 2\theta \right]_{\theta_1}^{\theta_2} \left[\frac{-3}{8(aL_w)^2} \frac{r^2}{\left[1+(aL_w)^2 r^2\right]^{4/3}} + \int \frac{3}{4(aL_w)^2} \frac{1}{\left[1+(aL_w)^2 r^2\right]^{4/3}} rdr \right]_{r_1}^{r_2} \tag{A.3.7}$$

Direct integration of Equation (A.3.7) yields:

$$= \frac{-\sigma_w^2}{6\pi} [\theta]_{\theta_1}^{\theta_2} \left[\frac{(aL_w)^2 r^2}{\left[1+(aL_w)^2 r^2\right]^{4/3}} + \frac{3}{\left[1+(aL_w)^2 r^2\right]^{1/3}} \right]_{r_1}^{r_2} \tag{A.3.8}$$

Finally, simplification of Equation (A.3.8) yields the exact integral of the von Kármán vertical autospectral density:

$$\int_{r_1}^{r_2} \int_{\theta_1}^{\theta_2} S_{ww}(r,\theta) r dr d\theta = \frac{-\sigma_w^2}{2\pi} \left[[\theta]_{\theta_1}^{\theta_2} \left[\frac{1+\frac{4}{3}(aL_w)^2 r^2}{\left[1+(aL_w)^2 r^2\right]^{4/3}} \right] \right]_{r_1}^{r_2} \tag{A.3.9}$$

Appendix B

Percentiles of the von Kármán Autospectra

The columns of this table list the normalized frequency ranges which bound a given percentile of turbulent energy of the von Kármán autospectral density functions.

Energy Percentile	Normalized Longitudinal Spatial Frequency	Normalized Lateral Spatial Frequency	Normalized Vertical Spatial Frequency
0.5	0.17285	0.17285	0.41173
1.0	0.24413	0.24413	0.50309
1.5	0.29880	0.29880	0.56893
2.0	0.34499	0.34499	0.62295
2.5	0.38586	0.38586	0.66998
3.0	0.42301	0.42301	0.71236
3.5	0.45743	0.45743	0.75141
4.0	0.48974	0.48974	0.78795
4.5	0.52037	0.52037	0.82253
5.0	0.54963	0.54963	0.85556
6.0	0.60498	0.60498	0.91806
7.0	0.65714	0.65714	0.97705
8.0	0.70699	0.70699	1.03357
9.0	0.75513	0.75513	1.08831
10.0	0.80203	0.80203	1.14178
	...	...	...
90.0	39.82775	39.82775	48.66847
91.0	46.65360	46.65360	57.00690
92.0	55.67557	55.67557	68.02852
93.0	68.02871	68.02871	83.12010
94.0	85.73186	85.73186	104.74821
95.0	112.70303	112.70303	137.69972
95.5	132.00179	132.00179	161.27785
96.0	157.51249	157.51249	192.44554
96.5	192.44558	192.44558	235.12519
97.0	242.51125	242.51125	296.29334
97.5	318.79129	318.79129	389.48935
98.0	445.52624	445.52624	544.32945
98.5	685.93425	685.93425	838.05144
99.0	1260.14333	1260.14333	1539.60015
99.5	3564.22530	3564.22530	4354.64823

Appendix C

CH-47D Dimensional Stability Derivatives

For the following table, the rigid body forces and moments are presented in the columns and the perturbations are presented in the rows. For example,

$$X_u = \frac{1}{m}\frac{\partial X}{\partial u} \cong -0.012728; \qquad L_u = \frac{1}{I_x}\frac{\partial L}{\partial u} \cong -0.000736$$

Flight Condition 1:

ρ	0.00238 slugs/feet^3	m	1,242 slugs
V_{TAS}	20 knots	I_x	46,300 slug·feet^2
		I_y	228,000 slug·feet^2
θ_{trim}	3.175 degrees	I_z	208,000 slug·feet^2
ϕ_{trim}	–0.335 degrees	I_{xz}	16,000 slug·feet^2

	X	Y	Z	L	M	N
u	–0.012728	0.000569	–0.171709	–0.000239	–0.000736	0.001417
v	0.001220	–0.041254	0.002036	–0.006052	–0.005079	0.000046
w	0.023383	0.002921	–0.466030	0.000844	0.000481	0.001125
p	–0.025912	–2.254424	–0.294934	–0.634107	–0.154322	–0.085201
q	1.861396	–0.125076	2.937016	0.175654	–1.051426	–0.273958
r	–0.609664	–0.255167	–0.092312	–0.051250	–0.277336	–0.101492
Pilot Control Derivatives: (c-collective, b-longitudinal stick, s-lateral stick, r-pedals)						
δ_c	0.474675	0.064860	–10.243005	–0.012622	0.048078	0.002037
δ_b	0.225513	–0.007162	–0.012473	–0.021046	0.367865	0.050755
δ_s	–0.002971	1.149460	–0.002693	0.469641	–0.003905	0.009848
δ_r	–0.060120	–0.004317	0.055268	–0.124819	–0.003267	0.224344
Forward Rotor Control Derivatives: (θ-collective pitch, a-lateral pitch, b-longitudinal pitch)						
θ_{0f}	0.301072	0.011926	–2.763091	–0.019582	0.295897	0.039590
a_{1cf}	–0.010231	0.300227	0.007985	0.103317	–0.001536	0.037852
b_{1cf}	0.276664	0.008354	0.217189	–0.002513	–0.044084	0.001111
Aft Rotor Control Derivatives: (θ-collective pitch, a-lateral pitch, b-longitudinal pitch)						
θ_{0r}	–0.045870	0.022945	–2.743902	0.012797	–0.270049	–0.038495
a_{1cr}	–0.008675	–0.301584	0.009395	–0.142568	0.000509	0.032696
b_{1cr}	0.302265	–0.009696	0.190872	0.000589	–0.008837	0.000744

For the following table, the rigid body forces and moments are presented in the columns and the perturbations are presented in the rows. For example,

$$X_u = \frac{1}{m}\frac{\partial X}{\partial u} \cong -0.026203; \qquad L_u = \frac{1}{I_x}\frac{\partial L}{\partial u} \cong 0.000003$$

Flight Condition 2:

ρ	0.00238 slugs/feet^3	m	1,242 slugs
V_{TAS}	60 knots	I_x	46,300 slug·feet^2
		I_y	228,000 slug·feet^2
θ_{trim}	0.699 degrees	I_z	208,000 slug·feet^2
ϕ_{trim}	–0.180 degrees	I_{xz}	16,000 slug·feet^2

	X	Y	Z	L	M	N
u	–0.026203	0.000674	–0.062160	0.000003	–0.003567	0.000047
v	0.003058	–0.063424	0.001609	–0.003578	0.000609	0.001648
w	0.011678	0.001666	–0.705643	0.001239	0.007173	0.001443
p	–0.140013	–2.176739	–0.457534	–0.046169	0.169021	–0.065953
q	2.045576	–0.079770	2.423859	–0.008395	–1.347767	–0.168243
r	–0.380769	–0.109560	–0.034291	0.011810	–0.289032	–0.075446
Pilot Control Derivatives: (c-collective, b-longitudinal stick, s-lateral stick, r-pedals)						
δ_c	–0.017962	0.032928	–11.719584	–0.015675	0.106220	0.025732
δ_b	0.256952	0.021730	–0.054916	0.013112	0.418825	0.030116
δ_s	–0.000378	1.125312	0.000882	0.456936	–0.002785	0.007602
δ_r	–0.060037	–0.027901	0.028826	–0.125379	–0.000890	0.219473
Forward Rotor Control Derivatives: (θ-collective pitch, a-lateral pitch, b-longitudinal pitch)						
θ_{0f}	0.192827	0.025567	–3.192669	0.005873	0.350727	0.030084
a_{1cf}	–0.009539	0.290197	0.004763	0.099903	–0.000869	0.036948
b_{1cf}	0.239679	0.006229	0.646245	–0.005048	–0.089895	0.002619
Aft Rotor Control Derivatives: (θ-collective pitch, a-lateral pitch, b-longitudinal pitch)						
θ_{0r}	–0.202484	–0.007864	–3.108183	–0.014300	–0.293620	–0.016245
a_{1cr}	–0.009341	–0.298971	0.004302	–0.139330	0.000589	0.032518
b_{1cr}	0.326491	–0.009129	0.607403	0.000369	0.031908	–0.003117

For the following table, the rigid body forces and moments are presented in the columns and the perturbations are presented in the rows. For example,

$$X_u = \frac{1}{m}\frac{\partial X}{\partial u} \cong -0.035375; \qquad L_u = \frac{1}{I_x}\frac{\partial L}{\partial u} \cong 0.000313$$

Flight Condition 3:

ρ	0.00238 slugs/feet^3	m	1,242 slugs
V_{TAS}	100.0 knots	I_x	46,300 slug·feet^2
		I_y	228,000 slug·feet^2
θ_{trim}	0.078 degrees	I_z	208,000 slug·feet^2
ϕ_{trim}	–0.170 degrees	I_{xz}	16,000 slug·feet^2

	X	Y	Z	L	M	N
u	–0.035375	0.000809	0.009736	0.000313	–0.003059	–0.000112
v	0.005038	–0.086778	0.006083	–0.003494	0.001981	0.002169
w	0.021412	0.003031	–0.823090	0.001663	0.008677	0.000942
p	–0.049431	–1.937982	–0.459357	–0.869098	0.001153	–0.071300
q	1.843923	0.020498	1.365934	–0.019545	–1.767791	–0.135076
r	–0.303079	–0.118155	–0.156466	–0.018356	–0.336161	–0.084534
Pilot Control Derivatives: (c-collective, b-longitudinal stick, s-lateral stick, r-pedals)						
δ_c	0.027574	0.062919	–13.770302	–0.000172	0.132087	0.032949
δ_b	0.246181	–0.000211	–0.074390	0.015523	0.495405	0.025482
δ_s	0.001177	1.133240	0.006724	0.463090	–0.002836	0.009994
δ_r	–0.060390	0.011469	0.019999	–0.121624	–0.001650	0.221344
Forward Rotor Control Derivatives: (θ-collective pitch, a-lateral pitch, b-longitudinal pitch)						
θ_{0f}	0.196782	0.016752	-3.758916	0.011894	0.416588	0.028459
a_{1cf}	-0.009187	0.298463	0.004905	0.102104	-0.001002	0.037419
b_{1cf}	0.206420	0.012664	1.198405	-0.009113	-0.151295	0.004602
Aft Rotor Control Derivatives: (θ-collective pitch, a-lateral pitch, b-longitudinal pitch)						
θ_{0r}	–0.181957	0.017076	–3.644469	–0.011986	–0.345573	–0.010744
a_{1cr}	–0.009803	–0.294857	0.001384	–0.140351	0.000483	0.032186
b_{1cr}	0.323109	–0.022793	1.152577	–0.000187	0.084099	–0.006032

Appendix D

Flight Simulation Experiment Surveys

D.1 Pilot Background Survey

1. Name: _____
2. Estimated number of hours flown total: _____
3. Estimated number of hours flown in CH-46/47's: _____
4. Estimated number of hours flown in simulators: _____
5. What characteristic(s) of atmospheric turbulence most interferes with your ability to control the aircraft:

   Rank the importance of turbulence, relative to excursions in:

Pitch	Roll	Yaw	Surge	Sway	Heave
____	____	____	_____	_____	_____

6. Describe the most critical flight regime for atmospheric turbulence based upon your flying experience:
   a. Weather: _____
   b. Terrain: _____
   c. Altitude: _____
   d. Airspeed: _____
   e. What task you were attempting before the turbulence was encountered?

D.2 Flight Simulation Realism Survey

Name: _____

Trial Number: A B C

1. Turbulence Intensity:

Very Light	1	2	3	4	5	6	7	Very Severe

2. Overall Realism of Turbulence:

Very Unrealistic	1	2	3	4	5	6	7	Very Realistic

Reasons for dissatisfaction:

3. Realism of Relative Amplitudes of Excursions:

a. Pitch	Too Little	1	2	3	4	5	6	7	Too Much
b. Roll	Too Little	1	2	3	4	5	6	7	Too Much
c. Yaw	Too Little	1	2	3	4	5	6	7	Too Much
d. Long.	Too Little	1	2	3	4	5	6	7	Too Much
e. Lateral	Too Little	1	2	3	4	5	6	7	Too Much
f. Vertical	Too Little	1	2	3	4	5	6	7	Too Much

4. Did you notice any repetitive pattern in the turbulence? yes no

5. Frequency Content of Turbulence:

Low <1P	Too Little	1	2	3	4	5	6	7	Too Much
High >1P	Too Little	1	2	3	4	5	6	7	Too Much

6. Sudden Large Amplitude Gusts:

Too Seldom	1	2	3	4	5	6	7	Too Often

7. Cooper-Harper Rating: (1–10)
   a. Hover Task _____
   b. Cruise Task _____
   c. Coordinated Turn Task _____

8. Please note differences between the response of the actual aircraft and the response of the flight simulator which may have affected the experiment? (if any)

9. Please note differences between the cockpit of the actual aircraft and the cockpit of the flight simulator which may have affected the experiment? (if any)

Bibliography

[1] Borgman L.E., "Ocean Wave Simulation for Engineering Design," *Journal of the Waterways and Harbors Division, Proceedings of the American Society of Civil Engineers*, WW4, pages 557-583, November 1969.

[2] Campbell C.W., Sanborn V.A., "A Spatial Model of Wind Shear and Turbulence," *Journal of Aircraft*, Volume 21, Number 12, pages 929-935, December 1984.

[3] Connell J.R., "The Spectrum of Wind Speed Fluctuations Encountered by a Rotating Blade of a WEC," PNL-4083, Pacific Northwest Laboratory, Richland, Washington, April 1980.

[4] Cooper G.E., Harper R.P., "The Use of Pilot Rating in the Evaluation of Aircraft Handling Qualities," NASA Technical Note, NASA TN D-7067, November 1972.

[5] Costello M.F., "A Theory for the Analysis of Rotorcraft Operating in Atmospheric Turbulence," Presented at the 46th Annual Forum of the American Helicopter Society, May 1990.

[6] Costello M.F., "A Theory for the Analysis of Rotorcraft Operating in Atmospheric Turbulence," Ph.D. Thesis, School of Aerospace Engineering, Georgia Institute of Technology, 1991.

[7] Dahl H.L., Faulkner A.J., "Helicopter Simulation in Atmospheric Turbulence," *Vertica*, Volume 3, pages 65-78, 1979.

[8] Drees J.M., Harvey K.W., "Helicopter Gust Response at High Forward Speeds," Journal of Aircraft, Volume 7, Number 3, pages 225-230, May-June 1970.

[9] Dutton J.A., "Broadening Horizons in Prediction of the Effects of Atmospheric Turbulence on Aeronautical Systems," Presented at the AIAA Fifth Annual Meeting and Technical Display, AIAA Paper Number 68-1065, October 1968.

[10] Dutton J.A., Deaven D.G., "Some Observed Properties of Atmospheric Turbulence," Statistical Models and Turbulence, Volume 12 of Lecture Notes in Physics, Springer-Verlag, 1972.

[11] Dryden H.L., "A Review of the Statistical Theory of Turbulence," Classic Papers on the Statistical Theory of Turbulence (S.K. Fiedlander and L. Topper, editors), Interscience Publishers, New York, 1961.

[12] Etkin B., Dynamics of Atmospheric Flight, John Wiley and Sons, New York, 1972.

[13] George V.V., Gaonkar G.H., Prasad J.V.R., Schrage D.P., "Adequacy of Modeling Turbulence and Related Effects on Helicopter Response," *Journal of the American Institute of Aeronautics and Astronautics*, Volume 30, Number 6, pages 1468-1479, June 1992.

[14] Hackett W.E., Garnett T.S., Borek B.V., "Mathematical Model of the CH-47B Helicopter Capable of Real-Time Simulation of the Full Flight Envelope," Volume I and Volume II, NASA CR 166458, July 1983.

[15] Hoblit F.M., Gust Loads on Aircraft: Concepts and Applications, AIAA Education Series, Published by the American Institute of Aeronautics and Astronautics, 1988.

[16] Howlett J., "UH-60A Black Hawk Engineering Simulation Program: Volume I – Mathematical Model," NASA CR 166309, December 1981.

[17] Howlett J., "UH-60A Black Hawk Engineering Simulation Program: Volume II – Mathematical Model," NASA CR 166310, December 1981.

[18] Jacobson I.D., Joshi D.S., "Modeling Atmospheric Turbulence for a Motion Based Simulator," University of Virginia Technical Report ESS-4035-104-75, Charlottesville, Virginia, October 1975.

[19] Mayo J.R., Occhiato J.J., Hong S.W., "Helicopter Modeling Requirements for Full Mission Simulation and Handling Qualities Assessment," Presented at the 47th Annual Forum of the American Helicopter Society, May 1991.

[20] Miller D.G., Weber T.L., "Investigation of the Role of Atmospheric Turbulence on the CH-47D Helicopter Drive System Loads and Vibration," Boeing Defense and Space Group–Helicopters Division Technical Report D210-12921-1, Philadelphia, PA, 1993.

[21] Miller D.G., Engineer, Boeing Defense and Space Group, Helicopters Division, private communication, January 1994.

[22] Panofsky H.A., Dutton J.A., Atmospheric Turbulence, John Wiley and Sons, New York, 1984.

[23] Prasad J.V.R., Riaz J., Gaonkar G.H., Yingyi D., "Real Time Implementation Aspects of a Rotorcraft Turbulence Simulation Method," Proceedings of the 49th Annual Forum of the American Helicopter Society, May 1993.

[24] Reeves P.M., Campbell G.S., Ganzer V.M., Joppa R.G., "Development and Application of a Non-Gaussian Atmospheric Turbulence Model for Use in Flight Simulators," NASA CR-2451, September 1974.

[25] Riaz J., "A Simulation Model of Atmospheric Turbulence for Rotorcraft Applications," Ph.D. Thesis, School of Aerospace Engineering, Georgia Institute of Technology, 1991.

[26] Riaz J., Prasad J.V.R., Schrage D.P., Gaonkar G.H., "A New Method for Simulating Atmospheric Turbulence for Rotorcraft Applications," *Journal of the American Helicopter Society*, Volume 38, Number 1, pages 84-88, January 1993.

[27] Rolfe J.M., Staples K.J., Flight Simulation, Cambridge University Press, New York, 1991.

[28] Rosenbrock H., "Vibration and Stability Problems in Large Wind Turbines Having Hinged Blades," Electrical Research Association Technical Report C/T 113, Surrey, England, 1955.

[29] Roskam J., Airplane Flight Dynamics and Automatic Flight Controls, Roskam Aviation and Engineering Corporation, 1979.

[30] Shinozuka M., Jan C., "Digital Simulation of Random Processes and Its Applications," *Journal of Sound and Vibration*, Volume 25, Number 1, pages 111-168, 1972.

[31] Taylor G.I., "The Spectrum of Turbulence," Proceedings of the Royal Society of London, Volume A164, pages 476, 1938.

[32] United States Department of Defense, "Flying Qualities of Piloted Aircraft," Military Specification, MIL-F-8785C, pages 45-62, November 1980.

[33] Veers P.S., "Modeling Stochastic Wind Loads on Vertical Axis Wind Turbines," SAND83–1909 UC–60, Sandia National Laboratories, Albuquerque, New Mexico, September 1984.

[34] Veers P.S., "Three-Dimensional Wind Simulation," SAND88–0152 UC–261, Sandia National Laboratories, Albuquerque, New Mexico, March 1988.

[35] Verholek G.M., "Preliminary Results of a Field Experiment to Characterize Wind Flow Through a Vertical Plane," PNL-2518, Pacific Northwest Laboratory, Richland, Washington, April 1978.

[36] von Kármán T., "Progress in the Statistical Theory of Turbulence," *Proceedings of the National Academy of Science*, Volume 34, 1948.

[37] Weber, T.L., "Turbulence Induced Loads on a Teetered Rotor," Ph.D. Thesis, Oregon State University, 1991.

[38] Young L.R., "Chapter 22 Perception of the body in space: Mechanisms," In Handbook of Physiology - The Nervous System, Volume 3, American Physiological Society, Bethesda, Maryland, 1984.

[39] Young L.R., Professor, Department of Aeronautics and Astronautics, Massachusetts Institue of Technology, private communication, March 1994.